School of Electrical Engineering, Computing and
Mathematical Sciences

The Polarimetric Properties of Fast Radio Burst Emission at Nanosecond Time Resolution

Danica R. Scott

ORCID iD: 0000-0002-6895-4156

This thesis is presented for the Degree of
Doctor of Philosophy
of
Curtin University of Technology

August 2024

To the best of my knowledge and belief this thesis contains no material previously published by any other person except where due acknowledgement has been made. This thesis contains no material which has been accepted for the award of any other degree or diploma in any university.

Danica Scott

Danica R. Scott

March 20, 2024

I acknowledge the Whadjuk People of the Noongar Nation, the traditional owners of the land on which Curtin University is located, where the work in this thesis was developed and written; the Wajarri Yamaji, the traditional owners of Wajarri Country that Inyarrimanha Ilgari Bundara, the Murchison Radio-astronomy Observatory, is on, where the Australian Square Kilometre Array Pathfinder is located; and the Wurundjeri People, the traditional owners of the land where Swinburne University and the OzStar Supercomputer are located.

I also acknowledge that no words I could write could ever make up for the genocide and dispossession of Indigenous people that took place in the colonisation of these lands, as well as the rest of Australia. Sovereignty was never ceded. Australia always was, and always will be Aboriginal land.

Acknowledgements

This research is supported by an Australian Government Research Training Program (RTP) Scholarship. This work was performed on the OzSTAR national facility at Swinburne University of Technology. The OzSTAR program receives funding in part from the Astronomy National Collaborative Research Infrastructure Strategy (NCRIS) allocation provided by the Australian Government, and from the Victorian Higher Education State Investment Fund (VHESIF) provided by the Victorian Government.

I want to acknowledge and express my thanks to my supervisors, Dr Clancy James, Dr Marcin Glowacki, and A/Prof Adrian Sutinjo, for their collaboration and guidance; all members of the Commensal Real-Time ASKAP Fast Transients Collaboration, especially Prof Adam Deller, Dr Kelly Gourdji, Dr Apurba Bera, and Tyson Dial for their work on CELEBI; Hyerin Cho and Dr Cherie Day, whose work this thesis is a direct continuation of; the research staff community at the Curtin Institute for Radio Astronomy, in particular Prof Cathryn Trott for her guiding role as chair of my thesis panel; and the late Jean-Pierre Macquart, who introduced me to fast radio bursts, and whose love for science and drive to understand the Universe rubbed off on me greatly.

I also want to acknowledge and thank my friends and comrades who have supported me over many years leading up to the finalisation of this thesis: Mawson Sammons, Alessandro Paduano, Jaiden Cook, Tyrone O'Doherty, Callan Wood, Susmita Sett, and especially Freya North-Hickey, who was there with me studying through more late nights, early mornings, weekends, and public holidays than I

could possibly hope to recall; and Erin Russell, Clare Francis, Vashti Fox, and Alevine Magila, who have given me the inspiration and motivation powering the light at the end of the tunnel.

As a final note, it is impossible for me to ignore the genocide of Palestinians in Gaza that has taken place during the final ten months of work on this thesis, and the prevalence of the dual-use of astronomy research for military purposes. What work is done in the future that may utilise or build upon what I have done here is out of my control, but it is my hope that it is never put towards military-related purposes in any way.

من النهر إلى البحر
فلسطين ستتحرر

"All science would be superfluous if the outward appearance and the essence of things directly coincided."

— Karl Marx

Abstract

Fast radio bursts (FRBs) are micro-to-millisecond duration radio transients of typically extragalactic origin, which promise new opportunities for investigating physics on scales ranging from the subatomic to the cosmological. These investigations demand high-resolution measurements of the polarimetric properties of the bursts themselves and of their sky position. The former allows examination of burst emission mechanisms and the effects of propagation through interstellar and intergalactic media; the latter allows identification of host galaxies, from which inferences can be made of progenitor populations and cosmological quantities that define the nature of the Universe. Making these measurements is complicated by the typically once-off, impulsive nature of FRBs; the overwhelmingly large data volumes associated with high time and spatial resolutions make blind FRB searches infeasible without compromising on data resolution or specialised instruments and techniques. The Australian Square Kilometre Array Pathfinder (ASKAP) has been enabled by the Commensal Real-time ASKAP Fast Transients Survey (CRAFT) to make real-time detections of FRBs and capture their signals in voltages separately across antennas and linear polarisation bases. This allows burst localisation to sub-arcsecond precision via interferometric imaging, and for the effectively perfect reconstruction of the electric field of burst emission at nanosecond-level time resolution.

In this thesis, I describe the CRAFT Effortless Localisation and Enhanced Burst Inspection pipeline (CELEBI): an automated, offline processing pipeline I have developed for producing FRB localisations and high-time resolution polari-

metric data from CRAFT voltages. CELEBI automates and extends processing methods previously applied by CRAFT, significantly improving the reliability and robustness of processing ASKAP FRB data products. It has reduced the typical turnaround time between FRB detection and obtaining final data products from days to hours, and reduced the level of human intervention involved to a small fraction of that previously required. At the time of writing, CELEBI has been key to ten publications, and will continue to be a vital element of FRB science with ASKAP, especially as the CRACO upgrade to ASKAP comes online.

I also present the polarimetric profiles and properties of 21 ASKAP FRBs processed with CELEBI. This sample is demonstrative of the capabilities of ASKAP and CELEBI to produce world-leading FRB data with high signal-to-noise ratios (up to $\sim$500) at high time resolutions (on the order of microseconds) of repeating and non-repeating FRBs alike.

Finally, I present an investigation into measuring the statistics of coherence of FRB emission, a line of inquiry with the potential to reveal the physical processes giving rise to FRB emission. This is made possible by ASKAP's unique ability to obtain electric field measurements at $\sim 3\,\mathrm{ns}$ for all bursts detected in real-time.

Contents

List of Figures

Introduction

The study of fast radio bursts (FRBs) — typically spontaneous and extragalactic radio transients shorter than a few milliseconds — has matured since the years immediately following their serendipitous discovery in archived Murriyang[1] data (Lorimer et al., 2007). The number of reported FRB discoveries is nearing a thousand,[2] and large surveys are increasing the observed population rapidly (e.g. CHIME/FRB Collaboration et al. 2021).

FRBs have opened new avenues for astrophysical investigation. In understanding the nature of the bursts themselves, many new models for the emission physics of electromagnetic radiation have been (and continue to be) developed (Platts et al., 2019)[3]. That there is no consensus on this as yet shows the potential for the growth of theoretical astrophysics by pursuing the explanation of FRB signals; it also is a sign that FRB measurements to date are of insufficient precision to draw definite conclusions. These models will inform possible progenitor objects drawn from the small but growing set of FRB host galaxies. The imprints of propagation through various media on FRB signals can be clues to the nature of the environments from which they are emitted, and on a grander scale are allowing the resolution of cosmological conflicts, such as the missing baryon problem (Macquart et al., 2020).

Merely observing FRBs in their ones and twos is no longer enough to push FRB science forward. Increasing the quantity of bursts analysed via higher detection

[1] Previously known as the Parkes Radio Telescope.

[2] 947 bursts from 691 sources at the time of writing according to the Transient Name Server (wis-tns.org).

[3] frbtheorycat.org

rates & large samples and making measurements of burst properties in finer detail have become of much greater importance to advancing the field.

The Australian Square Kilometre Array Pathfinder (ASKAP), as applied by the Commensal Real-time ASKAP Fast Transients Collaboration (CRAFT), is among the most important instruments in the world for FRB science. It is able to detect FRBs in real-time (including first detections of burst sources — i.e. including non-repeaters), allowing sub-arcsecond interferometric burst localisation *and* recovery of the raw electric field measurements across all antennas and both linear polarisations at the full bandwidth-limited time resolution of just under 3 ns. Placing bursts in host galaxies from only a single detection has been a significant step forward in the field, and is a major factor in enabling the application of FRBs to cosmological studies. No other instrument is able to obtain reliably artefact-free electric field measurements at the nanosecond level for all bursts detected.

The primary motivation driving this thesis is making a contribution to improving the quality of FRB measurements with ASKAP. Specifically, the aim was to automate ASKAP's ability to obtain sub-arcsecond FRB localisations and nanosecond-level time resolution polarimetric profiles so that these high-quality data products can be produced consistently and quickly. To this end, the primary work of this thesis is the CRAFT Effortless Localisation and Enhanced Burst Inspection pipeline (CELEBI), an automated software pipeline that produces FRB positions and high-time resolution data from ASKAP voltages. The application of this pipeline to preliminary studies of burst properties at high time resolutions is also encompassed in this work.

Chapter 1 reviews the literature and summarises current knowledge in relation to FRBs. Chapter 2 reviews the capabilities of ASKAP in relation to FRBs, and its contributions to the field thus far. Chapter 3 introduces the motivations and outcomes of the development of CELEBI, and summarises ten publications CELEBI's development made a direct contribution to. Chapter 4 describes CELEBI's implementation and methodology in detail. It was published as a paper

in *Astronomy & Computing* (Scott et al., 2023). Chapter 5 presents the to-date sample of FRBs observed with ASKAP for which high time resolution polarimetric data is available. The focus is on presenting the data itself and outlining trends and future avenues open for investigation with the expanding ASKAP FRB sample. At the time of writing, it is in the final stages of collaboration review for journal submission as a paper. Chapter 6 summarises preliminary investigations into applying the nanosecond-level FRB measurements to search for evidence of coherence in the burst emission mechanism. Chapter 7 provides a summary and conclusions for this thesis.

Chapter 1

Fast radio bursts

Fast radio bursts are a class of radio-frequency, short-duration transients, the first of which was discovered serendipitously in a search for pulsars in archival data collected with the Murriyang radio telescope (Lorimer et al., 2007). Thornton et al. (2013) confirmed their existence with the discovery of four more bursts, and inferred that they originate at cosmological distances via their large dispersion measures (DMs), which imply they travel through more ionised media than is present in our own Milky Way (§1.3.1).

FRBs are characterised primarily by their short durations, on the order of milliseconds or less. That they are extragalactic in origin has now been confirmed by host galaxy identifications for a small set of FRBs (e.g. Chatterjee et al. 2017; Bannister et al. 2019b; Ravi et al. 2019). It is thought that no FRB observed to date is likely to be from within the Milky Way, although FRB-like emission has been observed from a Galactic magnetar (CHIME/FRB Collaboration et al., 2020b; Bochenek et al., 2020). While some FRBs have been observed to repeat, most are apparently non-repeating (§1.4).

The spectra of FRBs tend to be broad (over at least $\sim 100\,\mathrm{MHz}$), and sometimes evolve between different components of the same burst (particularly in repeating FRBs; §1.4). They have been observed in bands from 110 MHz (Pleunis et al., 2021b) up to 8 GHz (Gajjar et al., 2018). There is no common shape to

FRB spectra, with the spectral indices of power-law fits varying widely and being of mixed applicability (Zhang, 2022).

1.1 High-time resolution measurments

The frequency-time morphologies of FRBs are diverse, with bursts having been observed with single narrow broadband peaks, multiple distinct sub-components, (relatively) broad complex profiles with drifting spectral occupancy, and many other shapes; some examples are shown in Figure 1.1. However, these features are often inaccessible as most FRB detections and measurements are done with a time resolution on the order of 1 ms, which severely limits the ability to resolve all but the broadest burst profiles. Recently, the number of measurements at higher time resolutions (< 1 ms) is increasing, made possible by advances in instrumentation and processing techniques.

FRB 20121102A, the first discovered repeating FRB, was the first to be examined at high time resolutions, with bursts detected by the Arecibo and Green Bank radio telescopes displaying structure on timescales on the order of tens to hundreds of µs (Michilli et al., 2018). It was this FRB's repeating nature that allowed these measurements — knowing the FRB position ahead of time allows for follow-up observations at higher time resolutions. Untargeted surveys for FRBs with positions unknown *a priori* (i.e. all non-repeaters) that rely on offline searches for bursts within their data are limited by storage requirements and processing speeds and therefore typically are restricted to time resolutions $\gtrsim 1$ ms.

The ability to detect FRBs in real time can allow an instrument to avoid this restriction. In this way, the UTMOST project at the Molonglo Observatory Synthesis Radio Telescope detected FRB 20170827A and collected data at a time resolution of 10.24 µs showing the burst to have a complex temporal profile with structure as narrow as ~ 30 µs (Farah et al., 2018). These were the first high-time resolution measurements of an apparently non-repeating FRB.

The Australian Square Kilometre Array Pathfinder (ASKAP) has made high-

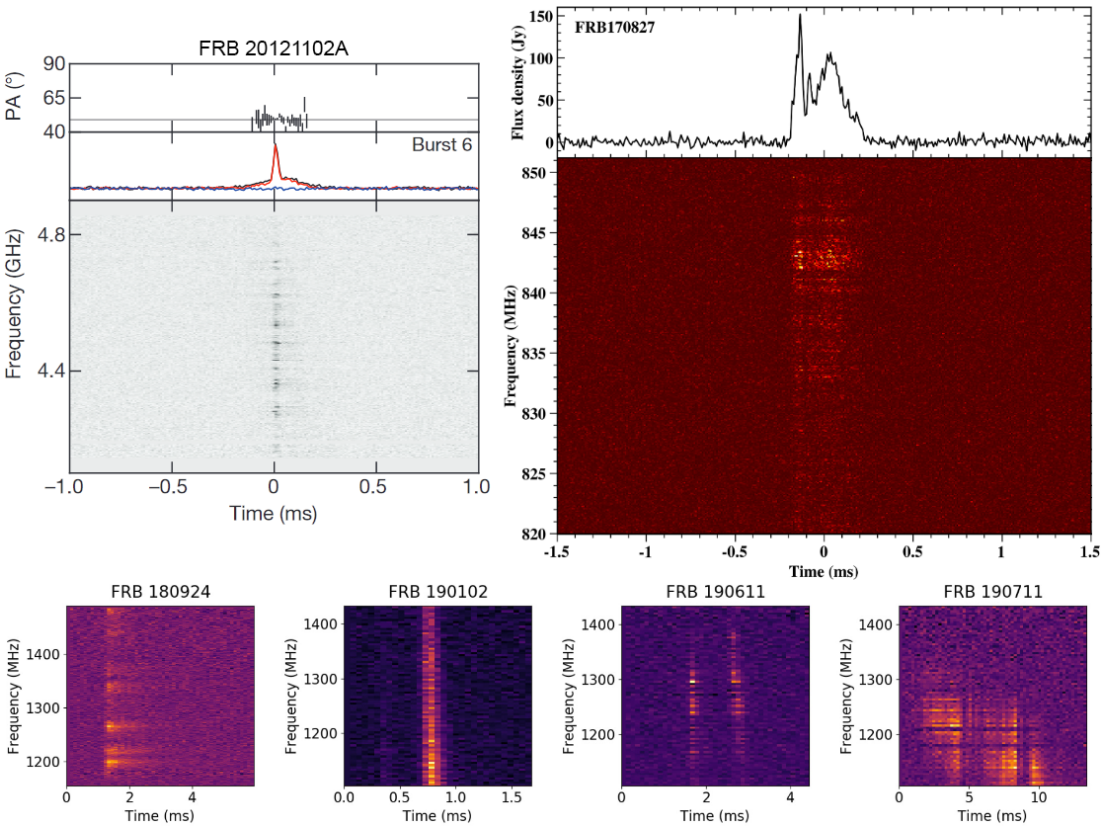

Figure 1.1: A selection of high-time resolution FRB data. Top left: Polarisation angle, integrated polarisation profiles (total intensity, linear polarisation, and circular polarisation in black, red, and blue respectively), and dynamic spectrum of a burst from the repeating FRB 20121102A as recorded by Arecibo (adapted from Michilli et al. 2018). Top right: Integrated profile and dynamic spectrum of FRB 20170827A as recorded with UTMOST (adapted from Farah et al. 2018). Bottom row: the dynamic spectra of four FRBs detected with ASKAP (adapted from Day et al. 2020).

time resolution measurements of several FRBs via real-time detection since 2018 (Cho et al., 2020; Day et al., 2020; Bhandari et al., 2022) (see §2.2). Notably, ASKAP is able to produce polarimetric data at time resolutions as fine as ~ 3 ns. The Deep Synoptic Array (DSA) and Canadian Hydrogen Intensity Mapping Experiment (CHIME) are similarly capable of real-time detection and have recently released samples of non-repeating FRBs with time resolutions on the order of microseconds (Sherman et al. 2024 and CHIME/FRB Collaboration et al. 2023a, respectively).

In many cases, high-time resolution data reveals burst structures that would be inaccessible with > 1 ms time resolution. High time resolutions will therefore be essential for deepening our understanding of FRBs and their emission processes. Two examples of the application of high-time resolution to interrogating the FRB emission mechanism(s) follow.

Nimmo et al. (2022) showed isolated "shots" of emission from the repeating FRB 20200120E with timescales from ~ 60 ns to 5 µs. These timescales imply a physical emission region no larger than 1500 m (ignoring relativistic beaming effects; see §1.6.2), and paired with the measured luminosities link repeating FRBs to pulsar giant pulse emission in transient luminosity-duration phase space, suggesting a magnetically powered emission mechanism common to repeating FRBs, the Crab pulsar, and the magnetar SGR 1935+2154.

Hewitt et al. (2023) identify two distinct morphological features in high-time resolution dynamic spectra of bursts from the repeating FRB 20220912A: "forests" of bright, broadband microshots with ~ 16 µs durations, and broader sub-bursts with more restricted spectral occupancy that tend to drift downwards across the duration of a burst. These features are proposed to have possibly arisen from different emission processes.

1.2 Polarimetric properties

Similarly to high-time resolution data, polarimetric measurements of FRBs are often not possible when performing offline data searches. High-time resolution data is typically polarimetric (although polarimetric data is not always at high time resolutions), so real-time burst detection is also relevant to performing studies of the polarisation properties of FRBs.

A small number of the earliest FRB discoveries included measurements of polarisation properties, and showed that FRBs could be significantly linearly and/or circularly polarised (Petroff et al. 2019, and see Table 1 from Caleb et al. 2018). As the number of bursts with measured polarisations has grown, it seems FRBs usually have some significant degree of linear polarisation, and less often are circularly polarised, with linear and circular polarisation occasionally appearing together. Zhang (2022) draws on many examples sketching out these trends, to which should now be added the much larger samples of Sherman et al. (2024) and Pandhi et al. (2024).

Conversion between linear and circular polarisation over time has been observed within burst components (e.g. FRB 20181112A, Cho et al. 2020) and between burst components (e.g. FRB 20190611B, Day et al. 2020). Conversion over frequency has also been measured (e.g. FRB 20201124A, Xu et al. 2022; Kumar et al. 2023). These variations allow for features of the magnetic field and environment local to FRB progenitors to be examined. For instance, Xu et al. (2022) suggest that frequency-dependent oscillations in the polarisation of bursts from the repeating FRB 20201124A could demonstrate that the source's immediate environment contains both cold and relativistic plasmas with a strong but variable magnetic field.

Feng et al. (2022) showed a trend towards lower linear polarisation fractions in FRBs at lower frequencies. They explain this by arguing that multipath propagation (stronger at lower frequencies; §1.3.2) through a complex magnetic field environment results in "rotation measure (RM) scatter", which depolarises

the FRB radiation (see §1.3.3 for more on RMs, which are closely related to polarisation properties). They go on to propose that the degree of RM scatter could be used as an indicator of the age of the stellar population an FRB source is embedded within.

The polarisation position angle (PA) of bursts also has varying behaviour, being observed to be stable in some bursts (e.g. Michilli et al. 2018; Day et al. 2020) and rapidly varying in others (e.g. Luo et al. 2020; Cho et al. 2020). Luo et al. (2020) argue that the PA variations they report are more likely intrinsic to the emission process rather than being determined by propagation effects, and point out that this would favour pulsar-like models locating the emission source in a neutron star magnetosphere over models involving synchrotron masers.

1.3 Propagation effects

All interstellar and intergalactic space contains some medium through which electromagnetic radiation travels — the interstellar medium (ISM) and intergalactic medium (IGM). These media do not allow the radiation to pass through unaffected, but impose certain changes and distortions onto it. Despite their low densities (of order $10^{-3} - 10^{6}$ particles per cm^3 in the ISM (Ferrière, 2001) and one particle per m^3 in much of the IGM (Nicastro et al., 2008)), the immense distances radiation must travel through the ISM and IGM mean the propagation effects become significant. The particular way these effects manifest is dependent on the nature of the medium and the signal.

The short durations and typically broadband spectra of FRBs mean the effects of propagation are an essential consideration when searching for and analysing them. Summarised here are the most significant: dispersion, scattering, scintillation, and Faraday rotation.

1.3.1 Dispersion

Ionised media, like the ISM and the IGM, impose a frequency-dependent refractive index μ on electromagnetic radiation propagating through them. Because $\mu < 1$, the group velocity $v_g = \mu c$ of the radiation will be reduced, and a delay proportional to the inverse square of frequency will be produced:

$$\Delta t_{\mathrm{DM}} = \left(f_2^{-2} - f_1^{-2}\right) \frac{\mathrm{DM}}{k_{\mathrm{DM}}}, \tag{1.1}$$

where Δt_{DM} is the delay imposed on radiation with frequency f_2 relative to radiation of frequency f_1, k_{DM} is the dispersion constant

$$k_{\mathrm{DM}} = \frac{2\pi m_e c}{e^{-2}} \approx 2.41 \times 10^{-4}\,\mathrm{pc\,cm^{-3}\,GHz^{-2}\,\mu s^{-2}}, \tag{1.2}$$

and DM is the dispersion measure (typically expressed with units of $\mathrm{pc\,cm^{-3}}$), defined as the integrated column density of electrons along the line of sight:

$$\mathrm{DM} = \int_0^d n_e(l)\, dl, \tag{1.3}$$

where $n_e(l)$ is the density of electrons along the path from the Earth ($l = 0$) to the source of the radiation ($l = d$) (Lorimer & Kramer, 2005). The dispersive delay is also representable in the spectral domain as a frequency-dependent phase rotation, which allows for the reversal of dispersion if one has measurements of a signal's electric field ("coherent dedispersion").

The short duration and large distances of FRBs makes dispersion a very significant effect. For example, over ASKAP's 336 MHz bandwidth centred on ∼1 GHz, the difference in arrival time between the top and bottom of the band can be on the order of seconds. The frequency-dependent "sweep" of an FRB over time is shown in Figure 1.2.

Because the DM of a burst is a function of the integrated electron density along the path of travel, it can be used to draw conclusions about the density

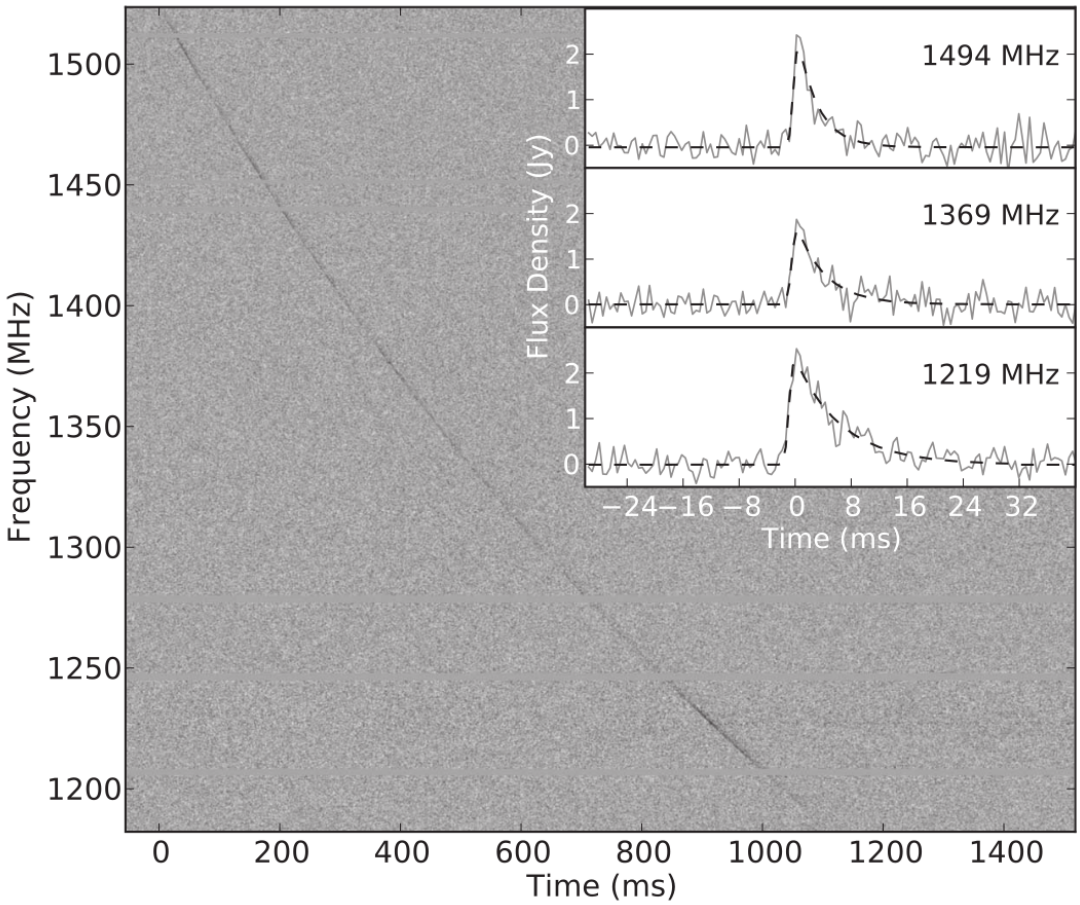

Figure 1.2: Dynamic spectrum of FRB 20110220A showing the frequency-dependent dispersive sweep over time. Inset: time profiles integrated over 25 MHz-wide bands at the top, centre, and bottom of the bandwidth. Solid grey lines are the data, dashed black lines are best fits. Figure reproduced from Thornton et al. (2013).

and location of electrons in the FRB's immediate host environment (Chittidi et al., 2020), host galaxy (Caleb et al., 2023a), and halos of intervening galaxies (Prochaska et al., 2019; Simha et al., 2023).

The intergalactic medium (IGM) makes a contribution $\mathrm{DM_{cosmic}}$ to an FRB's total DM, the expected value of which is:

$$\langle \mathrm{DM_{cosmic}} \rangle = \int_0^{z_{\mathrm{FRB}}} \frac{c\bar{n}_e(z)\ dz}{H_0(1+z)^2\sqrt{\Omega_m(1+z)^3+\Omega_\Lambda}}, \tag{1.4}$$

where z_{FRB} is the FRB redshift, $\bar{n}_e(z)$ is the mean electron density, H_0 is the Hubble constant, and Ω_m & Ω_Λ are the matter & dark energy densities of the Universe (Macquart et al., 2020). Consequently, measuring the DM–z distribution of FRBs (the Macquart Relation) allows for constraints on these macroscopic properties of the Universe. Macquart et al. (2020) measured the Macquart Relation for the first time and applied it to confirm the density of invisible electrons in the IGM is consistent with estimations of the primordial baryonic content of the Universe inferred from cosmic microwave background measurements (Planck Collaboration et al., 2016) and big bang nucleosynthesis (Cooke et al., 2018). These baryons had never been directly observed before, and this resolved the "missing baryon problem" (McQuinn, 2013). James et al. (2022) applied the Macquart Relation to measure H_0, and showed that a sample of ~ 100 FRBs with z measurements could potentially resolve the Hubble tension.

1.3.2 Scattering and scintillation

A medium with inhomogeneous electron density will shift the phase of a wave randomly as it propagates. This effectively means that the wavefront will be deformed so that rays originally not on a path towards an observer are redirected into the observer's line of sight. The source will be observed to have been broadened into a small diffuse disk on angular radius θ_d. Rays from a source at a distance d

that have been deflected by an angle θ will experience a geometric delay

$$\Delta t_{\rm scatt} = \frac{\theta^2 d}{c}. \tag{1.5}$$

An impulsive signal such as an FRB is therefore temporally scatter-broadened with an exponential tail:

$$I(t) \propto \exp\left(-\frac{t}{\tau_s}\right), \tag{1.6}$$

where τ_s is the scattering timescale:

$$\tau_s = \frac{\theta_d^2 d}{c} \propto f^{-4} \tag{1.7}$$

(Lorimer & Kramer, 2005). The inset of Figure 1.2 shows the exponential broadening of an FRB, and the frequency dependence of scattering with lower frequencies experiencing significantly more broadening.

The phase rotations induced by inhomogeneous media resulting in scattering will also produce interference between scattered waves whose phase differs by no more than about a radian. This interference will produce scintillation: variations in the intensity of an FRB's spectrum on the scale of the "decorrelation bandwidth" $f_{\rm DC} \propto 1/\tau_s \propto f^4$ (Lorimer & Kramer, 2005). An example of this is shown in Figure 1.3.

Scattering and scintillation are often approximated as taking place as radiation passes through a single scattering screen of inhomogeneous electron density. The geometry of the screen relative to the source and observer determines the precise manifestation of scattering and/or scintillation in a burst profile and spectrum. Measurements of scattering and scintillation in FRBs has been used to identify the likely presence of multiple scattering screens in some cases (Sammons et al., 2023).

FRBs are observed to have a wide variety of scattering timescales and degree of scintillation, implying that FRBs are not all emitted from turbulent, high-density environments.

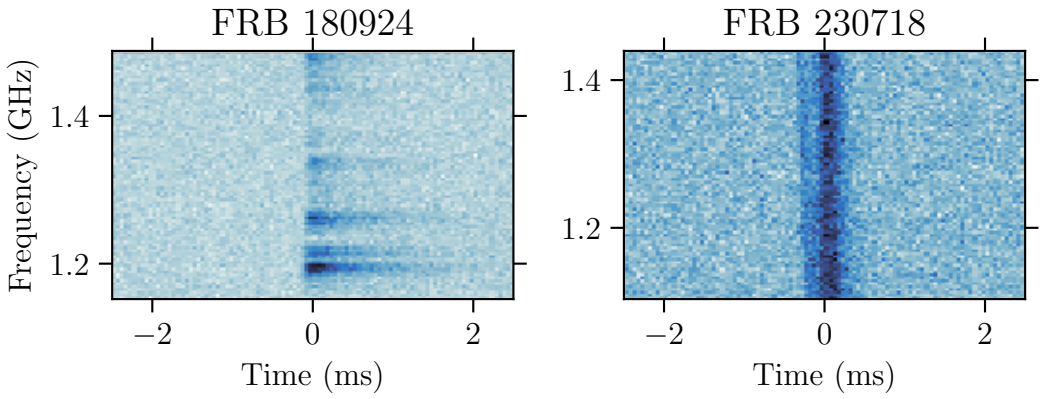

Figure 1.3: Dedispersed dynamic spectra of FRB 20180924A (left) and FRB 20230718A (right), plotted with time resolution 50 µs and frequency resolution 4 MHz. The left spectrum is heavily scintillated and scatter-broadened, while neither effect is significant in the right spectrum.

1.3.3 Faraday rotation

If radiation travels through a cold electron-ion plasma with a magnetic field B, the component parallel to the direction of travel $B_\parallel$ will induce a rotation of the PA:

$$\Delta\psi_{\mathrm{PA}} = \lambda^2 \mathrm{RM}, \tag{1.8}$$

where λ is the wavelength, and RM is the rotation measure:

$$\mathrm{RM} = \frac{e^3}{2\pi m_e^2 c^4} \int_0^d n_e(l) B_\parallel(l)\, dl, \tag{1.9}$$

(Lorimer & Kramer, 2005) (note that relativistic and electron-positron plasmas give rise to different effects). The fraction RM/DM therefore is a measure of the net magnetic field parallel to a burst's path of travel and can be used to probe extragalactic magnetic fields (Akahori et al., 2016; Prochaska et al., 2019; Mannings et al., 2023).

The values of RM measured in FRBs vary widely. Many have RMs close to zero, and FRB 20121102A has a measured RM $\sim 10^5\,\mathrm{rad\,m^{-2}}$ (Michilli et al., 2018). The RMs of some repeating FRBs have been observed to change over

time in a variety of ways, including decaying magnitudes (Michilli et al., 2018), short-term fluctuations (Luo et al., 2020; Xu et al., 2022), and a complete sign change (Anna-Thomas et al., 2023). As is the case for the diverse and sometimes variable (assumed) intrinsic polarisation features of FRBs (§1.2), the distributions and variations in burst RMs have implications for the nature of magnetic fields and environments around the progenitors.

1.4 Repeaters and non-repeaters

Among the observed FRB population, a small number of sources have been observed to produce more than one burst ("repeaters"). The first such source was FRB 20121102A (Spitler et al., 2016), and to date several dozen sources have been identified that have emitted more than one FRB. The fraction of repeating sources out of the general population is small; CHIME/FRB Collaboration et al. (2023b) report that in the sample of FRB sources observed with CHIME/FRB, currently the instrument with the highest detection rate, the fraction that repeat is tending to $2.6^{+2.9}_{-2.6}\%$.

Repeaters are not seen to produce bursts with regular periodicity. However, some are observed to have activity cycles. Bursts from FRB 20180916B arrive within a 4.0-day phase window that comes around every 16.35 ± 0.18 days (CHIME/FRB Collaboration et al., 2020a), and FRB 20121102A has been found to have an activity cycle with a periodicity of 161 ± 5 days (Rajwade et al., 2020; Cruces et al., 2021). FRB 20180916B's activity window has been found to be frequency-dependent, with lower-frequency bursts appearing later in the activity cycle (Pastor-Marazuela et al., 2021; Pleunis et al., 2021b).

There is evidence that repeating FRBs and non-repeating FRBs are distinct phenomena. Pleunis et al. (2021a) show that, of bursts in the First CHIME/FRB Catalog (CHIME/FRB Collaboration et al., 2021), one-off bursts and bursts from repeater sources have distinct distributions of burst duration and bandwidth, shown in Figure 1.4, with one-off bursts tending to be shorter and more broadband.

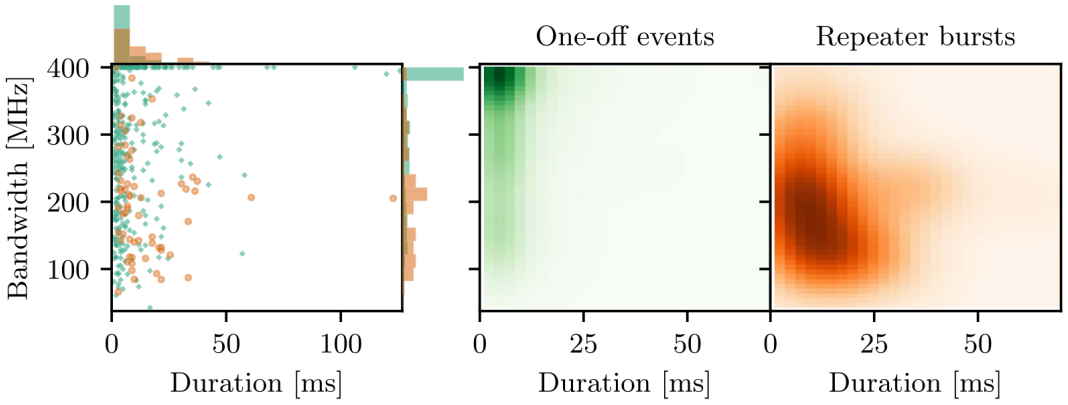

Figure 1.4: Bandwidths and durations of FRBs with detection S/N > 12 in the First CHIME/FRB Catalog (CHIME/FRB Collaboration et al., 2021). The left panel shows each FRB, with one-off bursts in green and bursts from repeaters in orange. The centre and right panels show smoothed and normalised distributions of the one-off bursts and repeater bursts respectively. Figure reproduced from Pleunis et al. (2021a).

They also identify that repeaters in their sample tend to have downward spectral drifts across burst components (the "sad trombone" shape), and never have broadband and single-peaked morphologies. CHIME/FRB Collaboration et al. (2023b) reinforce this distinction, and show that there may also be a difference in the distribution of burst DMs between repeaters and non-repeaters in their sample.

Bhandari et al. (2022) found no statistically significant difference between host galaxies of repeaters and non-repeaters, although the sample size of FRB host galaxies with detailed measurements of their properties available remains small (only 16 galaxies were used in this study). There is also no apparent distinction between the polarisation properties of repeaters and non-repeaters (Zhang, 2022).

1.5 Host galaxy associations

While the large DMs of FRBs relative to models of the DM contribution of the Milky Way (such as NE2001, Cordes & Lazio 2003, and YMW16, Yao et al. 2017) are alone enough to deduce that FRBs are extragalactic, identifying the

host galaxy of an FRB is generally non-trivial. Most single-dish FRB-detecting instruments do not have spatial resolution on the order of arcseconds, which is in most cases necessary to localise a single burst to a single galaxy. Without performing interferometry, beam sizes at radio frequencies are typically simply too large to permit precise enough localisation. Where single-dish instruments are large enough to have the required precision, for example the Five-hundred-meter Aperture Spherical Telescope (Zhu et al., 2020), this comes at the cost of greatly sacrificing their field of view and therefore their burst discovery rate.

For multi-antenna instruments, the large volumes associated with interferometric data prohibit straightforward surveys, where data over a long period of time is saved for an offline untargeted search. FRB sources that have rough positions measured can be followed up to search for repetitions, but if the burst does not repeat there will be no further opportunity to refine the position. FRB 20121102A was localised and associated with a host galaxy via follow-up interferometric observations of repeat bursts (Chatterjee et al., 2017). Putative association of one-off burst with a fading radio transient (Keane et al., 2016) and the low DM of another non-repeater (Mahony et al., 2018; Lee-Waddell et al., 2023), both poorly localised, permitted likely — but not unambiguous — association with host galaxies.

In order to obtain arcsecond-precision localisations of non-repeating bursts, an interferometer must be able to detect FRBs in real time in order to capture the required data containing the burst signal. The instruments currently capable of this are ASKAP (Bannister et al. 2019b; elaborated on in Chapter 2), the DSA (Ravi et al., 2019), CHIME (Cassanelli et al., 2023), MeerKAT (Driessen et al., 2023), and the Very Large Array (VLA; Law et al. 2020).

At the time of writing, 51 FRB sources have been linked to host galaxies (listed in Supplementary Table A.1). Identifying the host galaxies of FRBs permits detailed follow up of the properties of these galaxies, which can have implications on the likelihood of progenitor and emission models, and their redshifts, which

can be applied to cosmology studies.

Bhandari et al. (2022) examine the distribution of host properties with a sample of 16 galaxies, finding that FRBs tend to originate in galaxies with moderate star formation and are more rare in galaxies without it. They found no significant differences between the galaxies of repeating and non-repeating FRBs, nor any difference between FRB hosts and galaxies hosting core-collapse supernovae or short gamma-ray bursts, and that the distribution of FRB distances from the centre of their hosts does not match that for neutron stars and globular clusters.

1.6 Current constraints and models

1.6.1 Progenitors

While there is no absolute consensus on what objects produce FRBs, neutron stars are the most widely favoured candidate. In particular, there is evidence to support a magnetar (neutron stars with surface magnetic fields in excess of 10^{14} G, Duncan & Thompson 1992) progenitor for many FRBs. The most compelling evidence for this is the observation of FRB-like emission from Galactic magnetar SGR 1935+2154 (CHIME/FRB Collaboration et al., 2020b; Bochenek et al., 2020). The energy of this emission was more than an order of magnitude smaller than the dimmest FRBs, but the morphological and spectral similarities (Figure 1.5) have led many to conclude that even if not all FRBs are produced by magnetars, at least some must be (Bailes, 2022). The 216.8 ms periodicity observed within FRB 20191221A by CHIME/FRB Collaboration et al. (2022) is consistent with an origin in the magnetosphere of a neutron star (and therefore also magnetar), although the long (~ 3 s) duration of this FRB makes it an outlier of the general population. The association of the repeater FRB 20200120E with a globular cluster in M81 (Bhardwaj et al., 2021a) is not inconsistent with a recently-formed magnetar, but could also indicate an origin from a millisecond pulsar, which are prevalent in globular clusters (Bailes, 2022).

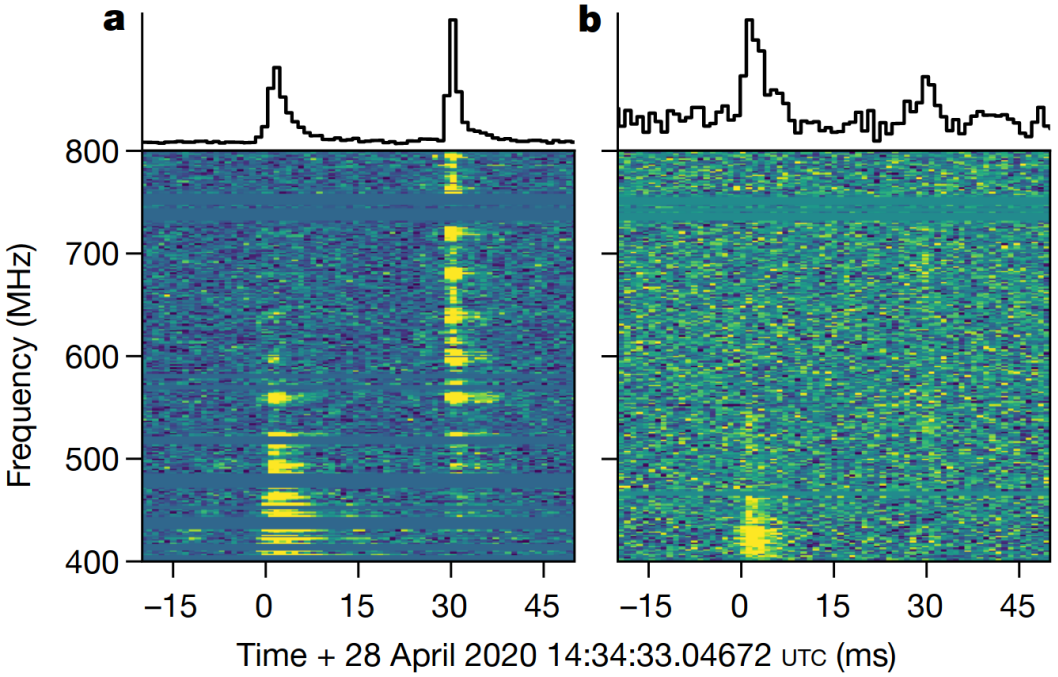

Figure 1.5: Dedispersed dynamic spectra and integrated profiles of FRB 200428, as detected by CHIME/FRB (left) and the Algonquin Radio Observatory (right). Figure reproduced from CHIME/FRB Collaboration et al. (2020b).

The existence of repeating FRBs completely rules out cataclysmic events such as supernovae and neutron star/black hole mergers as producers of those FRBs. The periodic activity cycles of some repeaters implies some sort of rotation at the burst sources, either from an extremely long period of rotation or precession of the progenitor, or the orbit of a binary system in which one of the bodies emits bursts in such a way that they are only observable from Earth at certain points in the orbit (e.g. due to orbital phase-dependent absorption due to the wind of a massive compantion star (Lyutikov et al., 2020)). Pastor-Marazuela et al. (2021) argue the chromatic activity phases of FRB 20180916B discredit a simple binary model and that there is no compelling evidence for precession, instead favouring an ultra-long-period magnetar.

It is difficult to demonstrate that non-repeating FRBs are intrinsically one-off, as opposed to simply having extremely low repetition rates or emitting more bursts at much lower energies than the burst of initial detection, but it remains a

possibility. There is theoretical support for the emission of FRBs from mergers of neutron stars or other cataclysmic events (e.g. Totani 2013; Zhang 2020; §VI.F of Zhang 2022), and Moroianu et al. (2023) show a possible association (2.8σ) between the non-repeating FRB 20190425A and GW190425, a gravitational wave event produced by a binary neutron star merger.

1.6.2 Emission mechanisms

There are less specific clues as to the physics of the emission mechanism(s), but some constraints can be determined. The large brightness temperatures ($\gtrsim 10^{35}$ K) are hugely in excess of any thermal temperature known to be reached by any physical process, as well as that allowed in synchrotron radiation (Kellermann & Pauliny-Toth, 1969). It is therefore generally accepted that the emission process must be a coherent one (Melrose, 2017; Zhang, 2022).

Measuring the intrinsic duration (i.e. after accounting for broadening due to scattering, §1.3.2, and any instrumental effects) of a burst can put an upper limit on the size R of the region from which it is emitted. This is because emission from the far side of this region has to travel for a slightly longer time R/c, which becomes a lower limit on the intrinsic width of the burst W. Therefore, if W is measured, we can determine that $R \lesssim cW$ (Zhang, 2022). Nimmo et al. (2022) measured burst component timescales of ~ 60 ns to 5 µs in FRB 20200120E, implying an upper limit on the emission regions of these components of 20-1500 m. They conclude that this emission cannot be from a synchrotron maser in a relativistic shock, and instead propose a magnetospheric origin, as this would be consistent with the ~ 0.4 ns duration nanoshots observed in giant pulses from the Crab pulsar (Hankins & Eilek, 2007). This is consistent with the conclusions Luo et al. (2020) draw from the varying PA behaviour observed in some FRBs (§1.2).

Existing models for FRB emission within these constraints are extensive, and well summarised by §V of Zhang (2022).

1.7 The future of FRB science

The field of FRB science has moved well beyond the era where simply observing bursts sparingly can help us to answer many of the unanswered questions concerning their nature. The value of single detections has depreciated, unless the FRB in question is measured in high detail (e.g. as in Cho et al. 2020; Nimmo et al. 2022; Hewitt et al. 2023), or can be associated with a known object (e.g. a magnetar, CHIME/FRB Collaboration et al. 2020b; Bochenek et al. 2020) or other type of transient event (such as a gravitational wave, Moroianu et al. 2023).

The study of the *population* of FRBs is being enabled by instruments with high detection rates such as CHIME (CHIME/FRB Collaboration et al., 2021), and the now steadily increasing number of host galaxies being identified by the precise localisations of DSA, MeerKAT, VLA, and ASKAP. This is beginning to paint a picture of what type of galaxies FRBs come from, and therefore what their progenitors are likely to be, as well as giving us a new probe of cosmological parameters via the Macquart Relation.

ASKAP is currently the only instrument able to both make a major contribution to host galaxy identification, due to its localisation capabilities plus moderate field of view, and simultaneously produce extremely high-time resolution ($\sim$3 ns) polarimetric data of every burst it observes upon first detection. The next chapter describes ASKAP and its capabilities in relation to observing FRBs.

Chapter 2

ASKAP

The Australian Square Kilometre Array Pathfinder (ASKAP; Hotan et al. 2021; shown in Figure 2.1) is a radio interferometer at Inyarrimanha Ilgari Bundara, the Murchison Radio-astronomy Observatory, on Wajarri Country in Western Australia. It is made up of 36 dishes, each with a diameter of 12 m, and observes with a 336 MHz bandwidth between 0.7 and 1.8 GHz. ASKAP is a precursor instrument to the Square Kilometre Array (SKA), the SKA-Low part of which will be built on the same site. ASKAP was designed primarily to maximise the rate of surveying large areas of the sky, and has proven an effective instrument for detecting FRBs through the Commensal Real-time ASKAP Fast Transients (CRAFT) Survey (Macquart et al., 2010).

Each of ASKAP's antennas is equipped with a phased array feed (PAF) composed of 188 individual receivers arranged in a checkerboard pattern, which allows the formation of 36 dual-linear-polarisation beams and a $\sim$ 30 degree field of view (Hotan et al., 2021). The beams can be rearranged to overlap with each other, which improves the localisation precision of fast transients by allowing the triangulation of the position based on the strength of detection across multiple adjacent beams. The data from each PAF is processed by an oversampled polyphase filterbank (PFB; §2.2.2) to coarsely channelise the data into 1 MHz channels of complex voltages (complex-valued electric field samples)

Figure 2.1: ASKAP. Image reproduced from Hotan et al. (2021).

in each polarisation, representing the electric field measured by each beam of each antenna at the bandwidth-determined sampling rate of $(336\,\mathrm{MHz})^{-1} \approx 2.976\,\mathrm{ns}$. These voltages go on to be processed depending on the specific requirements of the observation being made.

For fast transient searches (such as that done by CRAFT), the voltages are squared and summed across polarisations, then integrated over $\sim$1 ms to obtain "incoherent sum" (ICS) dynamic spectra across all beams and antennas. These are then searched with the Fast Real-time Engine for Dedispersing Amplitudes (FREDDA; Bannister et al. 2019a), which implements the Fast Dispersion Measure Transform (FDMT; Zackay & Ofek 2017). FDMT transforms intensities in frequency-time space into Δt_{DM}-time space, where Δt_{DM} is the expected time delay between the top and bottom of a frequency band due to dispersion quantified by DM. An example input and output of FDMT is shown in Figure 2.2. FDMT allows for highly efficient searching of frequency-time data for fast transients strongly affected by dispersion, including FRBs. FREDDA applies FDMT to

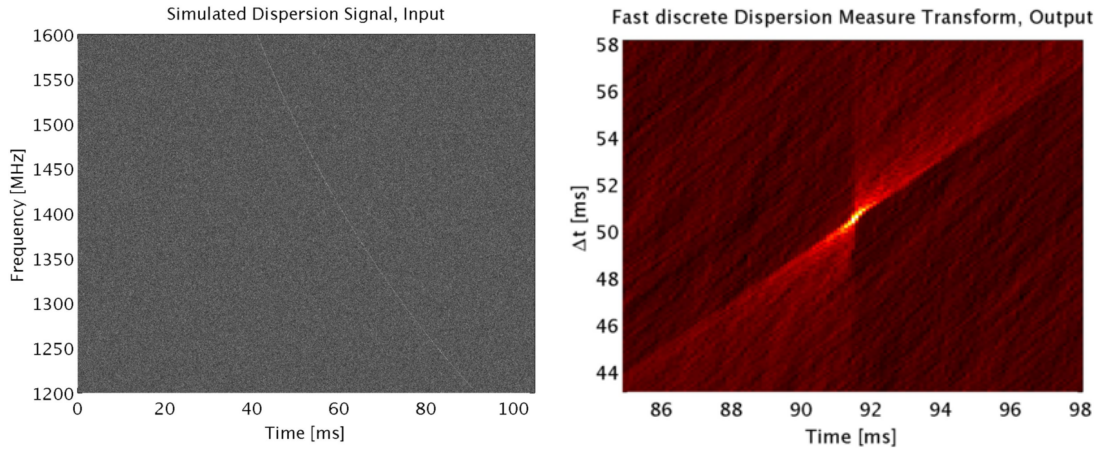

Figure 2.2: Simulated input dynamic spectrum (left) and zoomed-in FDMT output (right). Figure reproduced from Zackay & Ofek (2017).

the dynamic spectra obtained with ASKAP and searches the output for high signal-to-noise (S/N) candidates across time, DM, and boxcar convolution widths.

2.1 Early FRB searches

The early FRB detections with ASKAP (Bannister et al., 2017; Shannon et al., 2018) were made in offline searches of ICS data at 1.265 ms time resolution. The data was collected with ASKAP in the "fly's eye" configuration, where all in-use antennas point in different directions to improve the total field of view and detection rate. The dynamic spectrum and integrated time profile of FRB 20170117A, the first FRB detected by ASKAP (Bannister et al., 2017), are shown in Figure 2.3.

Because these bursts were discovered in offline post-processing searches, no further data could be recovered, limiting the time and frequency resolutions to those of the ICS data, the localisation precision to of order arcminutes, and preventing any polarimetric analysis. Even with these limitations, the sample made significant contributions to FRB science.

The fluences and DMs of the ASKAP FRBs showed a relationship between burst brightness and degree of dispersion within the FRB population observed

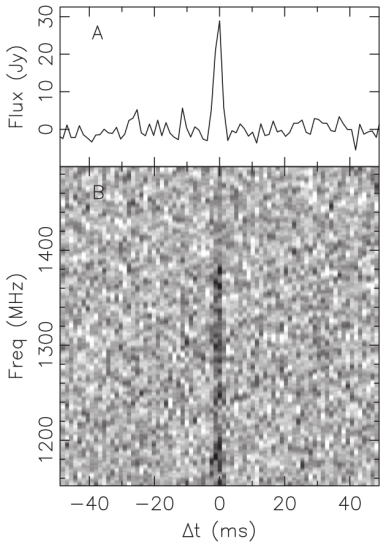

Figure 2.3: Frequency-integrated time profile (top) and dynamic spectrum (bottom) of FRB 20170117A. Figure reproduced from Bannister et al. (2017).

until that point, with brighter bursts tending to have lower DMs — confirming that DM is a proxy for distance (Shannon et al., 2018). FRB 20171020A had such a low DM ($114\,\mathrm{pc\,cm^{-3}}$) that a likely host galaxy could be identified, making it the first non-repeating FRB to be associated with a host galaxy, and the second of any FRB (following only the first repeater FRB 20121102A) (Mahony et al., 2018; Lee-Waddell et al., 2023).

2.2 Real-time FRB detection and voltage capture

As the voltages are formed into the ICS dynamic spectra, they are also recorded into ring-buffers that constantly update to contain the most recent 3.1 s of voltage data in each beam and antenna. In 2018, ASKAP was enabled to detect FRBs in real-time using FREDDA with sufficiently low latency to freeze and save the voltages in these buffers while they still contain the signal of an FRB. With the ASKAP antennas arranged in interferometric mode instead of fly's-eye, where the antennas have the same pointings, having access to these raw voltages allows for

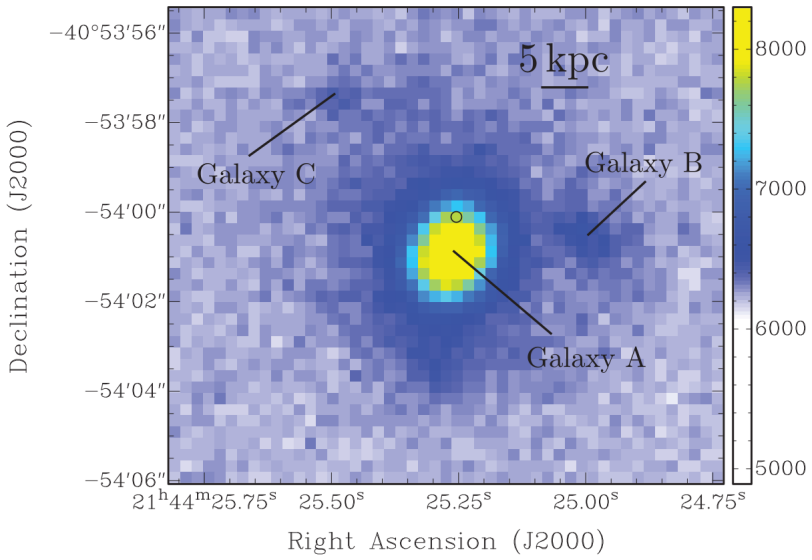

Figure 2.4: Very Large Telescope (VLT) image of FRB 20180924A's host galaxy, with the localisation region of the burst itself shown by the black circle. Figure reproduced from Bannister et al. (2019b).

interferometric localisation of FRBs upon their first detection (Bannister et al., 2019b), and polarimetric analysis of burst signals at high time resolution via coherent beamforming (Cho et al., 2020).

2.2.1 Burst localisation

The saved voltages can be correlated, calibrated, and imaged with various astronomy software to produce high-precision (sub-arcsecond) localisations of an FRB. DiFX (Deller et al., 2011) is used for correlation, and calibration & imaging are done with the Astronomical Image Processing System (AIPS; Greisen 2003) and the Common Astronomy Software Applications (CASA; CASA Team et al. 2022) (Bannister et al., 2019b).

FRB 20180924A was the first FRB to be directly localised with ASKAP, as well as being the first non-repeating FRB to be unambiguously associated with a host galaxy (Bannister et al., 2019b). An image of this host galaxy is shown in Figure 2.4.

To date, 18 FRBs detected with ASKAP have been localised to host galaxies

(Bannister et al., 2019b; Prochaska et al., 2019; Macquart et al., 2020; Heintz et al., 2020; Bhandari et al., 2020b, 2022; James et al., 2022; Bhandari et al., 2023; Gordon et al., 2023; Ryder et al., 2023; Glowacki et al., 2024), and the host galaxy of one further precisely-localised burst has evaded detection, implying a high redshift origin (Marnoch et al., 2023).

2.2.2 Coherent beamforming

Because the voltages saved are the direct outputs from the PFBs and have had no further integration or reduction applied to them, they can be used to reconstruct a measurement of the complex electric field of an FRB in both linear polarisations sampled at $\sim$3 ns, the maximum sampling rate permitted by the bandwidth, and coherently summed across antennas to grant a massive boost to signal-to-noise. This is the rawest measurement of a burst possible with a radio interferometer ("rawest" in the sense that the least information has been removed or corrupted by processing). Having access to the complex electric field allows not only for studies of burst properties, including polarimetric properties, at very high time and frequency resolutions, but also permits the near-perfect removal of the effects of dispersion via coherent dedispersion (Cho et al., 2020).

However, the voltages as recorded have been coarse-channelised. This has not removed any information, but PFB inversion must be applied to recover the full electric field measurements. ASKAP's PFBs are oversampled, meaning that each coarse channel is responsive to a frequency range B_{OS} that is wider than the channel separation B_C, as shown in Figure 2.5. The design is such that the regions of overlapping frequency response between adjacent channels is the part of each channel's response that tapers off, an unavoidable feature of the channelisation process. By trimming these overlapped regions of each channel and stitching the remaining, flat-response regions together, an artifact-free complex fine spectrum can be constructed across the entire 336 MHz bandwidth (Morrison et al., 2020).

Once these complex fine spectra have been created in both polarisations of

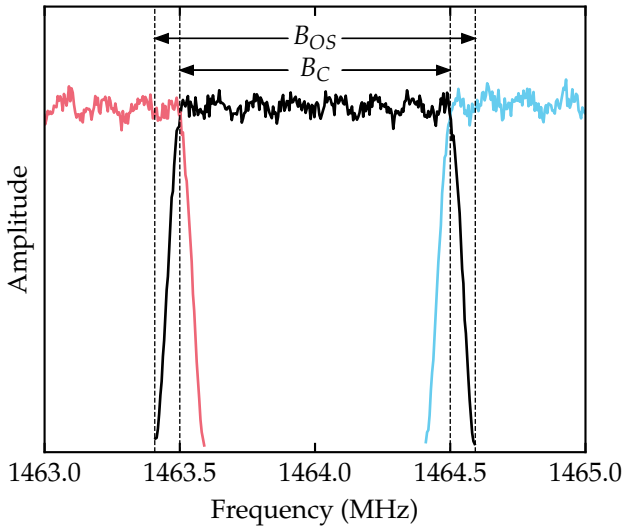

Figure 2.5: Spectral amplitudes of CRAFT voltages pre-PFB inversion in three adjacent coarse channels. B_C is the coarse channel separation/bandwidth and B_{OS} is the oversampled bandwidth. Figure reproduced from Scott et al. (2023).

each antenna, coherent beamforming is applied. This is the process of applying antenna-dependent geometric delays to the spectra, calculated from the localised sky position of the burst. This exactly lines up the arrival time of an FRB between antennas so that when the spectra are summed together, the signals add coherently and the S/N is maximised (Cho et al. 2020; Scott et al. 2023; Chapter 4).

The ultimate products are the coherently-summed complex fine spectra in the X and Y linear polarisations. These can then be coherently dedispersed (Hankins, 1971) to exactly remove the frequency-dependent dispersive delay (represented in the spectral domain as a frequency-dependent phase rotation), and then inverse Fourier transformed into complex time series data of time resolution $(336\,\mathrm{MHz})^{-1} \approx 2.976\,\mathrm{ns}$. From these, polarimetric profiles in the Stokes parameters can be constructed as simple time series or flexibly-shaped dynamic spectra.

Cho et al. (2020) demonstrated this process as applied to FRB 20181112A, the polarimetric time series profiles of which are averaged to 16 µs time resolution in Figure 2.6. This was the most detailed and high-resolution data published for a non-repeating FRB, and revealed that FRBs can have structure on the

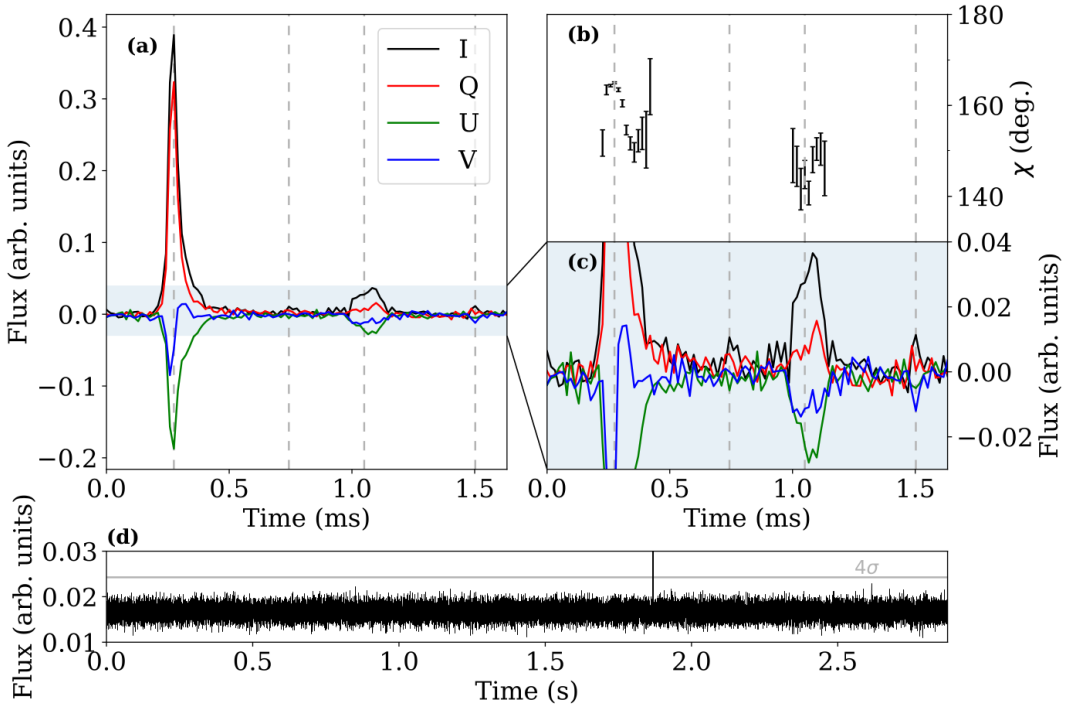

Figure 2.6: Dedispersed, Faraday-corrected, high-time resolution time profiles of FRB 20181112A, revealing four burst components. (a): Stokes parameters at 16 µs time resolution. (b): Polarisation position angle. (c): Zoom-in of panel (a). (d): Intensity time series of the entire voltage buffer. Figure reproduced from Cho et al. (2020).

scale of microseconds. The multiple components within about a millisecond were especially interesting, as at the typically millisecond-level time resolutions that most FRB observations were made such features would be completely hidden.

This data is notable as ASKAP is able to obtain it in principle for *all* FRBs it detects, not just upon the follow-up of repeating FRBs as is the case for most other instruments.

2.3 The CRAFT Coherent Upgrade

Work is currently underway to implement the CRAFT COherent (CRACO)[1] upgrade to ASKAP, which will allow real-time FRB detection to be done with the data output from ASKAP's correlator in the visibility domain. This will boost ASKAP's sensitivity to FRBs and therefore the burst detection rate, currently estimated to approach approximately one FRB every two days (up from approximately one per month).

The acceleration in the detection, localisation, and coherent beamforming of FRBs with ASKAP will require its voltage post-processing pipeline to be robust and highly automated. The development and implementation of this pipeline is the subject of the next two chapters.

[1] dataportal.arc.gov.au/NCGP/Web/Grant/Grant/LE210100107

Chapter 3

Developing the CRAFT voltage processing pipeline

The methods for burst localisation and production of high-time resolution data from ASKAP voltages were initially laid out in Bannister et al. (2019b) and Cho et al. (2020) respectively, with further iterations on the imaging methods presented by Day et al. (2020).

In the early phase of FRB studies with ASKAP voltages, these methods were implemented largely manually, with each step being carefully applied with close human oversight. Such an approach is sensible when a method is new, as the data and its behaviour when processed is yet to be comprehensively understood. Hands-on processing demands the verification that every step is doing what it is supposed to and produces correct results, and is such an important part of establishing a high level of trust in the methodology. However, as the validity and accuracy of the burst localisation and coherent beamforming processes became more certain, and as the number of FRBs with voltages available grew, it became highly desirable to fully automate the processing.

In mid-2020, development of what was to become the CRAFT Effortless Localisation and Enhanced Burst Inspection (CELEBI) pipeline began. The primary goal was to fully automate the production of FRB positions and high-

time resolution data from the dumped voltages with as little human intervention required as possible. The benefits of this include:

- **Faster turnaround from burst detection to precise localisation.** This not only is desirable from the perspective of increasing efficiency, but is also expected to be required to keep up with the increased detection rate with the implementation of CRACO. Additionally, faster processing opens the possibility of rapid FRB follow-up with other instruments to search for counterparts to bursts in other observing regimes, e.g. optical, which requires precise localisation.

- **More reliable results.** Manual processing is prone to human error; an automated pipeline much less so. Results produced in an automated way are more reliable due to being processed in a systematic and well-defined fashion. Automation also revealed human error in previously-processed data products.

- **Clearer definition of the method.** Automating a processing pipeline necessitates the clear, explicit definition of the method being implemented, which has several flow-on benefits:

  - **Easier and more rapid development.** Having a good understanding of the high-level method allows for modifications to that method to be introduced much more easily. This is especially the case with complex pipelines such as CELEBI.

  - **Simpler reproducibility of results.** Manual processing is prone to mistakes and certain steps (e.g. RFI flagging) can have an element of subjective judgement, making exact reproduction of data products difficult if not impossible. By minimising direct human intervention via automation, the method becomes more rigid and objective, and therefore more reliably replicated.

- **Improved logging.** Comprehensive and accurate logging is essential for diagnosing processing errors and bug-fixing. Manual logging can often require as much or more effort than the processing itself, and as such parts that don't seem of immediate importance are often not recorded or saved. Extensive, automated logging at every step of the pipeline ensures nothing is dropped, and that the logs are saved in standardised locations and formats. This in turn makes bug-fixing, increasing pipeline efficiency via resource-use analytics, and verification of intermediate & final data products much easier.

CELEBI's primary phase of development took place over 2020 to 2023, and it continues to undergo improvement in terms of both minor bug-fixes and major features. It is described in full in Chapter 4 (also Scott et al. 2023) and is available publicly on Github[1]. CELEBI is implemented in the pipeline scripting language Nextflow (Di Tommaso et al., 2017), which handles data flow between discrete processes (mostly implemented in Python) and trivialises much of the parallelisation within the pipeline. Nextflow also extensively logs the status of all processes and provides summaries of pipeline performance.

CELEBI has brought about many improvements to CRAFT voltage processing. Pre-CELEBI, an experienced user could spend days performing the processing in quite an involved way to produce burst positions; with CELEBI, positions can be obtained within just a few hours of the data becoming available with minimal direct intervention. The processing methods have evolved and become more robust throughout the development of CELEBI as more FRBs have been observed with specific peculiarities previously not accommodated for. It is also now much easier to onboard new users with CELEBI, as in-depth knowledge of each stage of the pipeline is no longer required to produce results.

The main failure mode of CELEBI is in relation to failed or incomplete voltage downloads, which affected 12 of the 44 bursts detected by ASKAP up until July 18 2023. Ongoing iterative development of CELEBI aims to make it more robustly

[1] github.com/askap-craco/CELEBI

able to handle incomplete or missing data, which will improve the consistency of its applicability.

3.1 Publications assisted by CELEBI

Throughout the development of CELEBI, it has been used to produce results for several publications. The active use of CELEBI has given it a symbiotic relationship with these science outcomes — CELEBI contributes to and improves the results, and the obtaining of these results motivates the development and growth of CELEBI. Listed below are the publications that processing with CELEBI made a contribution to.

Fong et al. (2021): Chronicling the Host Galaxy Properties of the Remarkable Repeating FRB 20201124A

ASKAP detected 11 bursts from the repeating FRB 20201124A over seven days in April 2021, five of which were detected in real-time and had voltages available for processing. Fong et al. (2021) report the localisation from three of these bursts, and present the properties of the FRB's host galaxy. Though still early in development, CELEBI made a significant contribution in allowing the processing of the five sets of voltages to proceed quickly and in a standardised way. This made identification of the issues with two of the data sets (a partial data download resulting in insufficient signal-to-noise of field sources for astrometric correction) simpler.

James et al. (2022): A measurement of Hubble's Constant using Fast Radio Bursts

A sample of 16 FRBs detected with ASKAP, mostly localised with CELEBI, are used to measure the DM-redshift distribution of FRBs (the Macquart relation), which depends on the macroscopic cosmological properties of the Universe, including the Hubble constant H_0. The Macquart relation offers a measure of

H_0 independent of those made from local-universe standard candles and from the Cosmic Microwave Background, which differ from each other at the 4σ level. James et al. (2022) constrain H_0 to $74^{+12}_{-8}\,\mathrm{km\,s^{-1}Mpc^{-1}}$, which is of insufficient precision to support either side of the Hubble tension, but it is shown that a sample of 100 FRBs localised with ASKAP and with measured redshifts (possibly obtainable within only one year of observation with the CRACO upgrade and sufficient optical follow-up) may bring the uncertainty in the measurement low enough to do so ($\lesssim \pm 2.5\,\mathrm{km\,s^{-1}Mpc^{-1}}$).

Ryder et al. (2023): Probing the distant universe with a very luminous fast radio burst at redshift 1

The localisation of FRB 20220610A to a galaxy with a redshift of $z = 1.016 \pm 0.002$ is presented. This is presently the FRB at the furthest known distance and with the highest energy, and provides a probe of the IGM and plasma in the burst host galaxy.

Bhandari et al. (2023): A non-repeating fast radio burst in a dwarf host galaxy

Both the CELEBI-produced localisation and high-time resolution polarimetric profiles of FRB 20210117A are presented. This FRB is apparently non-repeating, but originated in a dwarf galaxy similar to those of known repeaters, and has possible morphological similarities to the repeating population. The low magnetisation of the burst's local environment implied by the polarimetric data and the lack of a persistent radio source distinguish FRB 20210117A from the other repeaters in dwarf galaxies, and could point to the source of this burst being older than the others.

Gordon et al. (2023): The Demographics, Stellar Populations, and Star Formation Histories of Fast Radio Burst Host Galaxies: Implications for the Progenitors

A catalog of the stellar population properties of the host galaxies of 23 FRBs, several newly localised with CELEBI, is presented and analysed. The hosts are diverse in stellar masses, ages, and star formation rates, and no significant difference between the hosts of repeaters and non-repeaters is observed. The results point towards multiple formation channels for FRB progenitors, with most of them likely having short delays between formation and FRB emission (the authors suggest magnetars produced in core-collapse supernova as a possibility) and a small fraction from more delayed channels in environments of low activity.

Sutinjo et al. (2023): Calculation and Uncertainty of Fast Radio Burst Structure Based on Smoothed Data

The high-time resolution analysis enabled by CELEBI's coherent beamforming prompted an investigation into optimising burst DM via structure in the burst profile, rather than the standard method of maximising the measured S/N. These investigations led to the development of a method to measure DM by maximising the sharpness in a smoothed burst profile. Chapter 6 includes a more comprehensive overview of this method.

Baptista et al. (2023): Measuring the Variance of the Macquart Relation in z-DM Modeling

This work measures the Hubble constant H_0 and a parameter F, which measures the fluctuations in the density of baryons in the IGM, via the Macquart relation, now probed with 21 localised FRBs with redshift measurements and a further 57 without localisation. F is related to the width of the Macquart relation, and can be used to make inferences on feedback processes through which baryons are ejected from galactic halos into the IGM.

Sammons et al. (2023): Two-Screen Scattering in CRAFT FRBs

The coherently beamformed data output by CELEBI provide high frequency resolution as well as high time resolution. This work measures the temporal

broadening due to scattering and the spectral fluctuations induced by scintillation to not only measure the strength of these effects, but also to attempt to locate the positions of the scattering screens. Three FRBs are found to have likely passed through two distinct screens. In two of these bursts the position of a screen is limited to within the host galaxy or its circumgalacic medium, and in the third a screen is located at a distance of $\sim 9\,\mathrm{kpc}$.

Marnoch et al. (2023): The unseen host galaxy and high dispersion measure of a precisely-localised Fast Radio Burst suggests a high-redshift origin

The localisation and absence of an observed host galaxy of FRB 20210912A is presented. This is the first FRB localised with ASKAP and with substantial optical and infrared follow-up to result in the non-detection of a host galaxy. The favoured explanation is that the host galaxy is of a typical luminosity relative to the population of observed FRB hosts but is at a high redshift and the burst itself is exceptionally bright, but it is also possible that the host is exceptionally dim and at a closer redshift.

Glowacki et al. (2024): HI FRB, What's Your z: The First FRB Host Galaxy Redshift from Radio Observations

Detection of neutral hydrogen (HI) emission of the host galaxy of FRB 20230718A is used to measure a spectroscopic redshift. This is the first measurement of the redshift of an FRB host with HI emission, bypassing potential dust extinction limiting optical/near-infrared follow-up of FRBs in the Galactic plane. The HI emission also revealed that FRB 20230718A's host galaxy is interacting with a nearby companion.

Chapter 4

CELEBI: The CRAFT Effortless Localisation and Enhanced Burst Inspection Pipeline

Attribution statement

This chapter is the paper "CELEBI: The CRAFT Effortless Localisation and Enhanced Burst Inspection Pipeline", published in Astronomy & Computing Volume 44. CELEBI was designed, developed, and tested by me, with contributions from co-authors as listed below. The draft manuscript was written primarily by me, except where stated otherwise below, and circulated to all co-authors for review.

Hyerin Cho contributed to early development of methodology and software implementing polyphase filterbank inversion, coherent beamforming, derippling, coherent dedispersion, IFFT, and calculation of Stokes parameters. Cherie Day contributed to early development of methodology and software implementing imaging and localisation of bursts. Adam Deller contributed to development of the methodology employed by CELEBI and components of the source code; executed CELEBI and validated output data products; wrote part of section 3.3.2 & all of section 3.3.3; reviewed the manuscript and provided editorial suggestions. Marcin

Glowacki provided project supervision; contributed to development throughout CELEBI; executed CELEBI and validated output data products; reviewed and edited the manuscript. Kelly Gourdji contributed to development throughout CELEBI; executed CELEBI and validated output data products; reviewed and edited the manuscript. Keith Bannister developed the methodology and software related to ASKAP's voltage capture system, including that related to handling raw voltage data and performing polyphase filterbank inversion. Apurba Bera developed methodology and software implementing automatic flagging of RFI-affected data and wrote section 3.4; reviewed and edited the manuscript. Shivani Bhandari developed methodology and software implementing polarisation calibration. Clancy James provided project supervision; developed methodology and software implementing statistical determination of mean source offsets; reviewed and edited the manuscript. Ryan Shannon contributed to development of the high-level methodology of ASKAP voltage capture and burst localisation.

Abstract

Fast radio bursts (FRBs) are being detected with increasing regularity. However, their spontaneous and often once-off nature makes high-precision burst position and frequency-time structure measurements difficult without specialised real-time detection techniques and instrumentation. The Australian Square Kilometre Array Pathfinder (ASKAP) has been enabled by the Commensal Real-time ASKAP Fast Transients Collaboration (CRAFT) to detect FRBs in real-time and save raw antenna voltages containing FRB detections. We present the CRAFT Effortless Localisation and Enhanced Burst Inspection pipeline (CELEBI), an automated offline software pipeline that extends CRAFT's existing software to process ASKAP voltages in order to produce sub-arcsecond precision localisations and polarimetric data at time resolutions as fine as 3 ns of FRB events. We use Nextflow to link together Bash and Python code that performs software correlation, interferometric imaging, and beamforming, making use of common astronomical software packages.

4.1 Introduction

Fast radio bursts (FRBs) are micro- to millisecond duration radio transients (Lorimer et al., 2007; Thornton et al., 2013). Known to be extragalactic, they are extremely energetic (Bhandari et al., 2020b). Although a Galactic magnetar is known to have produced FRB-like emission (CHIME/FRB Collaboration et al., 2020b; Bochenek et al., 2020), no general emission mechanism nor progenitor has been identified, and it is possible that more than one progenitor type contributes to the observed population. Only a small fraction of FRB sources have been observed to repeat (CHIME/FRB Collaboration et al. (2023b) report a repeater fraction tending to $2.6^{+2.9}_{-2.6}\%$) and there are indications of intrinsic differences between repeating and non-repeating FRBs (Pleunis et al., 2021a).

In order to gain greater insight into the nature of FRBs, their emission mechanisms, progenitors, and host environments, and to use them as probes of cosmological parameters (James et al., 2022) and extragalactic matter distributions (Macquart et al., 2020) it is highly desirable and often necessary to identify their host galaxies and measure the polarimetric morphologies of the bursts themselves at high temporal and spectral resolutions. For example, the current sample of host galaxies does not yet point to any preferred progenitor class (Bhandari et al., 2022) but patterns may emerge as the sample grows, and high-time resolution measurements can constrain the size of the emission region and therefore emission mechanisms (Nimmo et al., 2022).

The computational load associated with FRB searches scales with increasing spatial, time, and frequency resolutions, so compromises must be made to make the load manageable. In many cases, these compromises result in an inability to localise most FRB sources with sufficient precision to identify a host galaxy, measure bursts with sufficient temporal or spectral resolutions to make detailed inferences on the emission mechanism, or measure the polarimetric properties of bursts.

Making associations between FRBs and their host galaxies, whilst still restricted

to a small fraction of the detected FRB population, has been accomplished by a number of different radio interferometers. For relatively nearby FRBs, lower localisation precision is needed given the lower sky density of potential host galaxies, and a number of repeating FRBs detected by the Canadian Hydrogen Intensity Mapping Experiment (CHIME) have been associated on the basis of moderate ($\lesssim$arcminute level) localisation precision afforded by detailed beam modelling (Bhardwaj et al., 2021a,b; Michilli et al., 2023; Ibik et al., 2023). Other interferometers operating at higher frequency and with longer baselines have successfully associated non-repeating FRBs to their host galaxies using data products formed in real time. The VLA has localised one apparently non-repeating FRB to a host galaxy (Law et al., 2020) using *realfast*, a real-time imaging FRB search pipeline (Law et al., 2018). MeerKAT has localised two apparently non-repeating FRBs, detected in an incoherent beam of $\sim 1.3\,\mathrm{deg}^2$, to sub-arcsecond precision in images made from standard correlation products and subsequently identified their host galaxies (Caleb et al., 2023b; Driessen et al., 2023), and a method for localising transients detected across multiple MeerKAT tied-array beams is described by Bezuidenhout et al. (2023). The Westerbork Synthesis Radio Telescope's Apertif system is able to detect FRBs in real time and consequently localise, but without the spatial resolution necessary to identify a host galaxy (Connor et al., 2020).

Another method for localising non-repeating FRBs involves a real-time search that triggers the capture of high-resolution data for offline processing that otherwise would not have been saved due to their large volume. The Deep Synoptic Array is able to capture FRBs in voltages and interferometrically localise them to arcsecond precision, allowing identification of host galaxies (Ravi et al., 2019, 2023b,a). While it is yet to localise a non-repeating FRB to a host galaxy, CHIME has a pipeline for real-time FRB detection and capture of baseband data, permitting sub-arcminute FRB localisations and measurement of burst profiles at microsecond time resolution from single detections (Michilli et al., 2021).

The Australian Square Kilometre Array Pathfinder (ASKAP, Hotan et al. 2021) has been enabled by the Commensal Real-time ASKAP Fast Transients Collaboration (CRAFT) to detect FRBs in real-time and save raw antenna voltages of FRB detections. This permits sub-arcsecond-precision localisation of FRBs, including non-repeating FRBs, via interferometric imaging, precise enough to identify a host galaxy and often a position within that galaxy (Bannister et al., 2019b; Prochaska et al., 2019; Macquart et al., 2020; Heintz et al., 2020; Fong et al., 2021; Bhandari et al., 2022; Ryder et al., 2022; Bhandari et al., 2023), and polarimetric measurements at time resolutions as fine as 3 ns (Cho et al., 2020; Day et al., 2020). However, to date, the post-processing of triggered FRB data products has been handled by an ensemble of processing scripts that are manually sequenced and which require significant human quality control. This process is time consuming and potentially error-prone, making it unsuitable for future FRB surveys with ASKAP with higher detection rates (as envisaged for the forthcoming "CRACO" coherent detection system; Bannister et al., in prep.).

This paper describes the CRAFT Effortless Localisation and Enhanced Burst Inspection pipeline (CELEBI), which has been made publicly available on Github[1]. CELEBI is an automated offline software pipeline that extends existing CRAFT post-processing code (Bannister et al., 2019b; Cho et al., 2020) with new functionality and improved monitoring and control to produce sub-arcsecond-precision localisations and high-time resolution data products of FRBs detected with ASKAP with minimal human oversight and direct intervention. §4.2 gives a high-level overview of the pipeline's structure and algorithm. §4.3 describes in detail the processes performed by CELEBI to produce FRB localisations, each subsection corresponding directly to one of CELEBI's processes. §4.4 similarly describes the processes that produce high-time resolution polarimetric data for FRB detections. §4.5 gives a summary and discusses the improvements to CRAFT's voltage processing produced by CELEBI, as well as future improvements to the pipeline. We

[1] github.com/askap-craco/CELEBI/

use FRB190711 (Day et al., 2020) as an example case throughout to demonstrate consistency with previously-published results.

4.2 Overview

4.2.1 Input data format

CELEBI's primary inputs are sets of voltages acquired by the simultaneous freezing and downloading ("dumping") of the contents of a 3.1 s-duration ring buffer for each ASKAP antenna. The buffers record complex-valued electric field samples across a 336-MHz bandwidth in both orthogonal linear polarisations of each beam of an antenna's phased-array feed (PAF), although only the data for the beam in which the desired target is detected in is saved. Upon the real-time detection of an FRB, the voltages are dumped with sufficiently low latency to capture the FRB (Bannister et al., 2019b). Voltages are then obtained for two other sources: a "flux" calibrator (a bright continuum source: typically PKS 0408−65 or PKS 1934−63), and a polarisation calibrator (a bright, highly linearly polarised pulsar: typically Vela or PSR J1644−4559). As described below, these two datasets are employed to derive the necessary calibration terms that enable astrometrically and polarimetrically correct images and time series to be formed for the FRB. The data for the calibrators are typically significantly separated from the FRB, both temporally and spatially. This will produce systematic errors in the images produced from the FRB voltages as the calibration solutions are applied. We account for this using the method described by Day et al. (2021) in process 4.3.7.4. With regards to measuring the polarimetric properties of the polarisation calibrator, ASKAP is sufficiently stable that we do not expect the polarisation calibration solutions derived to be invalid when applied to the FRB data.

ASKAP's polyphase filterbanks (PFBs) produce oversampled "coarse" channels, meaning adjacent channels overlap slightly. Each coarse channel is composed of many "fine" channels, the precise number of which is dependent on the amount of

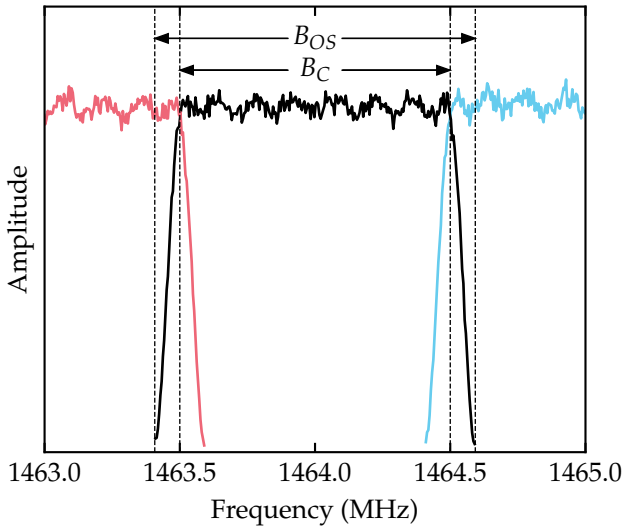

Figure 4.1: Amplitude response as a function of frequency within three adjacent coarse channels pre-PFB inversion, averaged over 4096 fine channels. $B_C = 1\,\text{MHz}$ is the coarse channel bandwidth and $B_{OS} = (32/27)B_C \approx 1.19B_C$ is the oversampled bandwidth. A predictable ripple in the passband amplitude is present due to the response function of the PFB used to form these 1 MHz channels.

data read from file which is dynamically determined during processing. Each PFB produces data across 784 coarse channels, each separated by $B_C = 1\,\text{MHz}$. The oversampled bandwidth of each channel is $B_{OS} = (32/27)B_C \approx 1.19B_C$. Each channel has a region of locally rippled but overall constant frequency response with width B_C, and an oversampled region of width $(B_{OS} - B_C)/2$ on either side that tapers off, as seen in Figure 4.1, which shows the fine spectrum amplitudes in three adjacent coarse channels. Of these 784 coarse channels, 336 are available for real-time analysis by the incoherent sum (ICS) pipeline (Bannister et al., 2019b) and recorded to voltage buffers for offline analysis.

Voltages are stored as 8-bit complex numbers (4 bit real, 4 bit imaginary) in "VCRAFT" files, each of which contains two sets of four 1 MHz oversampled coarse channels. Each set of four channels are internally contiguous in frequency, but the two sets within a VCRAFT file are not necessarily contiguous with each other. Each VCRAFT file was produced by one of six FPGAs on one of seven processing cards for a total of 42 VCRAFT files per polarisation per antenna, and a total

bandwidth of 336 MHz. The headers for these VCRAFT files contain frequency and timestamp information. The observing band is typically one of the "lower" (central frequency 863.5 MHz), "mid" (central frequency 1271.5 MHz), or "upper" (central frequency 1632.5 MHz) bands, with a fixed bandwidth of 336 MHz. We make use of the CRAFT utilities[2] to read and manipulate VCRAFT data.

As well as the raw voltage data, a set of metadata associated with the FRB trigger is also provided as input. This includes the real-time search candidate that triggered the voltage dump, the parameters of the observation the detection was made in, and a preliminary FRB position derived from multibeam analysis with a precision of a few arcminutes.

The candidate that triggered the voltage dump is stored as a text file containing the candidate's signal-to-noise ratio (S/N), arrival time, dispersion measure (DM), and boxcar width. This candidate is the first that passes the S/N, DM, and width filters of the real-time search and as such the parameters are considered preliminary.

The observational parameters provided include the name, location, and fixed delay associated with each ASKAP antenna.

4.2.2 Algorithm overview

CELEBI's primary functionalities are high-precision FRB localisation via interferometric imaging and obtaining high-time resolution data products via tied-array beamforming. It is constructed from Python and Bash scripts linked into a single Nextflow[3] pipeline (Di Tommaso et al., 2017). Nextflow manages data flow between processes, automation of process execution & parallelisation, and submission of processes to supercomputing resources. CELEBI makes use of the Astronomical Image Processing System (AIPS, Greisen 2003), ParselTongue[4], the Common Astronomy Software Applications (CASA, CASA Team et al. 2022),

[2] github.com/askap-craco/craft
[3] nextflow.io
[4] jive.eu/jivewiki/doku.php?id=parseltongue:parseltongue

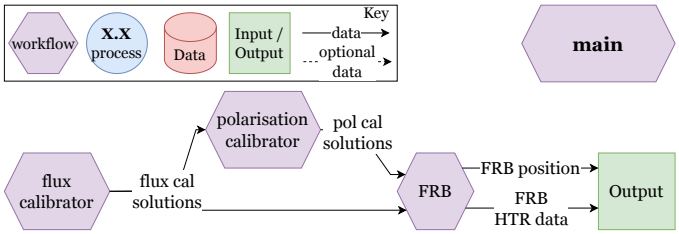

Figure 4.2: Top-level pipeline DFD. Inset: key for DFD symbols.

the CASA Analysis Utilities[5], CRAFT utilities, DiFX (Deller et al., 2011) and psrvlbireduce[6], as well as the Python libraries Numpy (Harris et al., 2020), Scipy (Virtanen et al., 2020), Matplotlib (Hunter, 2007), Astropy (Robitaille et al., 2013; Astropy Collaboration et al., 2018, 2022), and Astroquery (Ginsburg et al., 2019). These dependencies, as well as example execution commands for CELEBI, are listed in the README of CELEBI's github repository.

CELEBI is split into three major workflows, each associated with a set of voltages: `fluxcal`, `polcal`, and `FRB`. These are linked by a `main` workflow, a data-flow diagram (DFD) of which is shown in Figure 4.2.

`fluxcal` (Figure 4.3) produces frequency-dependent complex gain solutions and flux scaling from the "fluxcal" calibrator voltages. These solutions are used in `polcal` and `FRB` for imaging and beamforming. After the application of these solutions, each polarisation of each antenna should be (independently) correctly calibrated, meaning that the different antennas are correctly aligned and the amplitude scale is correctly placed in units of Janskys. However, the two polarisations may still be offset in delay or phase with respect to each other.

`polcal` (Figure 4.4) produces polarisation calibration solutions that correct for the small delay and leakage *between* the two nominally orthogonal polarisation bases of the ASKAP antennas from the polarisation calibrator voltages.

`FRB` (Figure 4.5) takes the solutions from the other major workflows and processes the FRB voltages to determine a sub-arcsecond-precision localisation of the FRB and produce a set of high-time resolution polarimetric data.

[5] casaguides.nrao.edu/index.php/Analysis_Utilities
[6] github.com/dingswin/psrvlbireduce

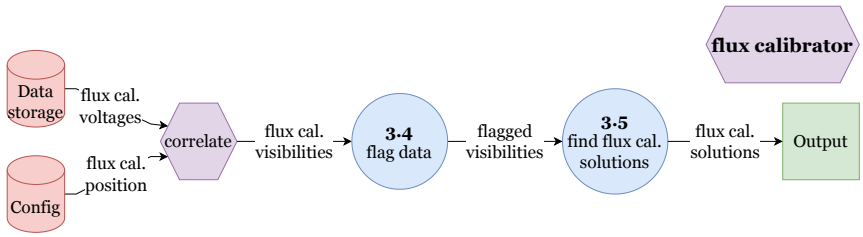

Figure 4.3: `fluxcal` workflow DFD.

4.3 FRB and polarisation calibrator localisation

In each of the major workflows, the voltages are correlated in software using the `correlate` workflow (§4.3.3, Figure 4.7) to produce visibilities, which are then processed in specific ways depending on the purpose of each data set.

`fluxcal` uses its visibilities to derive frequency dependent complex gain solutions (process 4.3.5), which are provided to the other major workflows, where they are used first in imaging, then passed as input to the `beamform` workflow (§4.4.1, Figure 4.11).

`polcal` images its visibilities to localise the calibrator (process 4.3.6) to provide its apparent position to `beamform`, which ultimately produces high-time resolution polarimetric data which is referenced to a model in order to derive polarisation calibration solutions (process 4.4.2). These solutions are then passed on to `FRB`.

`FRB` performs three different modes of correlation: field, gate, and RFI (radio-frequency interference). The field mode is a simple correlation of the full 3.1 s voltage dump, used to image the field around the FRB position (process 4.3.7.3). This is used to derive an astrometric correction for a systematic offset in apparent sky position introduced by the difference in observation time and direction between the FRB detection and later flux calibrator observation (process 4.3.7.4) (Day et al., 2021). The gate mode selects a small, frequency-dependent time window of data for correlation that matches the arrival time of the FRB itself in order to create an image of only the FRB and maximising signal-to-noise. The RFI mode similarly restricts the data used, but instead includes only small (frequency-dependent) time windows immediately before and after the FRB. The RFI visibilities are

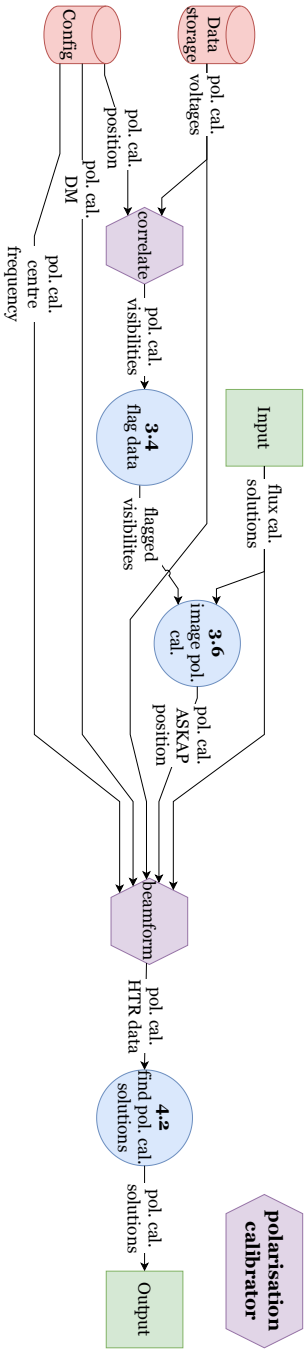

Figure 4.4: `polcal` workflow DFD.

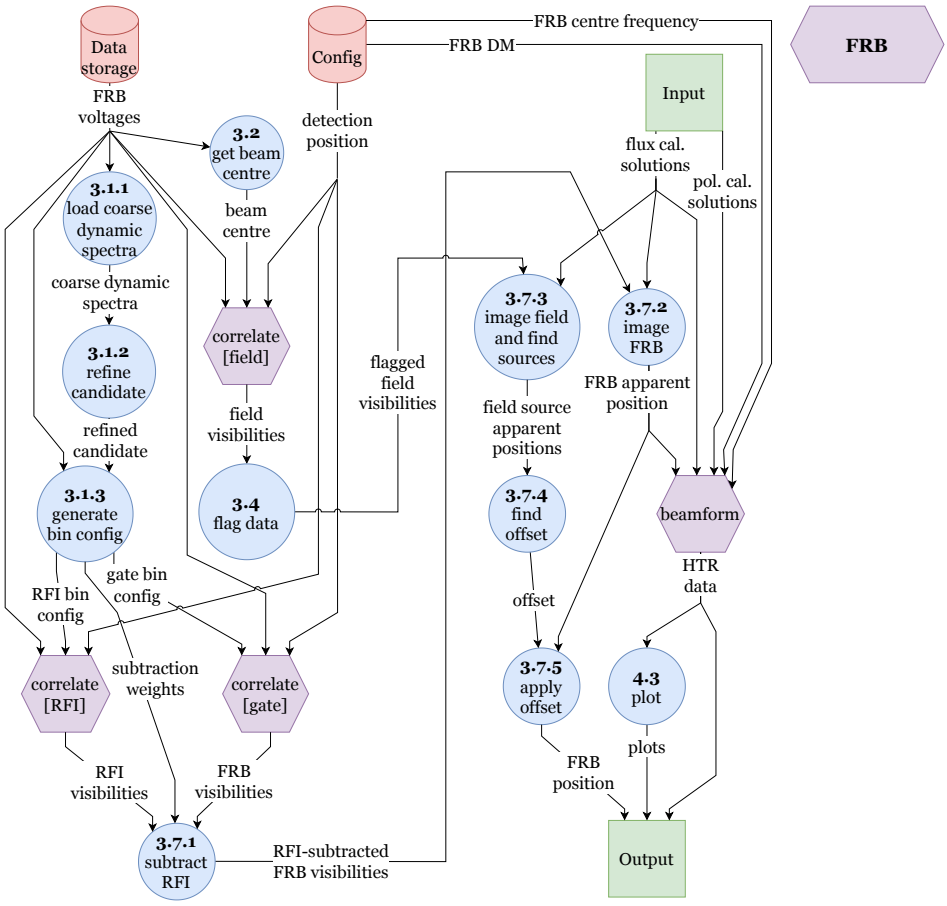

Figure 4.5: FRB workflow DFD.

subtracted from the FRB visibilities in order to eliminate RFI without removing entire channels that may contain important components of the FRB signal (process 4.3.7.1). On these millisecond timescales, RFI contributions to visibilities remain approximately constant, meaning that subtracting an appropriately scaled (in amplitude) copy of the RFI dataset from the FRB dataset can effectively mitigate RFI in frequency ranges that would otherwise be flagged and lost. The FRB is imaged, its position fit (process 4.3.7.2), and the offset derived from the field image applied to calculate the final astrometrically-corrected FRB position (process 4.3.7.5).

4.3.1 Incoherent search

CRAFT's real-time FRB search (Bannister et al., 2019b) tests a grid of DM and arrival time values, meaning that a single FRB event typically produces several candidates with a S/N above the threshold for triggering a voltage dump. Because the dump is triggered on the first candidate seen above threshold, the measured DM and arrival time of this candidate is likely not to be the combination that produces the highest S/N. In order to optimise S/N when imaging the FRB, we first refine the FRB candidate to measure a more accurate DM and arrival time by performing an incoherent search on the voltages following the same principles as CRAFT's real-time detection system.

4.3.1.1 Load coarse dynamic spectra

This process loads the voltages from the FRB data set and constructs a "coarse" dynamic spectrum. The frequency resolution is chosen to be 1 MHz for simplicity of implementation (the data is already channelised to 1 MHz), and the time resolution is chosen to be 1 ms as this is fine enough to allow sufficient precision in refining the FRB candidate, while keeping the processing time of candidate refinement low.

To construct a coarse dynamic spectrum, we load the coarse-channelised

voltages and for each coarse channel:

1. Fast Fourier Transform (FFT) into the spectral domain.
2. Trim the oversampled regions (Figure 4.1).
3. Inverse FFT to obtain a 1 µs time resolution complex voltage time series.
4. Take the square of the absolute power of this time series to obtain a power time series.
5. Reduce the time resolution ("time scrunch") to 1 ms by summing blocks of 1000 time samples.

The time scrunched power time series in each coarse channel is then arranged into a two-dimensional dynamic spectrum, which is passed as output of the process.

We account for geometric delays in signal arrival time between antennas by applying offsets in time in the data as it is read from the VCRAFT files based on an interferometer model calculated using the DiFX program `difxcalc` (Gordon et al., 2016) for the initial rough FRB position.

An instance of this process is run for each unique polarisation-antenna pair.

This process also calculates and outputs the time axis of the dynamic spectra in units of Modified Julian Day (MJD) based on the start time of the data in the VCRAFT headers and the geometric delays.

4.3.1.2 Refine candidate

This process sums the power dynamic spectra across both polarisations and all antennas as output by 4.3.1.1, then searches the resulting ICS dynamic spectrum for a single dispersed pulse. We search over DMs in a configurable range of DM values, defaulting to $\pm 10\,\mathrm{pc\,cm^{-3}}$ around the detection candidate's DM with a step size of $0.01\,\mathrm{pc\,cm^{-3}}$. For each DM, we incoherently dedisperse the ICS dynamic spectrum by shifting each coarse channel by an integer number of time samples.

The number of 1 ms samples a coarse channel of central frequency f is shifted in the direction of increasing time is given by

$$t_{\text{shift}}(\text{DM}, f) = \left\lfloor k_{\text{DM}} \text{DM} \left(f_0^{-2} - f^{-2} \right) \cdot 1000 \right\rfloor , \tag{4.1}$$

where $k_{\text{DM}} = (2.41 \times 10^{-4})^{-1}\,\text{MHz}\,\text{cm}^3\,\text{pc}^{-1}$, f_0 is a reference frequency, which we choose as the central frequency of the lowest-frequency coarse channel, and the factor of 1000 converts from seconds to milliseconds. Note that this choice of reference frequency results in the lowest-frequency coarse channel not being shifted at all, and as such we can use the MJD time array produced by process 4.3.1.1 to measure the arrival time of the burst at the bottom of the observing band. We then sum this dedispersed dynamic spectrum along the frequency axis to get a 1 ms-resolution dedispersed profile.

To improve the S/N of the FRB in the event that it is spread out over multiple time samples, either due to the burst's intrinsic width or dispersive smearing within channels, we smooth the profile by convolving with top-hat functions with widths between 1 and 10 samples. We then calculate the S/N of each sample in each smoothed profile by dividing each profile by its standard deviation. We take the DM, time, and width corresponding to the maximum S/N value (DM_{opt}, t_{opt}, and w_{opt} respectively) and create a refined candidate file with these values updated.

4.3.1.3 Generate bin configs

The gate and RFI correlation modes performed in `FRB` require the specification of time and frequency dependent weights that are used to select only certain windows of data for correlation and imaging. The windows are shaped according to the expected time delay due to dispersion across the band based on the arrival time and DM of the refined candidate generated by process 4.3.1.2. These take the form of "bin config" files, that record the windows and their weights, and a "polyco" file that records a reference time & frequency and the DM of the FRB.

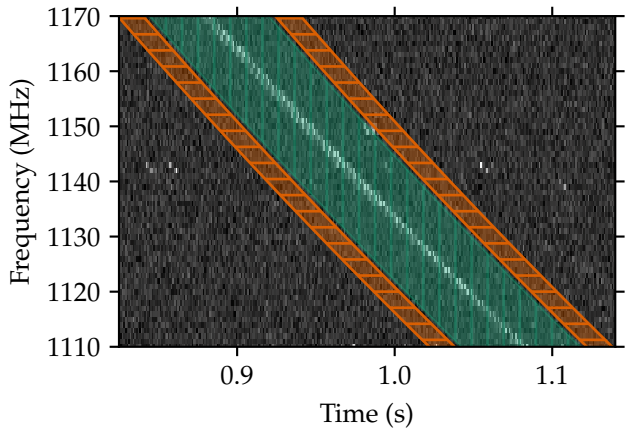

Figure 4.6: Cropped FRB190711 dynamic spectrum (time scrunched to 1 ms) with example gate bin region (green) and RFI bins (orange hatched) overlaid. The green region is split into seven equal-width bins.

Figure 4.6 illustrates how the bins are defined for the gate and RFI modes. The gate bins are defined by taking a region of width $w_{\mathrm{opt}} + 70\,\mathrm{ms}$, with a dispersive sweep corresponding to $\mathrm{DM}_{\mathrm{opt}}$, and centred on t_{opt} at the bottom of the band. This region is divided into seven bins. The central bin is expected to be the only bin to contain the FRB, but all are imaged in case part or all of the FRB signal falls outside of the central bin due to small unexpected errors in identifying the burst arrival time.

The RFI bins are each 16 ms wide and follow the same dispersive sweep as the gate region, leaving a 4 ms buffer on either side of the gate region. This width was chosen as a compromise between the counter-posed goals of minimising the noise contribution (which favours a longer duration) and measuring the RFI environment as close in time as possible to the FRB itself (which favours a shorter duration).

4.3.2 Get beam centre

We wish to centre the field image on the beam centre, rather than the preliminary FRB position. This process parses the FRB voltage headers in order to obtain

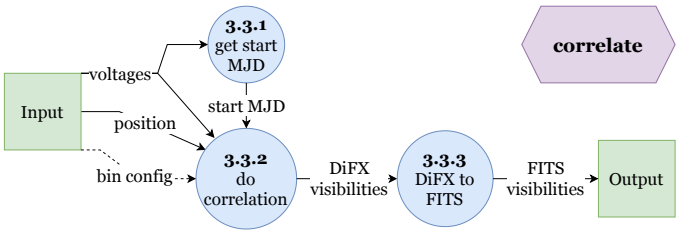

Figure 4.7: Correlation workflow DFD.

the sky coordinates of the beam centre, which are passed to the field mode's `correlate` instance.

4.3.3 Correlate

The `correlate` workflow takes as input a VCRAFT voltage dataset (as described in §4.2.1) and an optional bin configuration (as generated by process 4.3.1.3), and outputs correlated visibilities in the Flexible Image Transport System (FITS) format. Figure 4.7 shows the DFD for the workflow.

4.3.3.1 Get start MJD

Because the voltage dump does not happen perfectly simultaneously across all the antennas, the data will have slightly different start times on a per-antenna basis. This process parses the voltage headers to find the earliest start time so that it can be provided to process 4.3.3.2 to be used as a reference time. This ensures that all the correlations are using the same reference time.

This process is executed a single time, and its output passed to each instance of process 4.3.3.2.

4.3.3.2 Do correlation

This process uses the "DiFX" software correlator (Deller et al., 2011) to produce visibility datasets from the saved voltage data. One DiFX instance is executed for each of the 42 card-FPGA pairs, taking in two voltage files per antenna (one for each polarisation). This produces 8 × 1.185 MHz output subbands (which are

spaced by 1 MHz, but are wider than 1 MHz due to the ASKAP over-sampling), each with 128 frequency channels. The instance for the lowest-frequency card-FPGA pair is executed first, and its output passed to the other 41 instances (which are executed in parallel) to avoid issues caused by the FRB dispersion, as described below.

Because the 1 MHz-wide ASKAP coarse channels are over-sampled by a factor of 32/27, there is redundant data that can be discarded after correlation, and it is convenient to do so prior to the assembly of the DiFX output into FITS files. We achieve this with a python script *mergeOverSampledDiFX.py*; from each 1 MHZ coarse channel, it retains 108 of the 128 frequency channels, corresponding to the non-overlapped portion of the band, and assembles the retained channels into a contiguous block. Since each card-FPGA pair provides two blocks of four adjacent ASKAP coarse channels, the result is two 4 MHz subbands, no longer oversampled, each with 432 frequency channels.

If a bin configuration file, as generated by process 4.3.1.3, is provided for the FRB, one or more datasets of visibilities from only a subset of the available frequency-time range are produced, according to the definition in the bin config — either a single RFI dataset or seven gate bin datasets (from the orange regions or within the green region depicted in Figure 4.6 respectively). Due to the short length of the voltage files, the correction of the dispersive delays can lead to a frequency-dependent population of the output bin datasets — at higher frequencies, the time correction can exceed the difference between the voltage file start and the FRB time at the low end of the band. In this case, some bins may not have any visibility data for some frequencies, which leads to issues when subsequently assembling FITS files. To counter this, dummy data is generated for any baselines, times, and frequencies for which no visibilities were produced. This dummy data has zero weight, and therefore does not impact the outputs down the processing chain. The lowest frequency card-FPGA pair, which is guaranteed to have data due to having the latest FRB arrival time, is used as a template to provide the

dummy data.

4.3.3.3 Convert DiFX to FITS

This process collects the output of all instances of process 4.3.3.2 to combine visibilities and convert the data into the FITS format. This produces a single FITS visibility file containing the full 336 MHz bandwidth, assembled into a single subband. During this process, frequency averaging is undertaken to reduce the data volume by a factor of 27, leading to a final spectral resolution of 250 kHz.

4.3.4 Flag RFI-affected data

Parts of the visibility data are often found to be corrupted by RFI or other systematic effects. Identification and flagging of corrupted visibilities are essential for calibration and imaging. This process performs data-flagging in three steps as described below and is run post-correlation in the `fluxcal` and `polcal` workflows, and in the `FRB` workflow on the field mode correlated data.

1. Frequency channels that are known to be always affected by persistent RFI (from satellites) are flagged for all baselines.

2. Data from each baseline are independently inspected for RFI affected channels. Identification of corrupted channels is performed based on the average (median) power and noise (median-absolute-deviation) in each channel. A frequency channel is identified as corrupted if its average power (or noise) is an outlier of the distribution for all channels. The outlier threshold is calculated based on the number of data points and assuming Gaussian statistics. A nominal threshold is set at the value beyond which the number of expected data points drops below 1 for the given number of total data points and Gaussian statistics of the data. A multiplicative tolerance factor is applied to this nominal threshold to keep the flagging process conservative, especially in the initial rounds of flagging. Since presence of RFI in a

significant number of channels may bias the statistics, flagging is performed with a high tolerance factor in the first round. This step is repeated several times, lowering the tolerance factor in each subsequent round. The tolerance factor used in the final rounds of flagging is close to unity.

3. The statistics (average power and noise) of all baselines are compared together. Baselines having average power or noise which are outliers of the distribution for all baselines are identified as RFI-affected baselines, and flagged. An antenna is completely flagged if all its baselines are identified as RFI-affected baselines. The outlier threshold for flagging is set in a similar manner as described in the previous point.

This process is independently executed on visibilities corresponding to the flux calibrator, the polarization calibrator and the field correlation. A flag file containing affected antennas, frequency channels, and/or baselines to be excised (on the basis of the above steps) is also generated for diagnostic purposes. Each of the calibration and imaging processes may also be provided an optional user-defined flag file if more flagging than is done automatically is required.

4.3.5 Find flux calibration solutions

After flagging, we derive frequency-dependent complex gain solutions from the flux calibrator visibilities using three AIPS tasks: FRING (solves for delay, i.e., a phase slope linearly proportional to frequency, with the solution amplitude fixed at unity), CPASS (solves for frequency-dependent complex gain as a polynomial with frequency, normalising the average amplitude solution for each antenna to unity), and CALIB (solves for a single frequency-independent complex gain per antenna, effectively setting the flux density scale and correcting for antenna-to-antenna signal level variations). While it would in principle be possible to combine these three solutions into a single stage, this separation allows for an easier identification of outliers based on delay and/or average amplitude correction.

We also apply these solutions to the flux calibrator visibilities themselves and convert to a CASA measurement set for diagnostic purposes. The solutions are finally passed to the `polcal` and `FRB` workflows for imaging.

4.3.6 Image polarisation calibrator

After flagging, we apply the delay and bandpass calibration tables as derived by process 4.3.5 to the polarisation calibrator visibilities using AIPS. We then convert the calibrated visibilities to a CASA measurement set and create an image of a 128" square region centred on the expected position of the polarisation calibrator with a 1" resolution using the CASA routine TCLEAN. ASKAP's maximum angular resolution (with its longest baseline and at its highest frequency) is 6" (Hotan et al., 2021), so our choice of 1" pixels is always sufficient. We search the image for a single point source and fit its apparent position with the AIPS task JMFIT, which is passed as an output to the `beamform` workflow.

4.3.7 FRB localisation

4.3.7.1 Subtract RFI

Because FRB emission is often restricted to only a portion of the observing bandwidth and a significant amount of the signal is often in channels that are contaminated with RFI, we cannot simply flag channels as for the other visibility sets without losing significant signal-to-noise at best, or removing the FRB signal entirely at worst. Instead, we subtract the visibilities correlated in the RFI mode from those correlated in the gate mode, without any time interpolation and under the assumption that any RFI present is constant over the $\sim$50 ms surrounding the FRB. This process performs this subtraction, weighting the RFI visibilities by the ratio of the gate duration to the total duration of the RFI bins.

We find that the noise post-RFI subtraction is consistent with white noise, and this method sufficiently removes RFI to make good images and localisations

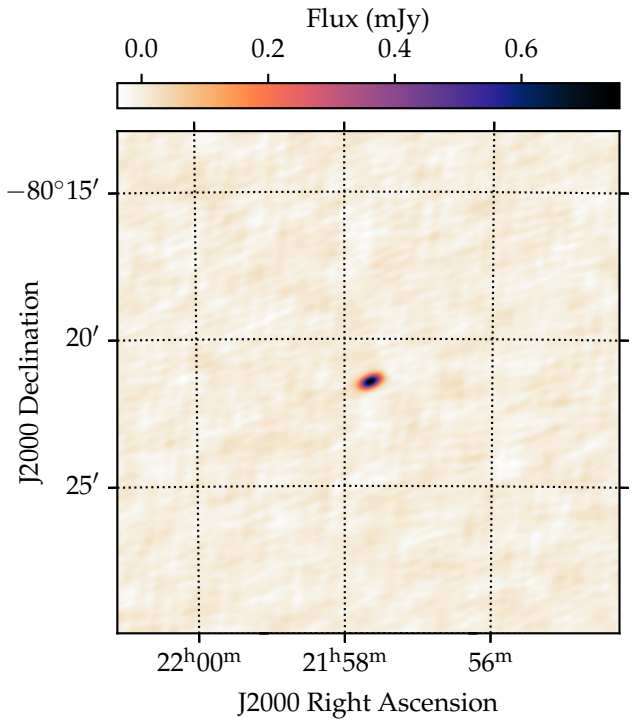

Figure 4.8: Image of FRB190711 created in process 4.3.7.2.

in most cases, but is occasionally imperfect. We treat imperfections by manually flagging data after RFI subtraction where necessary, and this is an area of ongoing improvement for CELEBI.

4.3.7.2 Image FRB

Using the RFI-subtracted visibilities from the FRB gate correlation, we calibrate, image, and fit the apparent position of the FRB in the same way as the polarisation calibrator (process 4.3.6), but creating a 1024" square image due to the larger initial positional uncertainty. As an example, an image of FRB190711 is shown in Figure 4.8. The FRB's measured position (right ascension $\mathrm{RA_{FRB}}$, declination $\mathrm{Dec_{FRB}}$) is passed both directly to `beamform` and with its error (right ascension $\Delta\mathrm{RA_{FRB}}$, declination $\Delta\mathrm{Dec_{FRB}}$) to process 4.3.7.5.

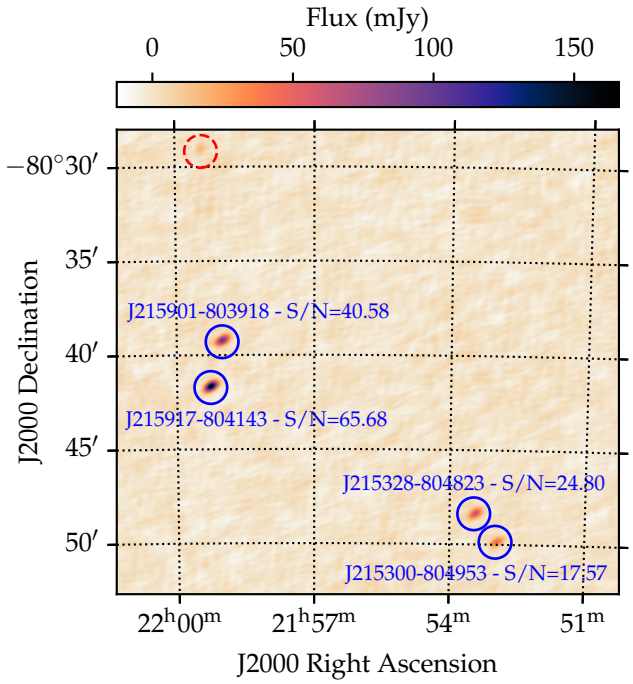

Figure 4.9: Cropped field image for FRB190711 created in process 4.3.7.3. Blue circles indicate sources identified in the field image that returned one source in the RACS catalog, labeled with RACS component ID and detection S/N. The red dashed circle indicates an identified point source that did not pass the S/N threshold of 7 to be included in the offset analysis.

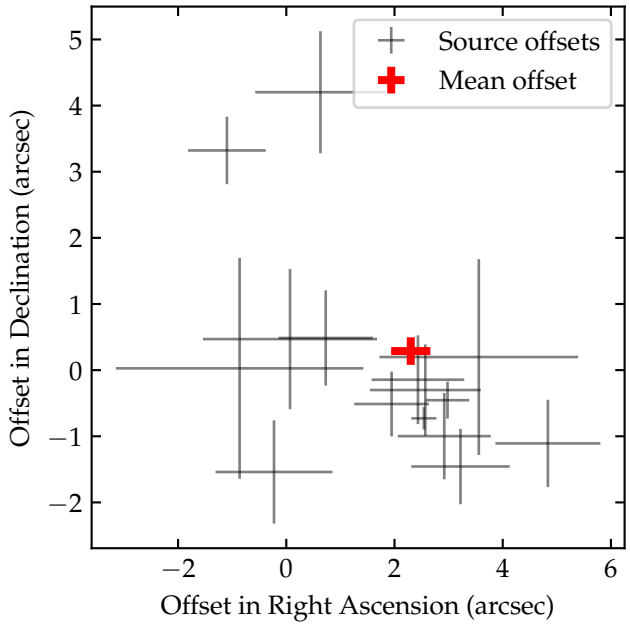

Figure 4.10: Offsets between measured field source positions and RACS catalog positions (thin grey) and mean offset as calculated by process 4.3.7.4 (thick red) for FRB190711.

4.3.7.3 Image field and find sources

The field visibilities are calibrated, and imaged as for the polarisation calibrator and FRB, creating a 3000" square image. We identify up to 50 point sources in this image through the CASA task FINDSOURCES and fit their apparent positions with JMFIT. These positions are then passed to process 4.3.7.4. A cropped section of the field image created for FRB190711 with identified point sources marked is shown in Figure 4.9.

4.3.7.4 Find offset

For each of the point sources identified in the field image, we filter out those with measured S/N less than 7 and search the Rapid ASKAP Continuum Survey (RACS) catalog (Hale et al., 2021) with Astroquery for point sources within a 5" radius of the apparent position. If more than one item is found in the catalog (which occurs with ∼1.4% of our field sources), or if no items are found (which

occurs with ∼22% of our field sources) we discard the source. Identified sources discarded due to having no corresponding items returned from RACS are typically a result of FINDSOURCES incorrectly identifying a noise fluctuation as a source. In a small number of cases, sources in our image that appear to be real will not return any items from RACS, likely due to differences in observing frequency between the RACS catalog (which is in the low band) and our observation.

For each source in the remaining ensemble, we calculate the offset between our measured position and the RACS catalogue position, and then estimate a systematic positional correction (right ascension $\overline{\mathrm{RA}}_{\mathrm{offset}}$, declination $\overline{\mathrm{Dec}}_{\mathrm{offset}}$) and error (right ascension $\Delta\overline{\mathrm{RA}}_{\mathrm{offset}}$, declination $\Delta\overline{\mathrm{Dec}}_{\mathrm{offset}}$) for the field (and the FRB itself) using a weighted mean of these offsets multiplied by an empirical scaling factor (which accounts for differences in the angular resolution and frequency of our observations compared to the reference catalogue); the process is described in detail by Day et al. (2021).

Figure 4.10 shows the offsets between CELEBI-measured positions and RACS catalog positions for the sources identified in the FRB190711 field image, as well as the calculated mean offset.

4.3.7.5 Apply offset

Finally, the mean offset and its error are added to the FRB's ASKAP position to obtain the corrected position (right ascension $\mathrm{RA}_{\mathrm{corrected}}$, declination $\mathrm{Dec}_{\mathrm{corrected}}$) and error:

$$\mathrm{RA}_{\mathrm{corrected}} = \mathrm{RA}_{\mathrm{FRB}} + \frac{\overline{\mathrm{RA}}_{\mathrm{offset}}}{\cos\left(\mathrm{Dec}_{\mathrm{FRB}}\right)} \pm \sqrt{\Delta\mathrm{RA}_{\mathrm{FRB}}^2 + \Delta\overline{\mathrm{RA}}_{\mathrm{offset}}^2}, \tag{4.2}$$

$$\mathrm{Dec}_{\mathrm{corrected}} = \mathrm{Dec}_{\mathrm{FRB}} + \overline{\mathrm{Dec}}_{\mathrm{offset}} \pm \sqrt{\Delta\mathrm{Dec}_{\mathrm{FRB}}^2 + \Delta\overline{\mathrm{Dec}}_{\mathrm{offset}}^2}. \tag{4.3}$$

Table 4.1 lists the measured position, offset, and corrected position as calculated by CELEBI for FRB190711. We note agreement of the corrected position here with the position given by Day et al. (2020).

Table 4.1: Position-related quantities for FRB190711 as calculated by CELEBI.

Quantity	CELEBI-calculated value
$\mathrm{RA_{FRB}}$ (J2000, hh:mm:ss.s)	21:57:40.1 ±0.2
$\mathrm{Dec_{FRB}}$ (J2000, dd:mm:ss.s)	-80:21:29.1 ±0.1
$\overline{\mathrm{RA}}_{\mathrm{offset}}$ (arcsec.)	2.3 ± 0.3
$\overline{\mathrm{Dec}}_{\mathrm{offset}}$ (arcsec.)	-0.4 ± 0.2
$\mathrm{RA_{corrected}}$ (J2000, hh:mm:ss.s)	21:57:41.0 ±0.4
$\mathrm{Dec_{corrected}}$ (J2000, dd:mm:ss.s)	-80:21:29.4 ±0.3

4.4 Obtaining high-time resolution data via beamforming

VCRAFT voltages can be used to reconstruct complex-valued time series of the electric field in the X and Y polarisations at the bandwidth-limited sample rate of $(336\,\mathrm{MHz})^{-1} \approx 3\,\mathrm{ns}$, coherently summed across antennas and coherently dedispersed to eliminate dispersion and associated smearing. This allows for construction of the Stokes parameters I, Q, U, V and measurements of the polarisation properties at high-time resolution and high S/N of FRBs detected and localised by ASKAP. Because we have access to the electric fields in X and Y directly, we can also construct arbitrarily-shaped dynamic spectra in I, Q, U, and V with freely-chosen time and frequency resolutions Δt and Δf, constrained only by $\Delta t \Delta f \geq 1$. These dynamic spectra allow for polarimetric measurements across frequency and time, including the rotation measure (RM) and polarisation fractions.

In order to obtain these data products, the following operations must be performed on the voltages:

1. Beamforming: the application of per-antenna time delays to account for the difference in signal arrival times due to the geometry of antennas and hardware signal propagation delays (process 4.4.1.2)

2. PFB inversion: undoing the coarse channelisation performed by hardware before the voltages are recorded to obtain a single complex fine spectrum

per polarisation per antenna (process 4.4.1.2)

3. Calibration: the application of per-antenna bandpass calibration solutions, obtained during burst localisation, to the fine spectra (process 4.4.1.2)

4. Summation: coherent summation of fine spectra across antennas to obtain a single fine spectrum per polarisation (process 4.4.1.3)

5. Derippling: removing systematic rippling in the fine spectra (processes 4.4.1.4 and 4.4.1.5)

6. Coherent dedispersion (process 4.4.1.6)

7. Inverse Fourier transform: obtain complex-valued time series at $(336\,\mathrm{MHz})^{-1} \approx 3\,\mathrm{ns}$, in the X and Y linear polarisation bases, via inverse Fourier transform of the fine spectra (process 4.4.1.7)

8. Construct Stokes parameters and dynamic spectra (process 4.4.1.8)

4.4.1 Beamform

The `beamform` workflow (Figure 4.11) takes in a set of voltages, localised source position, flux calibration solutions, and optionally polarisation calibration solutions, and performs the operations listed above to produce a HTR data set, which includes: complex $\sim$3 ns-resolution time series in X and Y; Stokes I, Q, U, and V time series at the same time resolution; and arbitrarily-shaped I, Q, U, and V dynamic spectra (typically with $\Delta t = 1\,\mu\mathrm{s}$ and $\Delta f = 1\,\mathrm{MHz}$).

The `beamform` workflow is invoked within the `polcal` and `FRB` workflows, in both cases after the respective source has been localised. The position provided to the `FRB` instance of `beamform` is the apparent position, i.e. the position that is fit from the FRB image without astrometric correction.

The method for PFB inversion has also been described by Morrison et al. (2020), and the full method for obtaining high-time resolution FRB data by Cho

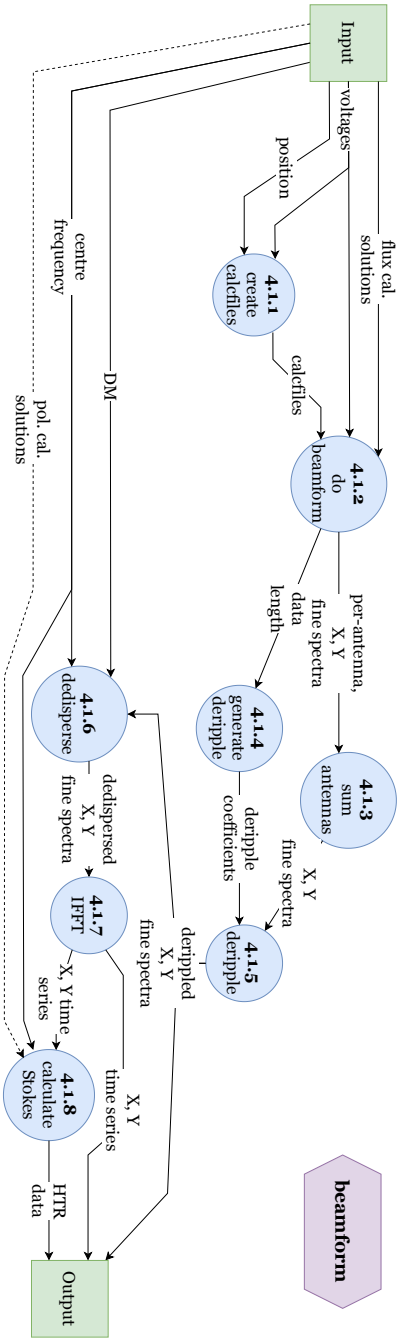

Figure 4.11: Beamform workflow DFD.

et al. (2020). We describe these methods again here to reflect changes to the methods and describe the specific implementations applied in CELEBI.

4.4.1.1 Create calcfiles

This process uses `difxcalc` to calculate the antenna-dependent geometric delays used in used by process 4.4.1.2 to align each antenna's datastream in time, given the previously-determined FRB position.

4.4.1.2 Do beamform

This process prepares a fine spectrum (a spectrum of fine channels across the entire observing bandwidth) from voltages in each antenna for beamforming. This involves the application of antenna-dependent time delays, PFB inversion, and application of flux calibration solutions. An instance of this process is run for each unique polarisation-antenna pair, which we index with $p \in \{\mathrm{X}, \mathrm{Y}\}$ and $a \in [1 \,..\, n_{\mathrm{ant}}]$ respectively, where n_{ant} is the number of antennas available.

The initial duration of the data across all antennas is equal, but because we are applying offsets to each antenna's data we must slightly reduce the duration of data loaded so that the data for all antennas occupies the same time range after applying the delays. We choose a number of samples n_{samp} that maximises the duration loaded while satisfying this condition.

In order to coherently sum signals across antennas, we must apply antenna-dependent time delays Δt_a to the data. These have two components: a time-dependent geometric delay $G_a(t)$ that accounts for the differing path lengths of a signal between antennas; and a fixed delay F_a, which is measured during normal ASKAP operations and accounts for delays in hardware (mostly due to signal propagation delay in cables of different lengths for each antenna). F_a is measured every few days and is only expected to change when ASKAP's digitisers are reset, so we assume it to be stable between these resets. These delays are provided by process 4.4.1.1.

The geometric delay changes with time to account for the Earth's rotation changing the difference in arrival times over the duration of the 3.1-second voltage dump. `difxcalc` fits a polynomial to model the required geometric delay in each antenna as a function of time. Due to the short ($\sim$seconds) duration of data included in processing FRB voltages, the delay applied is well-approximated as being linear in time. $G_a(t)$ is evaluated via the interferometer model's polynomial at t_{start} and t_{end}, corresponding to the start and end times of the data, and is linearly interpolated to give $G_a(t) \propto t$.

The coarse channelised voltages are loaded from all available VCRAFT files to obtain a complex time series for each coarse channel index $c \in [1 \,..\, n_{\text{chan}}]$ where in general the number of channels $n_{\text{chan}} = 336$. When reading the data from disk, we load n_{samp} samples, offset from the beginning of the data by a number of samples equivalent to F_a. We then Fourier transform the complex time series to obtain a fine spectrum $s_{p;a;c}(f)$. Each of these spectra are of oversampled coarse channels with central frequency f_c. The geometric delay $G_a(t)$ is applied to $s_{p;a;c}(f)$ to give an aligned spectrum:

$$s^{\text{align}}_{p;a;c}(f) = s_{p;a;c}(f) e^{2i\pi f_c G_a(t)}. \tag{4.4}$$

By truncating each channel to remove the tapered regions and concatenating the flat regions of the fine spectra of the channels, we obtain a fine spectrum across the full bandwidth with a constant frequency response. First the truncation:

$$s^{\text{trunc}}_{p;a;c}(f) = \begin{cases} 0, & f < f_c - \frac{B_C}{2} \\ s^{\text{align}}_{p;a:c}(f), & f_c - \frac{B_C}{2} \leq f < f_c + \frac{B_C}{2} \\ 0, & f_c + \frac{B_C}{2} \leq f \end{cases}, \tag{4.5}$$

and then the concatenation:

$$S_{p;a}(f) = \sum_{c=1}^{n_{\text{chan}}} s^{\text{trunc}}_{p;a;c}(f). \tag{4.6}$$

Then we apply the flux calibration:

$$S^{\text{cal}}_{p;a}(f) = P_{\text{flux};a}(f) S_{p;a}(f), \tag{4.7}$$

where $P_{\text{flux};a}(f)$ is an antenna-dependent phasor applying the flux calibration solutions as derived by process 4.3.5.

4.4.1.3 Sum antennas

This process takes in the calibrated, beamformed fine spectra for each polarisation in each antenna output by process 4.4.1.2 and coherently sums these spectra to produce a single spectrum per polarisation:

$$S_p(f) = \sum_{a=1}^{n_{\text{ant}}} S^{\text{cal}}_{p;a}(f). \tag{4.8}$$

4.4.1.4 Generate deripple coefficients

The design of ASKAP's PFB leads to the recovered fine spectra having a non-uniform, rippled frequency response (see Figure 4.1). However, the exact shape of this rippling is predictable and it can be mitigated by dividing by a set of deripple coefficients. The deripple coefficients are the inverse of the coarse channel bandpass. This is determined by the FFT of the 24,576 ASKAP PFB coefficients $C_{\text{PFB}}(\delta f)$, where δf is frequency relative to the centre of the coarse channel, themselves a sinc function which is smoothed at the edges to reduce artefacts from the finite size of the filter. Fluctuations in the response are within 0.2 dB over the nominal 1 MHz coarse channel bandwidth (Tuthill et al., 2015). These coefficients are constant within the ASKAP system, and identical for each coarse channel and antenna. They have been generated once, and are hard-coded within CELEBI.

The derippling coefficients for each channel are

$$C_{\text{derip}}(\delta f) = \frac{1}{|\mathcal{F}(C_{\text{PFB}}(\delta f))|}. \tag{4.9}$$

Because the exact number of samples in the fine spectra (n_{samp}) differs between input datasets, we linearly interpolate the denominator of this fraction to match the number of samples in each channel's truncated fine spectrum, i.e. $\lfloor n_{\text{samp}}(B_C/B_{OS}) \rfloor$.

4.4.1.5 Apply deripple coefficients

Because the deripple coefficients $C_{\text{derip}}(\delta f)$ are identical for each coarse channel, we apply them by iterating over the central frequencies f_c of each of the n_{chan} coarse channels:

$$S_p^{\text{derip}}(f_c + \delta f) = S_p(f_c + \delta f) C_{\text{derip}}(\delta f). \tag{4.10}$$

This produces fine spectra $S_p^{\text{derip}}(f)$ with uniform frequency responses.

4.4.1.6 Coherently dedisperse

Dispersion is a well-modelled process, and one that is straightforward to account for in FRB data. Having access to the complex spectra of the X and Y polarisations enables coherent dedispersion, instead of imperfect incoherent dedispersion.

Coherent dedispersion is able to perfectly compensate for and remove the frequency-dependent time delay introduced by the ionised interstellar medium (assuming cold plasma dispersion) by acting on the voltage data that samples the electromagnetic wave in each of the two linear polarisations. This is because dispersion, as a physical process, effectively acts as a frequency-dependent rotation of phase in the spectral domain that manifests as a frequency-dependent time delay in the temporal domain. Therefore, with access to the spectral domain of the radiation being dispersed (the FRB signal), the phases can be de-rotated to obtain the signal as it would have been without any dispersion.

Assuming cold plasma dispersion, the transfer function for coherent dedispersion to a dispersion measure DM is:

$$H(f;\,\mathrm{DM}) = \exp\left(2i\pi k_{\mathrm{DM}}\mathrm{DM}\frac{(f-f_0)^2}{f f_0^2}\right), \tag{4.11}$$

(Hankins, 1971) where f_0 is a reference frequency, which we choose as the minimum frequency of the observing bandwidth. We apply this transfer function to the spectrum of each polarisation to coherently dedisperse them:

$$S_{p;\mathrm{DM}}(f) = H(f;\,\mathrm{DM})S_p^{\mathrm{derip}}(f). \tag{4.12}$$

4.4.1.7 Inverse fast Fourier transform

This process applies the inverse fast Fourier transform to the dedispersed fine spectra to obtain the complex electric field in each polarisation in the time domain:

$$E_p(t) = \mathcal{F}^{-1}\left(S_{p;\mathrm{DM}}(f)\right). \tag{4.13}$$

4.4.1.8 Calculate Stokes parameters

We now calculate time series for the Stokes parameters:

$$I(t) = |E_X(t)|^2 + |E_Y(t)|^2, \tag{4.14}$$

$$Q(t) = |E_X(t)|^2 - |E_Y(t)|^2, \tag{4.15}$$

$$U(t) = 2\,\mathrm{Re}(E_X^*(t)E_Y(t)), \tag{4.16}$$

$$V(t) = 2\,\mathrm{Im}(E_X^*(t)E_Y(t)). \tag{4.17}$$

The electric field time series can also be used to generate dynamic spectra with frequency resolution Δf and time resolution Δt such that $\Delta f \Delta t = 1$. Typically, this is done with $\Delta\nu = 1\,\mathrm{MHz} \implies \Delta t = 1\,\mu\mathrm{s}$, but is in general only constrained by $\Delta t = N_{\mathrm{chan}}\delta t$, where N_{chan} is a positive integer representing the number of channels desired in the dynamic spectra and $\delta t = (336\,\mathrm{MHz})^{-1} \approx 3\,\mathrm{ns}$ is the bandwidth-limited time resolution.

Once Δf and Δt are selected, the dynamic spectra in each polarisation are

generated by taking the discrete Fourier transform of N_{chan} samples at a time. This process is demonstrated visually in Figure 4.12, and gives the dynamic spectra $E_X(t, f)$ and $E_Y(t, f)$. The Stokes dynamic spectra are then calculated as before:

$$I(t, f) = |E_X(t, f)|^2 + |E_Y(t, f)|^2, \tag{4.18}$$

$$Q(t, f) = |E_X(t, f)|^2 - |E_Y(t, f)|^2, \tag{4.19}$$

$$U(t, f) = 2\,\mathrm{Re}(E_X^*(t, f)E_Y(t, f)), \tag{4.20}$$

$$V(t, f) = 2\,\mathrm{Im}(E_X^*(t, f)E_Y(t, f)). \tag{4.21}$$

We mitigate time-constant, frequency-dependent RFI in the dynamic spectra by zero-meaning and normalising each channel. For each channel in each Stokes dynamic spectrum, we zero-mean by subtracting the average value in that channel, and normalise by dividing by the standard deviation of the corresponding Stokes I channel to ensure constant scaling between the Stokes parameters.

If polarisation calibration solutions as determined by process 4.4.2 have been provided, we also apply these to the Stokes U and V dynamic spectra:

$$U'(t, f) = U(t, f)\cos(\Phi(f)) - V(t, f)\sin(\Phi(f)), \tag{4.22}$$

$$V'(t, f) = U(t, f)\sin(\Phi(f)) + V(t, f)\cos(\Phi(f)). \tag{4.23}$$

4.4.2 Derive polarisation calibration solutions

In order to correct for instrumental frequency-dependent leakage between Stokes U and V, we take the Stokes dynamic spectra produced by process 4.4.1.8 for the polarisation calibrator data and derive a correction angle $\Phi(f)$ to apply to the FRB data using the method described by Prochaska et al. (2019):

$$\Phi(f) = \Delta\tau f + \Phi_0, \tag{4.24}$$

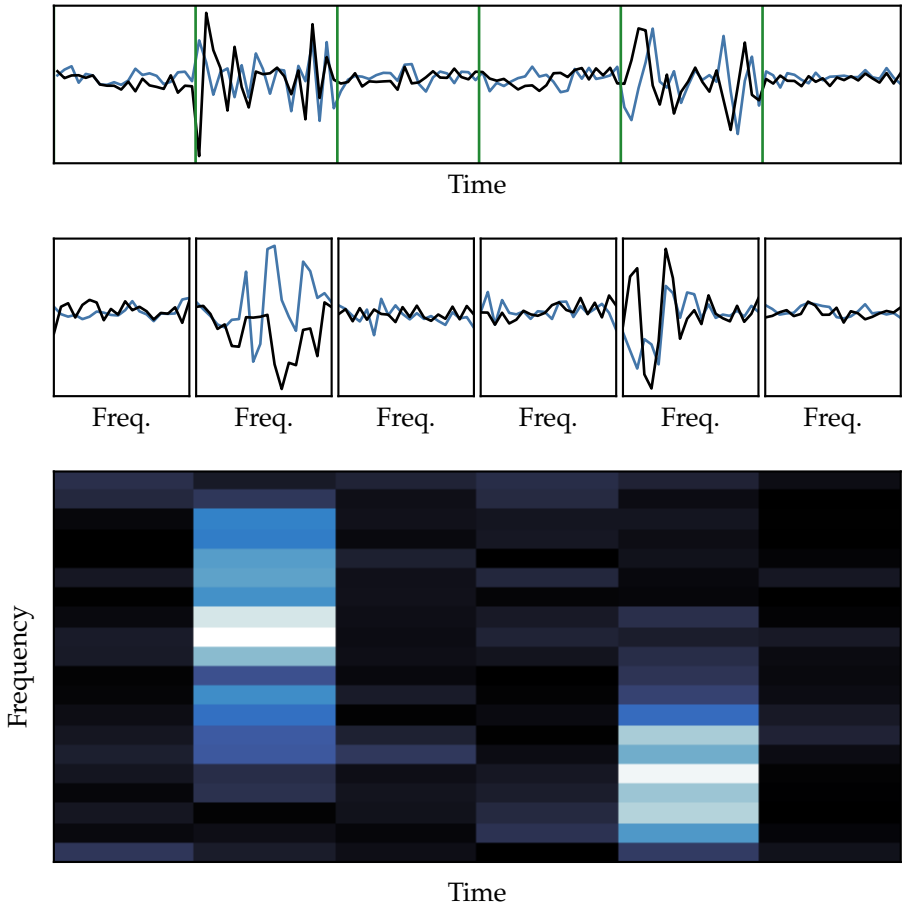

Figure 4.12: Visual representation of the process of converting a complex time series into a dynamic spectrum. Top panel: a simulated complex time series with the real component in black and the imaginary component in blue. Green lines separate sets of samples into bins of width Δt. Middle panels: the complex Fourier transforms of each of the bins, again with the real component in black and imaginary component in blue. Bottom panel: The amplitude of the dynamic spectrum created by plotting each bin's spectrum vertically, with lighter cells representing higher values.

where $\Delta\tau$ and Φ_0 are leakage terms respectively representing a time and phase offset between U and V. We derive models for the linear and circular polarisation ratios $L(f)/I(f)$ (where $L(f) = \sqrt{Q(f)^2 + U(f)^2}$ is the total linear polarisation) and $V(f)/I(f)$ of each polarisation calibrator as second-order polynomials in f by fitting spectra obtained with the Murriyang radio telescope.

4.4.3 Plot FRB high time resolution data

The final process of the high time resolution processing is to plot the data for the FRB. Because the ideal time resolution for visual inspection of an FRB dynamic spectrum can be anywhere between 1 µs and 1 ms, and the sub-millisecond structure of the FRB is not known until this stage, we plot each of the Stokes dynamic spectra over a range of time averaging values. Figure 4.13 shows this plot as generated for FRB190711, and we note recovery of the high-time resolution structure reported by Day et al. (2020).

4.5 Summary

The bringing together of CRAFT's voltage processing software into CELEBI has led to several significant improvements to the software overall. Most importantly, voltage processing is now almost entirely automated. This has reduced the turnaround between FRB detection and obtaining the final data products (high-precision localisation and high-time resolution data) from a week or more of processing requiring a close level of human oversight and manual execution, to as little as less than a day with very little direct human supervision. The precise time required for processing depends on the resources available on the supercomputing cluster CELEBI is being run on (we have largely been using the OzStar supercomputer). Also, processing can be impeded by unexpected irregularities in the data or observations that CELEBI is not yet robust to. Nextflow's handling of complex process relationships has greatly helped development, and its

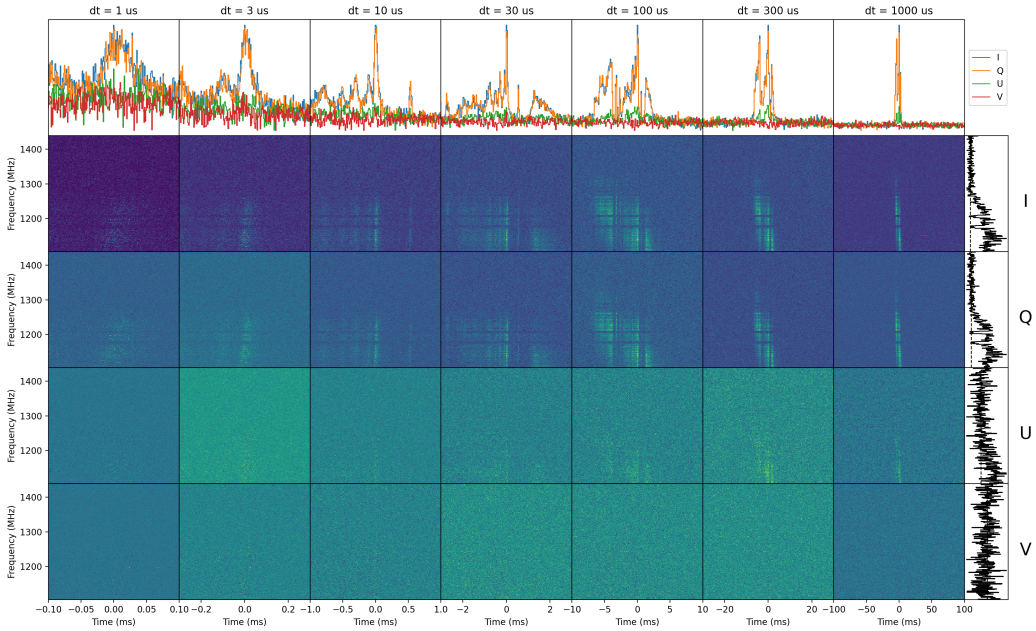

Figure 4.13: CELEBI output plot of Stokes dynamic spectra for FRB190711. Each row shows dynamic spectra for a Stokes parameter, labelled on the right, with the time averaging length labelled at the top of each column. The top row is the frequency-integrated pulse profile for each of the Stokes parameters. The rightmost column is the spectrum at the peak time index in the largest time averaging length.

method of process execution, where each instance of a process is executed in its own directory, combined with its detailed logging and reporting, makes diagnosis of problems quite straightforward and has greatly improved reproducability in processing. Processing CRAFT voltages is now much more accessible than it was previously, as the user-end interactions are much simpler and require less technical knowledge. Responsive follow-up observations, on timescales on the order of a day, of CRAFT FRBs are now a possibility with the automation of procesing CRAFT voltages.

A primary motivation for the development of CELEBI was the forthcoming CRACO upgrade for ASKAP's real-time detection system (Bannister et al., in prep). CRACO is expected to increase the rate at which ASKAP detects FRBs from of order $\sim$1 per month to of order $\sim$1 per day. This much higher detection rate will require automated processing and logging, and standardised data outputs, all of which are now provided via CELEBI.

CELEBI robustly reveals the intrinsic high-time resolution and polarimetric properties of ASKAP FRBs, free from instrumental artefacts (as demonstrated by pulsar calibration observations). This will enable the statistical examination of burst properties, including polarisation properties, as the detection rate increases and the sample of FRBs with these high quality measurements grows. Paired with high-precision and trustworthy localisations, the environments of progenitors could be studied, and comparisons made between trends in the repeating & apparently non-repeating populations.

While the primary functionality of CELEBI is now complete, development is ongoing. The processing of each FRB still requires a degree of human oversight, and processing errors are handled on a case-by-case basis. The robustness of CELEBI to issues such as data corruption, unusual antenna behaviour, calibration errors, and unexpected RFI environments is continually improving, but this can only occur as the issues arise.

There are also remaining improvements to be made to optimise the quality of

the pipeline outputs. The current method of imaging an FRB and subtracting RFI could be improved from the current binning (process 4.3.1.3) by instead correlating of order 100 bins each 1 ms in duration, and using a matched filter post-correlation to image the burst while removing RFI. This would simplify the pipeline structure by making the RFI correlation branch obsolete, give more flexibility in imaging the FRB, and maximise the S/N of the FRB in its image, therefore minimising its positional uncertainty.

The high-time resolution data products are currently output as Numpy arrays. Incorporating conversion to other standard formats, such as PSRCHIVE archives or FITS, would be convenient for using the data products with already-existing analysis software. CELEBI also does not currently include any functionality for measuring FRB RMs, a burst property which is considered a standard measurement when possible, i.e. when polarimetric data is available.

Chapter 5

The CRAFT High-Time Resolution FRB Sample

Attribution statement

This chapter is the paper entitled "The CRAFT high time resolution FRB sample", intended for submission to Proceedings of the Astronomical Society of Australia. The version presented here has been through one round of review within the Commensal Real-time ASKAP Fast Transients Collaboration, and may differ from the submitted and accepted versions. I performed data processing, analysis, and interpretation, with contributions from co-authors as listed below. The draft manuscript was written primarily by me, except where stated otherwise below, and circulated to all co-authors for review.

Marcin Glowacki provided project supervision; processed FRB data; assisted with data analysis; reviewed and edited the manuscript. Adam Deller processed FRB data; contributed to development of methodology of ASKAP voltage capture and processing; reviewed and edited the manuscript. Kelly Gourdji processed FRB data; reviewed and edited the manuscript. Apurba Bera processed FRB data. Tyson Dial processed FRB data; validated polarisation calibration. Clancy James provided project supervision and conception of work; wrote section 4.2, part of sections 4.1, 4.3, and 4.4; reviewed and edited the manuscript. Ryan Shannon

oversaw ASKAP operations for CRAFT FRB detections; curated ASKAP voltage data; contributed to the development of the methodology of ASKAP voltage capture and data processing; assisted with validation of polarimetry. Keith Bannister contributed to development of methodology of ASKAP voltage capture and data processing. Shivani Bhandari operated ASKAP for CRAFT FRB detections. Adrian Sutinjo provided project supervision.

Abstract

Fast radio bursts (FRBs) have been observed to exhibit structure on microsecond timescales. Detailed examination of these structures has been largely restricted to repeating FRBs, a potentially distinct class of transient from non-repeating FRBs, due to the time resolution of most instruments being limited when the position and arrival of a burst is not known a priori.We present microsecond-level, coherently-dedispersed, polarimetric measurements of the frequency-time structure of 21 FRBs, mostly as yet non-repeating, made with the real-time burst detection and voltage capture capabilities of the Australian Square Kilometre Array Pathfinder (ASKAP). Within this sample is a wide diversity in frequency-time morphology and polarisation properties and behaviours. We compare with the sample from the Deep Synoptic Array (DSA), and find that our sample contains more FRBs with multiple components, attributed to a higher S/N of our detections (39–507, compared to 8–98). A marginally significant anti-correlation is found within both our sample and that of DSA between rotation measure (RM) and circular polarisation. Additionally, a surprising excess of negative extragalactic RM is observed in our sample, but with no physical scenario apparent to explain the trend, this is attributed to random chance.

5.1 Introduction

The mechanisms by which fast radio bursts (FRBs) — bright and unpredictable extragalactic bursts of radiation with durations typically of order milliseconds (e.g.

Lorimer et al. 2007) — are produced are not known. The FRB population has great diversity in burst properties, including duration, spectral extent, morphology, polarisation, and the extent to which propagation effects have distorted, smeared, or otherwise shaped their signals. Some FRBs emit more than one burst, but a large majority of the burst population are apparently non-repeating (CHIME/FRB Collaboration et al., 2023b).

Models attempting to explain FRB emission abound, and it is possible that there are multiple mechanisms that can produce FRBs (Platts et al., 2019). A general constraint is that the emission process must be a coherent one, deduced from the extreme brightness temperatures ($\gtrsim 10^{32}$ K, e.g. Xiao & Dai 2022), far in excess of any known possible thermal process, and above what is allowed for synchrotron radiation (Kellermann & Pauliny-Toth, 1969).

The frequency-time morphologies of FRBs have been seen to be extremely varied, with some bursts containing one or more components of similar or varying frequency structure. Trends in morphology in bursts detected by the Canadian Hydrogen Intensity Mapping Experiment (CHIME) indicate an intrinsic difference between repeating and non-repeating FRBs, with repeating bursts tending to be narrower in bandwidth and broader in duration (Pleunis et al., 2021a).

High-time-resolution studies of FRB morphologies and properties offer great potential for discerning the nature of their emission as well as their environment (Farah et al., 2018). For example, Nimmo et al. (2022) observed in FRB 20200120E structure on timescales between ∼60 ns to 5 µs, which implies an upper limit on the emission region of 20–1500 m, ignoring relativistic beaming effects. This is inconsistent with emission from a synchrotron maser in a relativistic shock, instead favouring a magnetospheric origin. Hewitt et al. (2023) observe two distinct types of structure in FRB 20220912A: broad frequency-drifting components and extremely narrow "microshots", and propose that each arises from different emission processes.

Measured FRB polarisation properties also display diverse features and be-

haviours. These include high polarisation fractions and extremely large and variable rotation measures (RMs) (e.g. Michilli et al. 2018); changes in the degree and basis of polarisation over the durations of bursts (e.g. Cho et al. 2020); depolarization at low frequencies (Feng et al., 2022); and swings in the polarisation position angle (PA) (e.g. Luo et al. 2020). Sherman et al. (2024) recently presented high-time resolution polarimetric measurements of 25 FRBs detected by the Deep Synoptic Array (DSA), and find their sample to be consistent with all FRBs being intrinsically highly linearly polarised, with variations in the measured properties being due to effects of propagation through the media around the progenitors. Pandhi et al. (2024) perform a similar analysis for a sample of 128 FRBs detected by the Canadian Hydrogen Intensity Mapping Experiment (CHIME) for which baseband data is available, and find a consistent distribution of properties. Given this, ongoing efforts to expand the sample of FRBs studied in full polarisation at high time resolution are strongly motivated.

The Australian Square Kilometre Array Pathfinder (ASKAP, Hotan et al. 2021) is a radio interferometer at Inyarrimanha Ilgari Bundara, the Murchison Radio-astronomy Observatory, that is applied to FRB searches by the Commensal Real-time ASKAP Fast Transients (CRAFT) collaboration. Through real-time detection & voltage capture (Bannister et al., 2019b), polyphase filterbank (PFB) inversion (Morrison et al., 2020), and coherent beamforming, CRAFT is able to obtain coherently-summed measurements of the complex electric field of FRB signals in two orthogonal linear polarisations at the bandwidth-limited time resolution of $(336\,\mathrm{MHz})^{-1} \approx 3\,\mathrm{ns}$. This permits full polarimetric analysis at high-time resolution of FRBs detected with ASKAP, including one-off bursts for which the arrival times and positions are not known a priori. This has been previously demonstrated for FRB20181112A by Cho et al. (2020), and a high-time resolution imaging technique was applied to five ASKAP FRBs by Day et al. (2020).

We present a sample of 21 FRBs detected in voltages with ASKAP, for which PFB inversion and coherent beamforming have been applied to obtain extremely

high-time resolution polarimetric data. §5.2 describes the methods of detection, data processing, and subsequent analysis; in §5.3 we display the bursts themselves and results of analysis; §5.4 discusses the results, drawing interpretations from measured properties; §5.5 summarises and concludes.

5.2 Methods

5.2.1 Data acquisition

We use ASKAP's incoherent-sum FRB detection mode (Bannister et al., 2019b) to perform blind searches for dispersed pulses over a 336 MHz bandwidth, with a central frequency f_0 varying between 863.5 MHz and 1631.5 MHz. This search is able to be performed commensally with other observations. Each of ASKAP's 12 m diameter antennas is fitted with a phased-array feed which forms 36 dual-polarisation beams over a total field of view of $\sim 30\,\mathrm{deg}^2$. The signal in each of these beams is integrated to a time-resolution of between 0.864–1.728 ms, incoherently summed across antennas and searched for dispersed pulses in real time. Complex samples of the electric field in each beam of each antenna are stored in a 3.1 s-duration ring buffer, being continuously written to until an FRB is detected, at which point these voltage buffers are frozen and downloaded from all available antennas for further processing.

5.2.2 Processing

We process the raw voltages to obtain high-time resolution polarimetric data using the CRAFT Effortless Localisation and Enhanced Burst Inspection Pipeline (CELEBI, Scott et al. 2023). In short, after interferometric burst localisation, CELEBI performs polyphase filterbank inversion and beamforming to obtain the complex electric fields in two orthogonal linear polarisations (which, following the terminology used in Hotan et al. (2021), we refer to as X and Y) at the bandwidth-limited time resolution of $(336\,\mathrm{MHz})^{-1} \approx 3\,\mathrm{ns}$, coherently summed

across all antennas for which data is available. These data are initially coherently dedispersed to the DM measured at detection.

Dynamic spectra in X and Y are constructed with 336 channels of width 1 MHz and time resolution 1 µs via a 336-point complex-to-complex fast Fourier transform. Dynamic spectra in each of the Stokes parameters I, Q, U, and V are derived directly from the X and Y data. The Stokes U and V data has been polarisation calibrated to account for frequency-dependent U-V leakage.

5.2.3 Post-processing

5.2.3.1 Bad channel removal

We do not automatically flag channels to remove RFI from the data. Instead, we normalise each channel of the dynamic spectra such that the off-pulse noise has a mean of zero and standard deviation 1 (assuming Gaussian noise).

The 3.1 s duration of the voltage buffers and the latency of the real-time detection sometimes results in some of the higher-frequency components of the burst falling out of the ring buffers before they can be frozen and the data downloaded due to the dispersive time delay. We therefore remove these channels in order to avoid adding unnecessary noise to the time profiles, and to prevent the false impression of a sharp spectral cutoff in the dynamic spectra.

Once channels have been removed, we integrate the IQUV dynamic spectra over frequency to obtain the respective time series profiles.

5.2.3.2 Dedispersion

Our data are coherently dedispersed, and because we retain the X and Y polarisations, we can coherently dedisperse to any other DM without loss of quality in our data. We measure the DM of each FRB by optimising separately for S/N and structure in the I profiles.

Structure optimisation is performed using the method of Sutinjo et al. (2023), which seeks to maximise the sum of $\left(d\tilde{I}/dt\right)^2$, where $\tilde{I}$ is the FRB's I profile

averaged in time ("t-scrunched") to a δt chosen such that the profile's S/N is boosted without averaging out any apparent structure, and then smoothed via regularisation. This method identifies the structure-maximising DM, $\mathrm{DM_{struct}}$, and its uncertainty out of a range of provided trial DMs.

We optimise for S/N simultaneously with structure optimisation by identifying the trial DM that maximises S/N across boxcar convolution widths between δt and 10 ms. The uncertainty in $\mathrm{DM_{S/N}}$ corresponds to the range of DM values where the S/N is within 1 of the peak value. We define the offline $\mathrm{S/N_{DM}}$ as the S/N measured at $\mathrm{DM_{S/N}}$.

For all subsequent analysis, we dedisperse each FRB to whichever of $\mathrm{DM_{S/N}}$ or $\mathrm{DM_{struct}}$ has the smallest error estimate. This is because some FRBs have sharp structure to optimise for in their profiles, where $\mathrm{DM_{struct}}$ will be preferred, and some do not. Exceptions to this are FRBs 20190611B and 20220610A, where we choose $\mathrm{DM_{struct}}$ instead of $\mathrm{DM_{S/N}}$ as the latter obviously does not align the signal across the available frequency band, and FRB 20220918A, which is dedispersed by-eye to $656\,\mathrm{pc\,cm^{-3}}$. The latter two of these FRBs have severely limited effective observing bandwidths due to much of the burst falling off the edge of the voltage buffer before the data was frozen and dumped, which subsequently limits the ability to reliably measure dispersive delays.

5.2.3.3 Signal-to-noise

Our offline S/N is boosted due to coherent beamforming, coherent dedispersion, and higher time resolution. However, the loss of high-frequency signal in the buffer may degrade the S/N. For the sample presented here, these effects result in S/N of between 39 and 507, i.e. a gain factor between 1.5 and 16 above the real-time detection S/N.

5.2.4 Analysis

5.2.4.1 Boxcar width

We measure the approximate temporal width $w_{\rm box}$ of each FRB by finding the width of a boxcar that maximises S/N when convolved with the Stokes I time series. We t-scrunch the I time series to $\delta t = 10\,\mu$s, and convolve this profile with boxcars with widths between 1 and 1000 samples (probing time ranges between 10 us and 10 ms) and measure the peak S/N in the resulting time series. We take the optimal width as $w_{\rm box}$. The upper and lower uncertainty bounds on $w_{\rm box}$ are then found by increasing or decreasing respectively the boxcar width and calculating the peak S/N after convolution until the S/N is found to have decreased by 1.

For FRB 20191106B and FRB 20210912A, which both have two clearly distinct, well-separated components, after the first pass of the boxcar analysis we mask out the region corresponding to the first measured $w_{\rm box}$, and run the analysis again to measure $w_{\rm box}$ for the second component. For both of these FRBs, we fit RMs, polarisation fractions, scattering timescales, and scintillation decorrelation bandwidths for both of their distinct components.

FRB 20230708A also has many distinct components, but we do not measure their individual widths here as deeper analysis of the temporal profile will be presented in a future work (Dial et al., in prep). The S/N-maximising $w_{\rm box}$ includes only the primary double-peaked burst.

5.2.4.2 Rotation measure

To fit RMs, we integrate the I, Q, and U dynamic spectra of each burst over the boxcar width $w_{\rm box}$. The spectra in this integrated region are passed to RM-Tools (Purcell et al., 2020), along with the noise in each channel calculated from off-pulse regions more than 40 ms away from the burst, to measure the burst RM.

We then correct the Q and U dynamic spectra by rotating the PA by a

frequency dependent angle $\psi_{\rm RM}(f)$:

$$Q'(t,f) = Q(t,f)\cos(2\psi_{\rm RM}(f)) + U(t,f)\sin(2\psi_{\rm RM}(f)), \tag{5.1}$$

$$U'(t,f) = -Q(t,f)\sin(2\psi_{\rm RM}(f)) + U(t,f)\cos(2\psi_{\rm RM}(f)), \tag{5.2}$$

where

$$\psi_{\rm RM}(f) = {\rm RM}\left(\left(\frac{c}{f}\right)^2 - \left(\frac{c}{f_{\rm ref}}\right)^2\right), \tag{5.3}$$

where $f_{\rm ref}$ is a reference frequency, which we choose to be the top of the bandwidth. The corrected Q and U profiles are then obtained by integrating the respective dynamic spectra over frequency.

We take the Galactic RM contribution $\rm RM_{MW}$ along the line-of-sight to the FRB source as given by Hutschenreuter et al. (2022) using the `FRB` software package (Prochaska et al., 2023), and subtract this from the total RM to determine the extragalactic RM contribution $\rm RM_{EG}$.

In this work, we do not investigate for any change in RM over time within a burst.

5.2.4.3 Polarisation angle

To calculate burst PA profiles, we follow the method outlined in Day et al. (2020). To briefly summarise, we calculate the PA $\psi(t)$ by

$$\psi(t) = \frac{1}{2}\arctan\left(\frac{U'(t)}{Q'(t)}\right), \tag{5.4}$$

where $Q'(t)$ and $U'(t)$ are the RM-corrected Stokes Q and U profiles, obtained by integrating the respective dynamic spectra over frequency. The error in $\psi(t)$ is given by:

$$\sigma_\psi(t) = \frac{1}{2}\sqrt{\frac{Q'(t)^2\sigma_{U'}^2 + U'(t)^2\sigma_{Q'}^2}{\left(Q'(t)^2 + U'(t)^2\right)^2}}, \tag{5.5}$$

where $\sigma_{Q'}$ and $\sigma_{U'}$ are the errors in $Q'(t)$ and $U'(t)$ respectively, taken as the standard deviation of the profiles calculated from time regions more than 40 ms

separated from the peak of a burst. We then plot only time steps where $\sigma_\psi(t) \leq 10°$.

5.2.4.4 Polarisation fractions

We calculate the linear polarisation fraction as

$$L(t) = \sqrt{\left(\frac{Q'(t)}{\sigma_{Q'}}\right)^2 + \left(\frac{U'(t)}{\sigma_{U'}}\right)^2}. \tag{5.6}$$

The de-biased total linear polarisation, following Day et al. (2020), is

$$L_{\mathrm{de-bias}}(t) = \begin{cases} \sigma_I \sqrt{\left(\frac{L}{\sigma_I}\right)^2 - 1} & \frac{L}{\sigma_I} > 1.57 \\ 0 & \text{otherwise,} \end{cases} \tag{5.7}$$

where σ_I is the standard deviation of off-pulse noise in the $I(t)$ profile.

We then integrate the $I(t)$, $L_{\mathrm{de-bias}}(t)$, and $V(t)$ profiles over the boxcar width w_{box} to obtain $\bar{I}$, $\bar{L}$, and $\bar{V}$, and calculate the linear and circular polarisation fractions $\bar{L}/\bar{I}$ and $\bar{V}/\bar{I}$ respectively, and the total polarisation fraction

$$\frac{P}{I} = \frac{\bar{L}^2 + \bar{V}^2}{\bar{I}^2}. \tag{5.8}$$

We note that this is the same order of operations as applied by Sherman et al. (2024) to obtain circular polarisation fractions.

5.2.4.5 Scattering

We apply the Bayesian methods presented by Qiu et al. (2020) to fit integrated burst profiles for simple bursts with single components for scattering timescales τ and apparent widths w_s. The model is constructed by convolving a Gaussian of width w_s with an exponential decay function with a decay time of τ. We do not need to account for intrachannel dispersion smearing as Qiu et al. (2020) do because we have dedispersed our data coherently.

We also scale τ to its expected value at a central frequency of 1 GHz assuming

a power law dependence on frequency $\tau \propto f^{-4}$:

$$\tau_{1\,\mathrm{GHz}} = \left(\frac{f_0}{1\,\mathrm{GHz}}\right)^4 \tau, \tag{5.9}$$

where f_0 is the actual central frequency.

This method produced good fits for 11 of our 21 bursts.

5.3 Results

We consider the 44 bursts ASKAP detected between real-time FRB detection and voltage capture becoming possible (the first burst being FRB 20180924, Bannister et al. 2019b) and July 18 2023. We exclude 11 of these that were detections of the previously-discovered repeating FRB 20201124A (Fong et al., 2021), and a further 12 bursts for which no suitable voltage data was available. In general, this was because either the voltage download was not triggered (bursts detected above a given width threshold were not triggered due to challenges with false positives due to RFI), or the voltage download did not completed correctly (on some occasions, only a single polarisation was downloaded, or only a small subset of the frequency channels and/or antennas completed the download). FRB 20181112A was excluded from reprocessing with CELEBI for this last reason, but we quote properties measured from high-time resolution data by Cho et al. (2020) where possible. This leaves us with 21 bursts in our fully-processed sample to date.

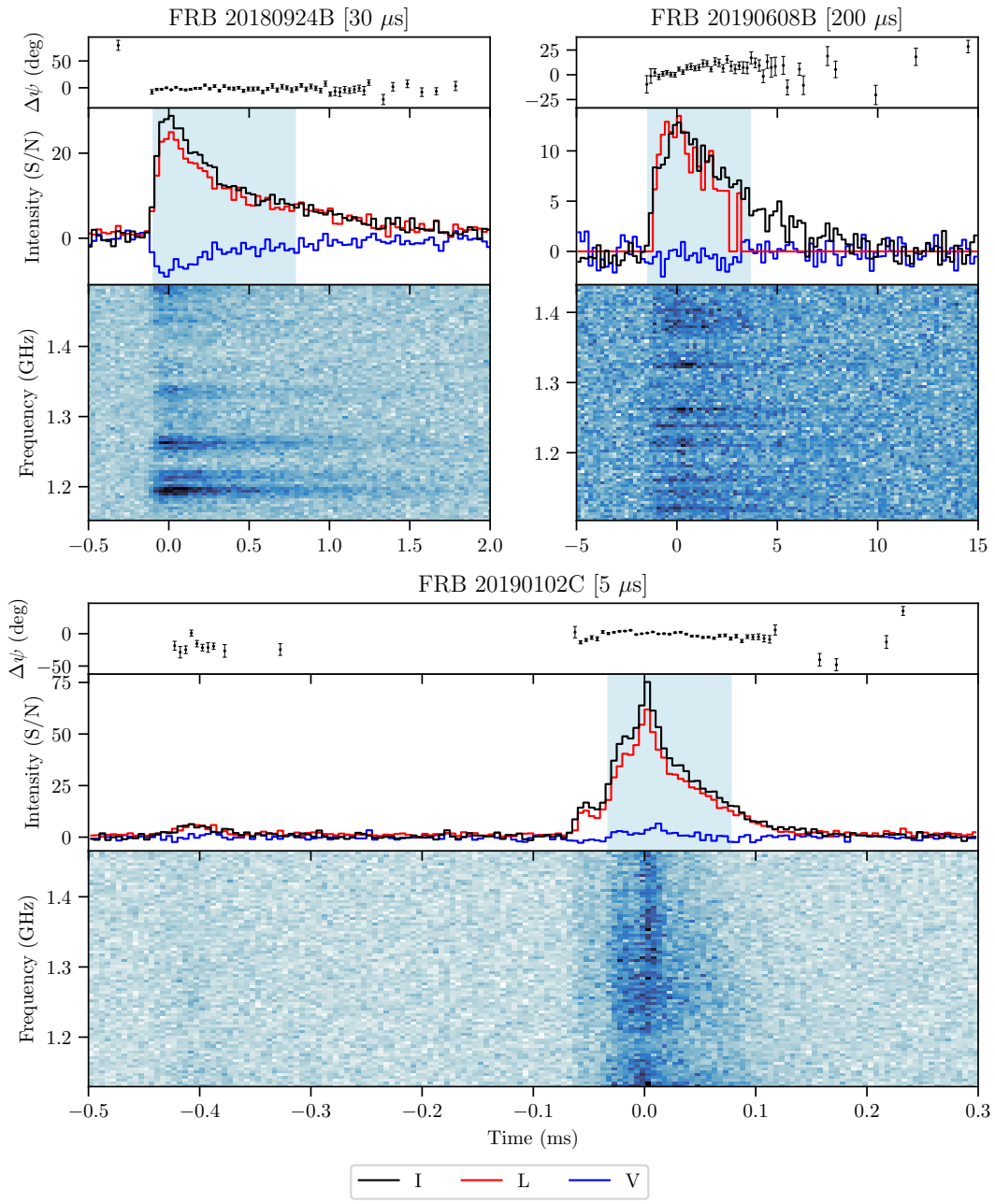

Figure 5.1: High-time resolution dynamic spectra and polarimetric profiles of the FRBs in our sample. The time axis is relative to the bin with the peak I profile. (For each subplot) Top panel: PA relative to the value at the peak time index ($\Delta\psi = \mathrm{PA}(t) - \mathrm{PA}(0)$). Middle panel: Profiles of total intensity I, linear polarisation L, and circular polarisation V, with the region corresponding to the optimal fitted boxcar of width w_{box} shaded in blue. Bottom panel: Stokes I dynamic spectrum with frequency resolution 4 MHz. The title of each subplot is the FRB's name and its plotted time resolution. Frequencies above the crossing frequency (where the FRB is expected to fall off the edge of the voltage buffer due to its dispersive sweep) are greyed out. All bursts have been coherently dedispersed to the DM indicated in Table 5.1, and corrected for Faraday rotation by their respective RM.

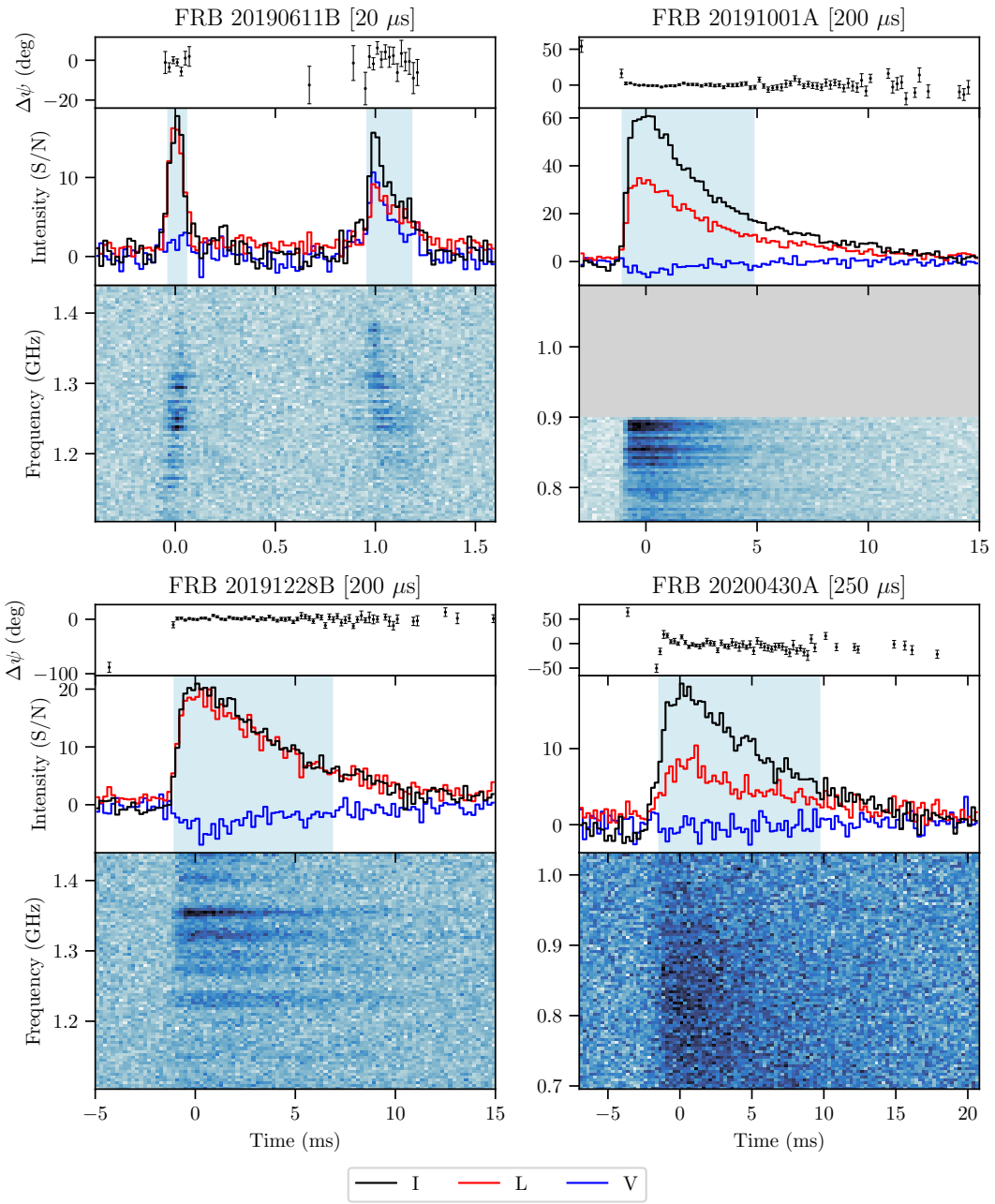

Figure 5.1: (cont.)

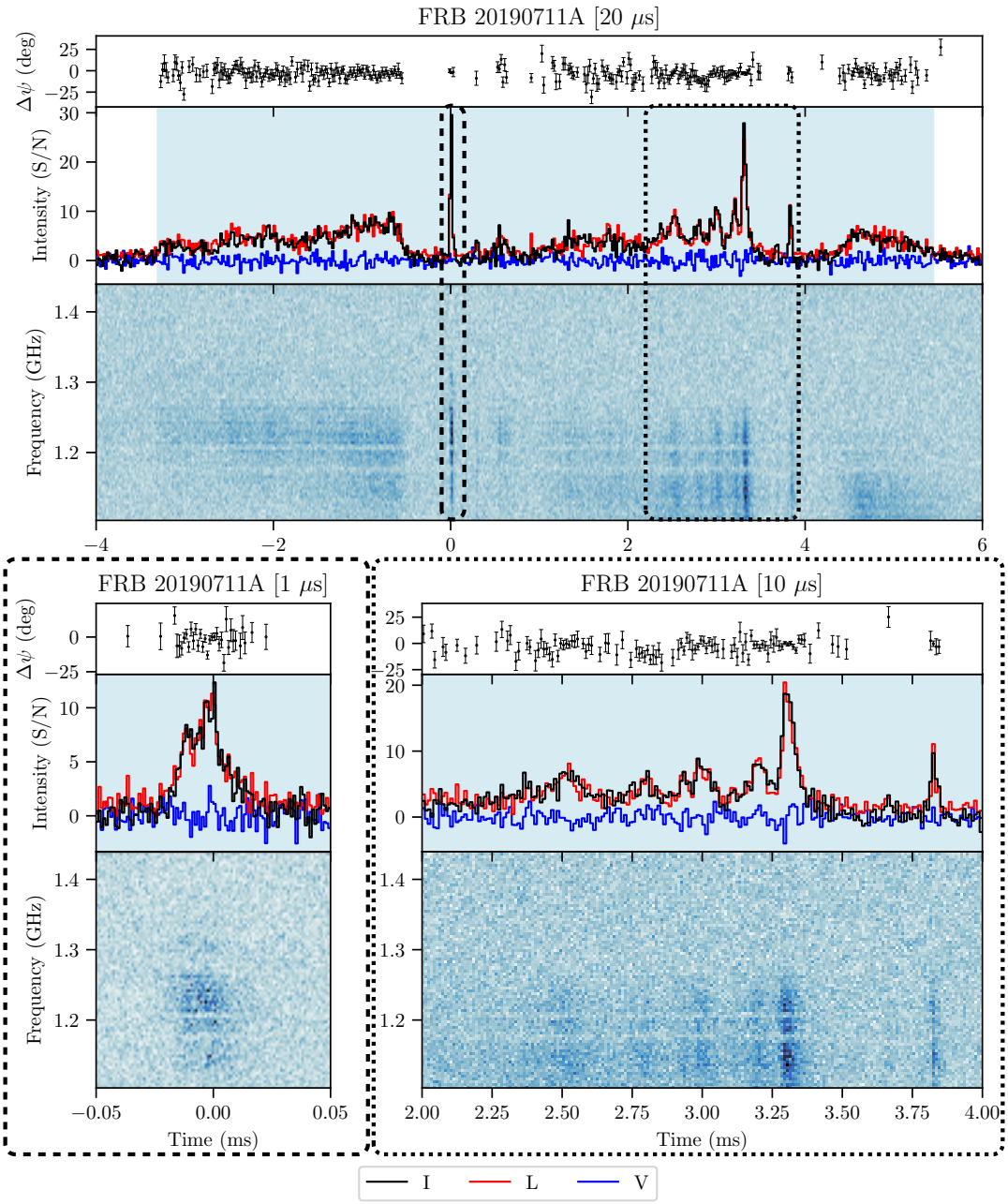

Figure 5.1: (cont.) Note that the subplots shown on this page are different views of FRB 20190711A.

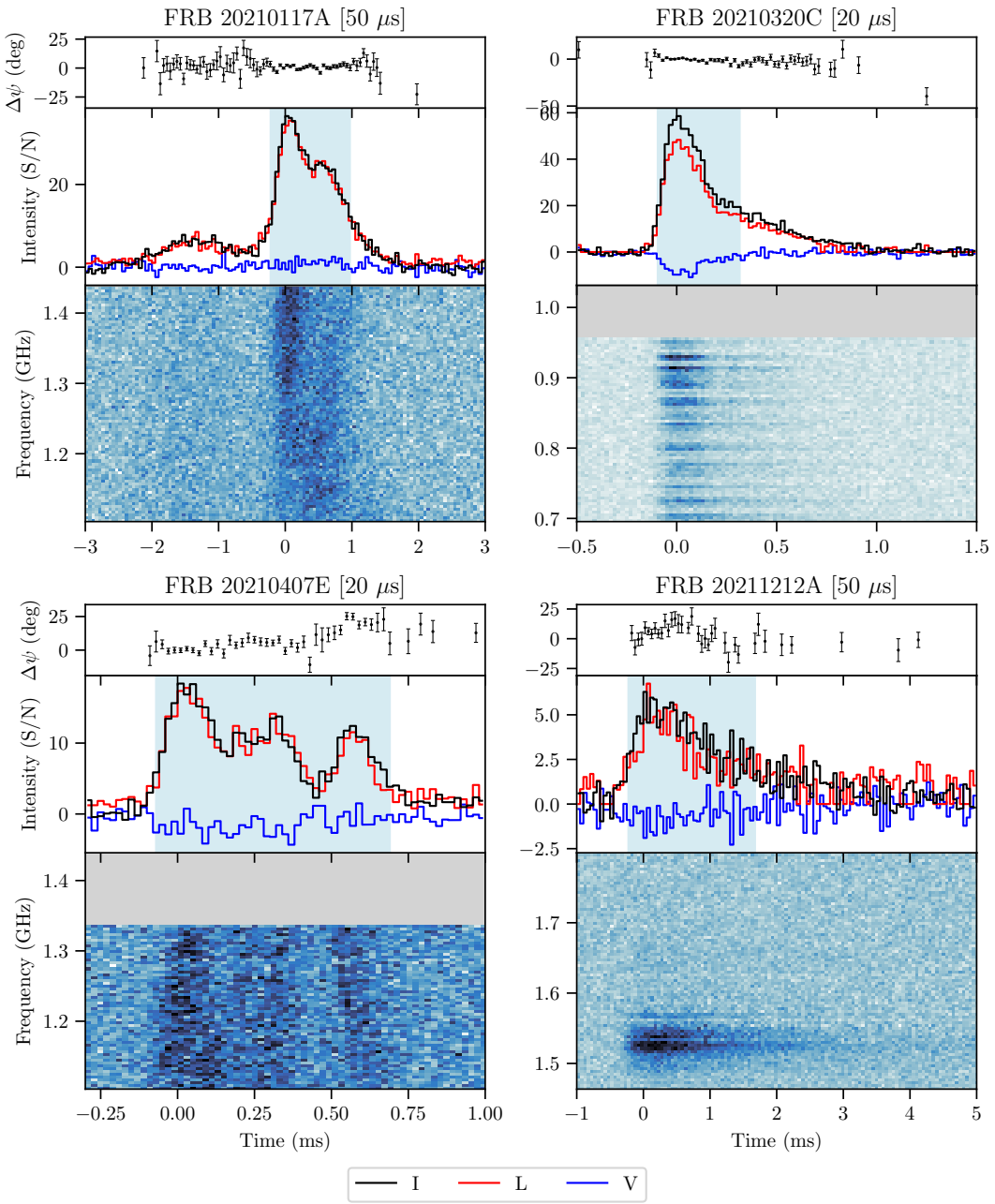

Figure 5.1: (cont.)

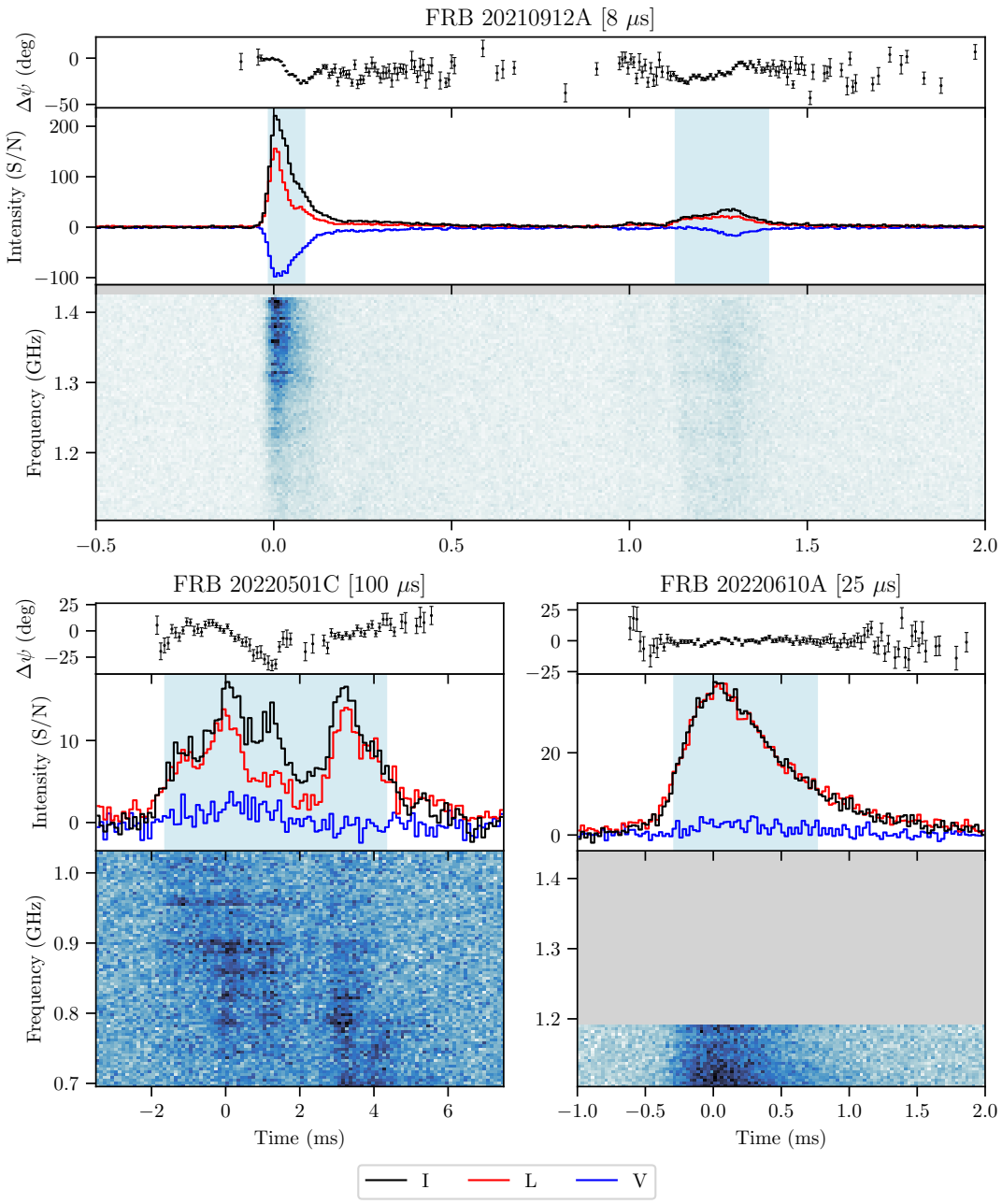

Figure 5.1: (cont.)

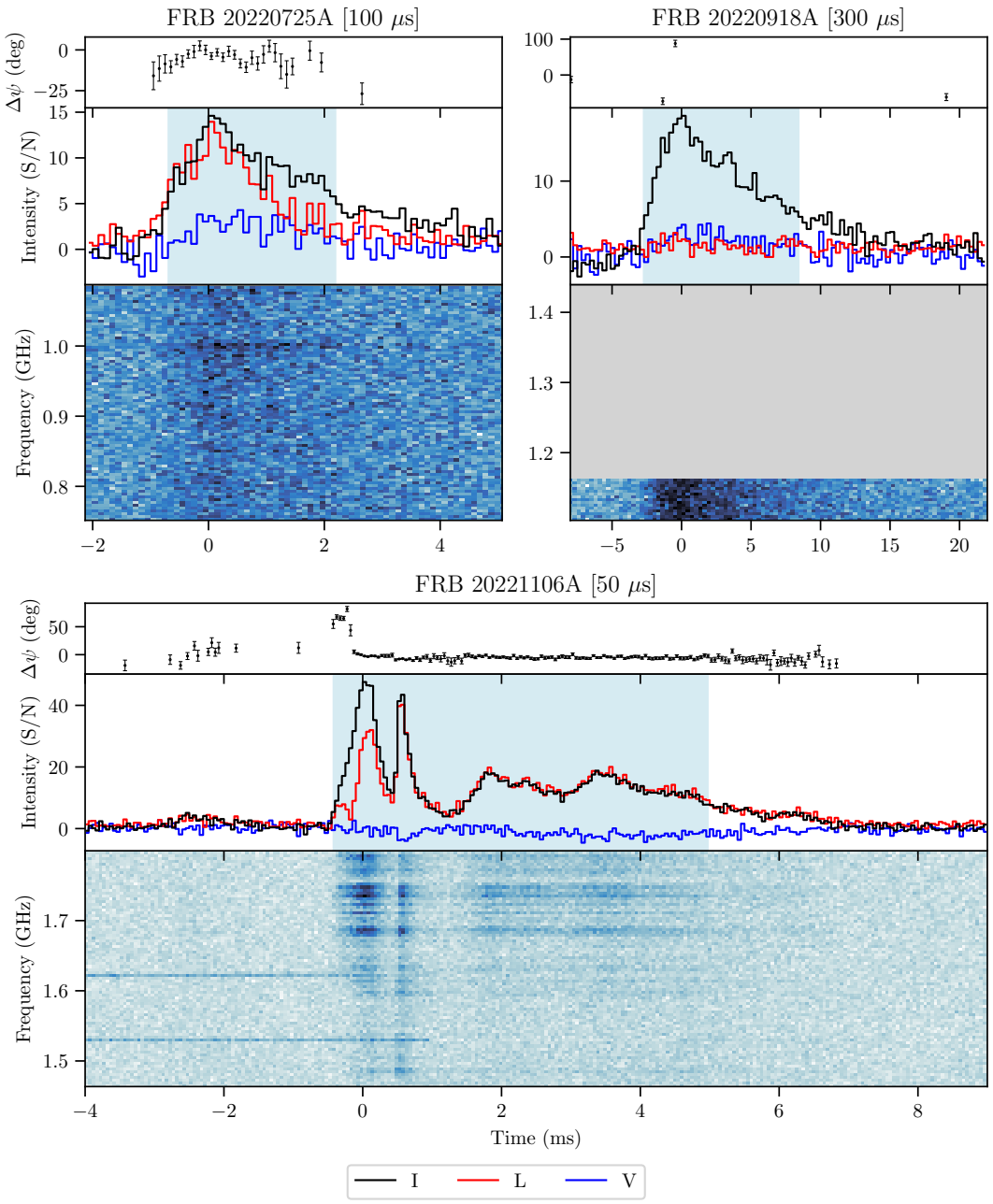

Figure 5.1: (cont.)

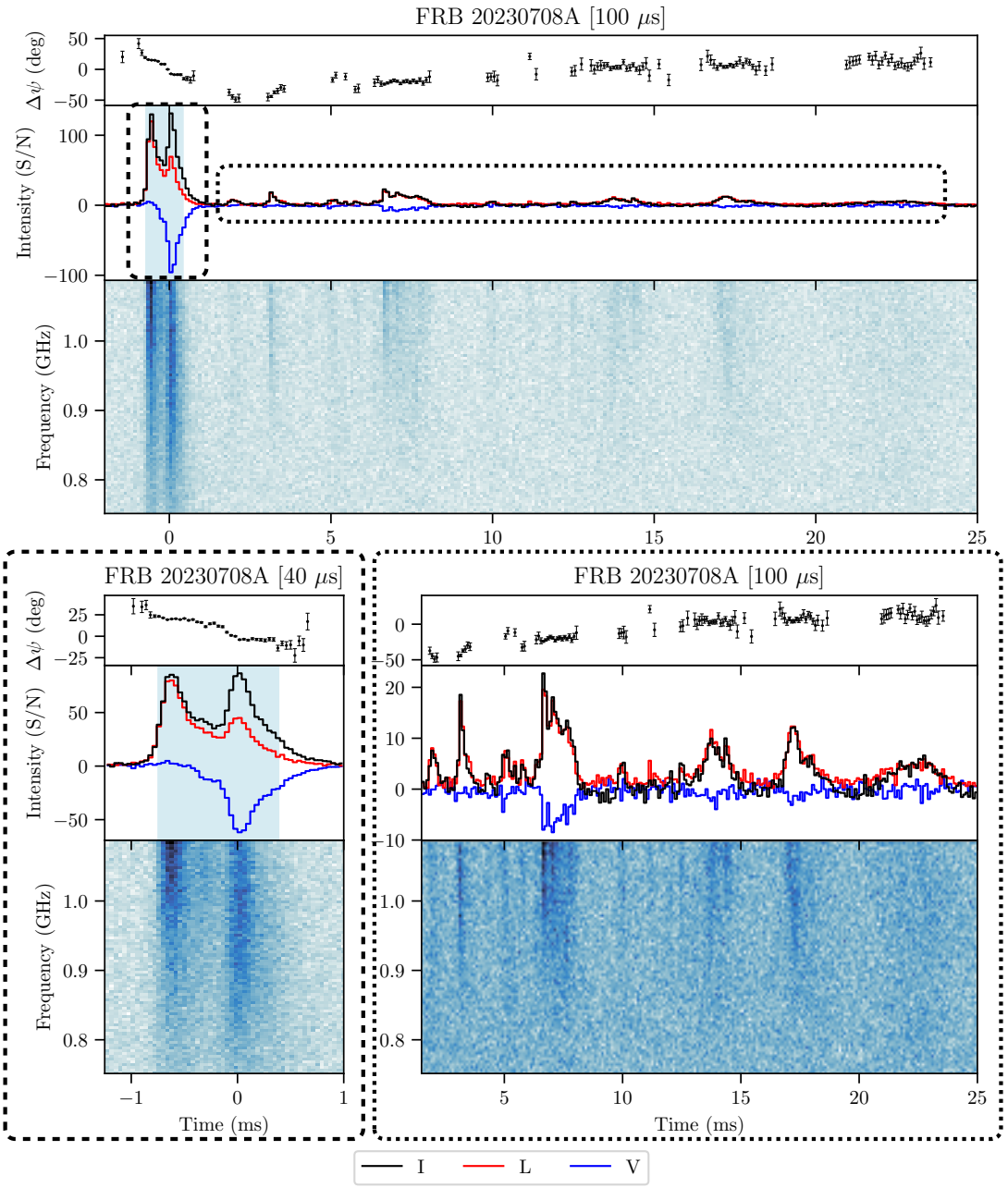

Figure 5.1: (cont.) Note that the subplots shown on this page are different views of FRB 20230708A.

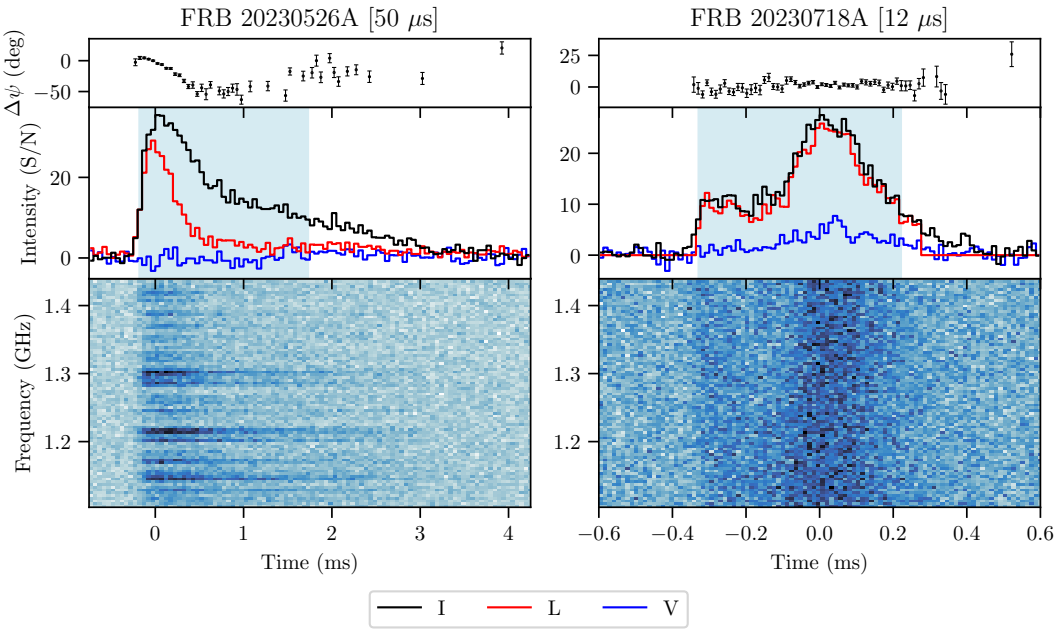

Figure 5.1: (cont.)

Table 5.1: Measured properties of the bursts in our sample. The selected DM value for each FRB is highlighted in bold.
[a]Cho et al. (2020)
[b]Sammons et al. (2023)
[c]The by-eye value of 656 pc cm^{-3} is used for FRB 20220918A's DM

FRB	f_0 (MHz)	$n_{\rm ant}$	S/N$_{\rm det}$	S/N$_{\rm DM}$	DM$_{\rm S/N}$	DM$_{\rm struct}$	τ (ms)	$\tau_{1\,\rm GHz}$ (ms)	w_s (ms)
20180924B	1320.0	24	21.08	123	$361.75^{+0.01}_{-0.02}$	$\mathbf{361.74^{+0.2}_{-0.08}}$	0.52 ± 0.02	$1.57^{+0.06}_{-0.05}$	0.026 ± 0.002
20181112A[a]	1297.5	11	19.3	-	589.265 ± 0.001	-	0.0278 ± 0.0008[b]	0.078 ± 0.002	-
20190102C	1297.5	23	14.00	209	$\mathbf{364.55^{+0.02}_{-0.01}}$	$364.55^{+0.03}_{-0.02}$			
20190608B	1271.5	25	16.08	72	340 ± 1	$\mathbf{338.7^{+1}_{-0.8}}$	$4.1^{+0.3}_{-0.4}$	10.8 ± 0.9	0.7 ± 0.1
20190611B	1271.5	20	9.54	65	322.4 ± 0.1	$\mathbf{322.7^{+0.4}_{-0.2}}$			
20190711A	1271.5	28	23.82	114	592 ± 2	$\mathbf{587.74^{+0.03}_{-0.02}}$			
20191001A	919.5	30	37.08	186	$\mathbf{507 \pm 0.3}$	$507^{+0.6}_{-0.7}$	4.25 ± 0.05	$3.04^{+0.04}_{-0.03}$	0.23 ± 0.01
20191228B	1271.5	21	22.92	108	$\mathbf{297 \pm 1}$	296 ± 2	6.2 ± 0.3	16.3 ± 0.8	$0.57^{+0.08}_{-0.07}$
20200430A	863.5	26	13.85	91	$379.9^{+0.6}_{-0.5}$	$\mathbf{379.6^{+0.7}_{-0.4}}$	7.9 ± 0.4	4.4 ± 0.2	0.76 ± 0.07
20210117A	1271.5	21	17.71	158	$\mathbf{729.2^{+0.2}_{-0.1}}$	$729.1^{+0.5}_{-0.2}$			
20210320C	863.5	24	15.32	172	384.6 ± 0.02	$\mathbf{384.59^{+0.03}_{-0.01}}$	0.254 ± 0.006	0.141 ± 0.004	0.037 ± 0.002
20210407E	1271.5	15	19.07	61	$\mathbf{1784.8 \pm 0.2}$	$1784.9^{+0.3}_{-0.4}$			
20210912A	1271.5	22	31.19	507	$\mathbf{1233.72^{+0.01}_{-0.02}}$	$1233.7^{+0.03}_{-0.02}$			
20211212A	1631.5	24	10.50	83	$\mathbf{200^{+2}_{-1}}$	200^{+4}_{-3}	$1.52^{+0.05}_{-0.04}$	10.8 ± 0.3	0.15 ± 0.01
20220501C	863.5	23	14.81	117	$449.6^{+0.2}_{-0.4}$	$\mathbf{449.1^{+0.3}_{-0.2}}$			
20220610A	1271.5	22	23.86	89	$\mathbf{1458.1^{+0.3}_{-0.5}}$	$1457.6^{+0.8}_{-0.9}$	0.51 ± 0.01	1.34 ± 0.03	0.172 ± 0.004
20220725A	919.5	25	10.87	62	$290.1^{+0.3}_{-0.4}$	$\mathbf{290^{+0.2}_{-0.3}}$	$2.3^{+0.2}_{-0.1}$	1.7 ± 0.1	0.39 ± 0.03
20220918A[c]	1271.5	24	26.27	39	$\mathit{643^{+6}_{-5}}$	$\mathit{660^{+20}_{-30}}$	$7.9^{+0.4}_{-0.3}$	20.6 ± 0.9	0.98 ± 0.07
20221106A	1631.5	21	19.71	205	$343.2^{+0.7}_{-0.9}$	$\mathbf{343 \pm 0.3}$			
20230526A	1271.5	22	22.09	151	316.2 ± 0.2	$\mathbf{316.1^{+0.3}_{-0.1}}$	1.31 ± 0.03	$3.44^{+0.08}_{-0.09}$	0.073 ± 0.006
20230708A	919.5	23	30.50	290	$\mathbf{411.54^{+0.05}_{-0.04}}$	$411.52^{+0.08}_{-0.05}$			
20230718A	1271.5	22	10.91	121	476.67 ± 0.09	$\mathbf{476.64^{+0.08}_{-0.1}}$			

Table 5.2: Continued measured properties of the bursts in our sample. Values for each distinct component of FRBs 20190611B and 20210912A are included where relevant.
[a]Cho et al. (2020)

FRB	$w_{\rm box}$ (ms)	RM (rad m^{-2})	RM$_{\rm MW}$ (rad m^{-2})	RM$_{\rm EG}$ (rad m^{-2})	L/I	$\lvert V\rvert/I$	P/I
20180924B	0.9 ± 0.2	-9 ± 2	16 ± 5	-25 ± 5	0.763 ± 0.002	0.226 ± 0.002	0.796 ± 0.002
20181112A[a]	-	10.5 ± 0.4	16 ± 6	-6 ± 6	0.92	-	0.94
20190102C	$0.11^{+0.01}_{-0.03}$	112.7 ± 0.4	27 ± 8	86 ± 8	0.784 ± 0.001	0.055 ± 0.001	0.786 ± 0.001
20190608B	$5.1^{+2}_{-0.8}$	-353 ± 1	-20 ± 10	-330 ± 10	0.88 ± 0.005	0.07 ± 0.004	0.883 ± 0.005
20190611B	$0.09^{+0.06}_{-0.02}$	-17 ± 2	30 ± 10	-50 ± 10	0.84 ± 0.01	0.11 ± 0.01	0.85 ± 0.01
	$0.22^{+0.2}_{-0.06}$	-17 ± 2		-50 ± 10	0.576 ± 0.007	0.6 ± 0.01	0.834 ± 0.008
20190711A	$8.8^{+0.6}_{-0.5}$	-8.9 ± 0.6	19 ± 6	-28 ± 7	0.7836 ± 0.0005	0.0124 ± 0.0005	0.7837 ± 0.0005
20191001A	$5.9^{+0.6}_{-1}$	-53.8 ± 0.2	23 ± 4	-77 ± 4	0.5593 ± 0.0008	0.0629 ± 0.0009	0.5629 ± 0.0008
20191228B	8 ± 2	-13.9 ± 0.8	18 ± 6	-32 ± 6	0.848 ± 0.002	0.182 ± 0.002	0.867 ± 0.002
20200430A	11^{+3}_{-2}	-195.3 ± 0.7	15 ± 7	-210 ± 7	0.34 ± 0.002	0.031 ± 0.002	0.342 ± 0.002
20210117A	1.2 ± 0.1	43.7 ± 0.8	3 ± 9	40 ± 9	0.918 ± 0.002	0.042 ± 0.002	0.919 ± 0.002
20210320C	$0.41^{+0.07}_{-0.1}$	-289.3 ± 0.1	-3 ± 6	-287 ± 6	0.834 ± 0.001	0.165 ± 0.001	0.851 ± 0.001
20210407E	$0.76^{+0.1}_{-0.08}$	10 ± 1	-60 ± 30	70 ± 30	0.795 ± 0.002	0.146 ± 0.002	0.808 ± 0.002
20210912A	0.1 ± 0.02	7.1 ± 0.2	8 ± 4	-1 ± 4	0.5772 ± 0.0005	0.503 ± 0.0007	0.7656 ± 0.0006
	$0.26^{+0.04}_{-0.03}$	-9.1 ± 0.8		-18 ± 4	0.663 ± 0.001	0.39 ± 0.003	0.725 ± 0.001
20211212A	1.9 ± 0.4	-30 ± 3	6 ± 6	-36 ± 6	0.386 ± 0.002	0.152 ± 0.002	0.415 ± 0.002
20220501C	$6^{+0.7}_{-0.4}$	-35.9 ± 0.3	10 ± 5	-46 ± 5	0.581 ± 0.001	0.059 ± 0.002	0.584 ± 0.001
20220610A	$1.1^{+0.1}_{-0.2}$	-216 ± 0.4	12 ± 5	-228 ± 5	0.924 ± 0.001	0.0832 ± 0.0009	0.927 ± 0.001
20220725A	$2.9^{+2}_{-0.3}$	25.2 ± 0.6	10 ± 3	15 ± 4	0.586 ± 0.003	0.232 ± 0.004	0.631 ± 0.003
20220918A	11^{+4}_{-2}	-480 ± 10	15 ± 9	-500 ± 10	0.072 ± 0.002	0.182 ± 0.002	0.195 ± 0.002
20221106A	$5.4^{+0.6}_{-0.3}$	-447 ± 1	40 ± 10	-480 ± 10	0.7814 ± 0.0005	0.0803 ± 0.0005	0.7855 ± 0.0005
20230526A	$1.9^{+0.6}_{-0.3}$	-613 ± 2	10 ± 6	-622 ± 6	0.3426 ± 0.0009	0.01 ± 0.001	0.3428 ± 0.0009
20230708A	$1.13^{+0.09}_{-0.07}$	6.6 ± 0.1	40 ± 10	-40 ± 10	0.6873 ± 0.0004	0.3799 ± 0.0005	0.7853 ± 0.0004
20230718A	$0.55^{+0.08}_{-0.04}$	-243.1 ± 0.9	190 ± 50	-430 ± 50	0.839 ± 0.002	0.173 ± 0.001	0.857 ± 0.002

Figure 5.1 is a gallery of the 21 FRBs in our sample, in roughly chronological order (deviations are to allow for larger plots for certain bursts). The time resolution for each FRB has been chosen by eye in order to display the structure of each burst with sufficient S/N. Tables 5.1 and 5.2 list the observational parameters and measured burst properties of each FRB.

The high-time resolution properties of a number of the FRBs included in this sample have previously been studied. Day et al. (2020) presented FRBs 20180924B, 20190102C, 20190608B, 20190611B, and 20190711A, although these high time resolution data were obtained via an imaging method (with a maximum time resolution of 0.05 – 0.2 ms), rather than by PFB inversion and coherent beamforming. Bhandari et al. (2023) included analysis of FRB 20210117A at high time resolution.

5.4 Discussion

In this section, we examine the patterns seen from analysing the spectro-temporal-polarimetric properties of our ensemble of 21 ASKAP bursts, and highlight tentative trends worthy of close examination in future, larger datasets.

5.4.1 Morphological overview

Table 5.3: Classifications of our sample of FRBs, where we use a scheme similar to that used by Sherman et al. (2024).
* Repeating FRB
[a] Cho et al. (2020).

	Unpolarized $L/I < 0.34, \lvert V\rvert/I < 0.3$	Partially Depolarized $0.34 \leq L/I < 0.7, \lvert V\rvert/I < 0.3$	Circularly Polarized $\lvert V\rvert/I > 0.3$	Linearly Polarized $L/I > 0.7, \lvert V\rvert/I < 0.3$
Multi, PA Varies		20220501C	20210912A 20230708A	20181112A[a] 20210407E 20221106A
Multi, PA Constant			20190611B	20190102C 20190711A* 20210117A 20230718A
Single, PA Varies		20211212A 20220725A 20230526A		20220610A
Single, PA Constant	20220918A	20191001A 20200430A		20180924B 20190608B 20191228B 20210320C

Our sample shows a wide diversity in burst morphology and properties, much of which is only accessible with our extremely high-time-resolution data. Ten of the FRBs presented here, and also FRB 20181112A (Cho et al., 2020), have complex time profiles, in which we include bursts with multiple distinct components and bursts with multi-peaked structure within individual components. Only one burst in our sample has been observed to repeat (FRB 20190711A), but at least one other (FRB 20220501C) clearly displays the hallmarks of a repeater, in particular frequency downdrifting (the "sad trombone" effect) plus a broader pulse duration and limited bandwidth.

Indeed, the PA variation in our FRBs can be quite complex: FRB 20210912A exhibits rapid PA changes near the peaks of its two pulses, which we interpret elsewhere (Bera et al. 2024, submitted); FRB 20221106A has constant PA for most of its duration, but a sudden change near the onset of the burst; FRB 20230708A has an approximately linear PA swing near its primary double-pulse, consistent with the mostly linear PA trends observed for other FRBs (e.g. Luo et al., 2020), but a reversal of the trend for its later components; and FRB 20220501C exhibits two sharp reversals in its PA swing.

We find similarly diverse polarisation properties — in particular, changes in polarisation fractions over the duration of seven bursts in our sample (plotted in Figure 5.2). The nature of these changes is diverse, including: drop in total polarisation (FRBs 20220725A and 20230526A); conversion from linear to circular polarisation within individual burst components (both components of FRB 20210912A; see also FRB 20181112A, Cho et al. 2020); conversion from linear to circular polarisation between apparently distinct burst components (FRB 20190611B and the two brightest peaks of FRB 20230708A); and complex increasing/decreasing linear polarisation within complex-profile bursts (FRBs 20221106A and 20220501C). Additionally, these changes in polarisation fractions are typically correlated with changing PAs, and are typically not present when a burst has a flat PA.

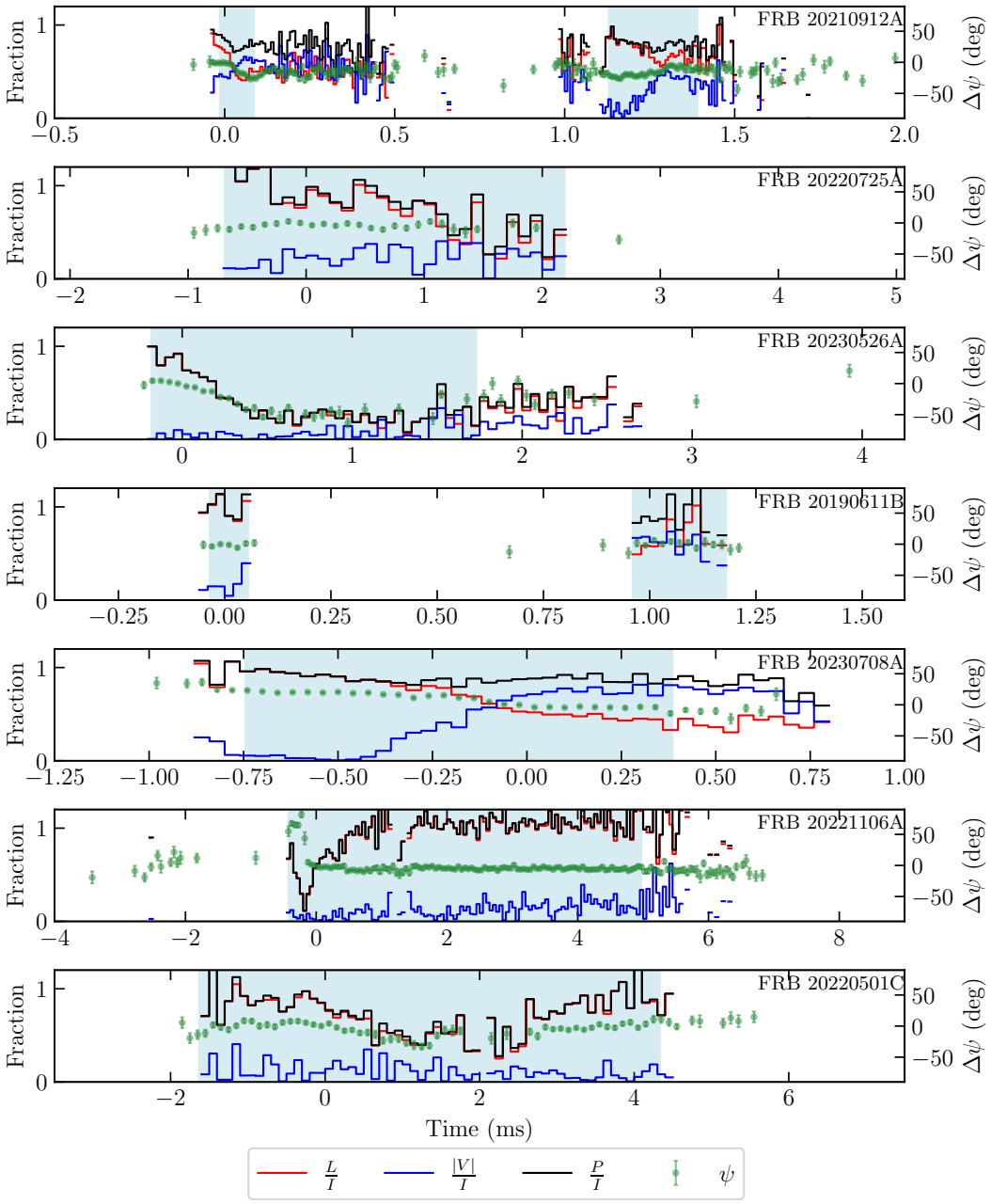

Figure 5.2: Varying polarisation fractions in our sample. Relative polarisation PAs are also plotted. The time ranges are set to match with those in Figure 5.1. Blue shaded regions are the boxcar-fitted burst regions, as plotted in Figure 5.1.

Given the rapidly changing nature of these polarisation properties, typically on timescales of $\sim 100\,\mu$s, we attribute these to properties of plasmas in the very near vicinity of the progenitor or at the point of emission, e.g. in the magnetosphere of a neutron star.

5.4.2 Classification, and comparison with DSA and CHIME/FRB

For comparative purposes, we employ the same classification scheme of Sherman et al. (2024) and Pandhi et al. (2024), which was developed based on the most similarly scoped FRB samples: 25 FRBs detected by the Deep Synoptic Array (DSA; time resolution 32.768 µs), and 128 non-repeating FRBs detected by the Canadian Hydrogen Intensity Mapping Experiment (CHIME/FRB; time resolution 2.56 µs). This scheme morphologically classifies FRBs as those with single/multiple components, and those with constant and variable PA; and divides them according to unpolarised ($L/I < 0.35, |V|/I < 0.3$), partially polarised ($0.35 < L/I < 0.7, |V|/I < 0.3$), linearly polarised ($L/I > 0.7, |V|/I < 0.3$), and circularly polarised ($|V|/I > 0.3$) bursts. We slightly amend these criteria, such that the (somewhat arbitrary) threshold between unpolarised and partially polarised FRBs is $L/I = 0.34$, since two of our FRBs lie in the $0.34 \leq L/I \leq 0.35$ range, while our "unpolarised" FRB has $L/I = 0.072$. The high S/N of our data means that we are more likely to identify multiple components, and/or inconsistencies with a constant PA. We therefore use a "by-eye" analysis, rather than a strict statistical test, to determine which category FRBs fall into. The allocation of our FRBs to these categories is given in Table 5.3.

We compare our entire FRB sample with those reported by DSA, and our 21 significantly polarised FRBs against the 88 FRBs with significant polarisation from CHIME/FRB for which a classification is presented. The major difference is that we find more FRBs with multiple components (11/22, vs. 4/25, and 11/21 vs. 29/88). This is likely due to the higher offline S/N_{DM} of the sample presented here (39–507, compared to 8–98 and approximately 10–500

for CHIME/FRB; CHIME/FRB Collaboration et al., 2023a) — three multi-component FRBs (20190102C, 20210117A, 20210912A) and potentially a fourth (20230718A) would likely be identified as single-component bursts if S/N was reduced, making the results more consistent. Similarly, we also detect a much higher fraction with varying PA (10/22, vs. 4/25, and 10/21 vs. 19/88) — FRB 20220725A would likely not be detected as having time-varying PA at lower S/N, but we find a sinusoidal pattern with ~ 1 ms period; and fewer unpolarised FRBs (1/22, vs. 5/25 for DSA and 30/118 for CHIME/FRB).

We further identify a new sub-category of FRBs: those with a scatter-like break in their intensity profile, seen in FRBs 20210320C, 20230526A, and potentially 20180924B. These have an intensity profile which closely mimics an exponential scattering decay law, but which exhibits a clear break from rapid to slow decay, inconsistent with expectations from scattering (the frequency-dependence is clearly inconsistent with $\tau_{\rm scat} \sim \nu^{-4}$ for 20210320C, though potentially consistent for the other two). In the case of FRB 20230526A, the initial, rapidly decaying part of the burst is significantly linearly polarised, while the latter, slowly decaying part is initially unpolarised but has a rising circularly polarised fraction. FRB 20210320C, and 20180924B have constant polarisation properties across their bursts. The secondary, slow-decay behaviour may be related to the long, shallow "feet" seen in FRBs such as 20210912A (this work) and 20181112A (Cho et al., 2020). Note that we treat both the rapidly and slowly decaying parts as a single-component for purposes of morphological classification, since their intensity profiles decrease monotonically away from the peak. This class of FRBs suggests caution when interpreting measured scattering parameters of FRBs, since a high S/N is required to differentiate between scattering and such presumably intrinsic behaviour.

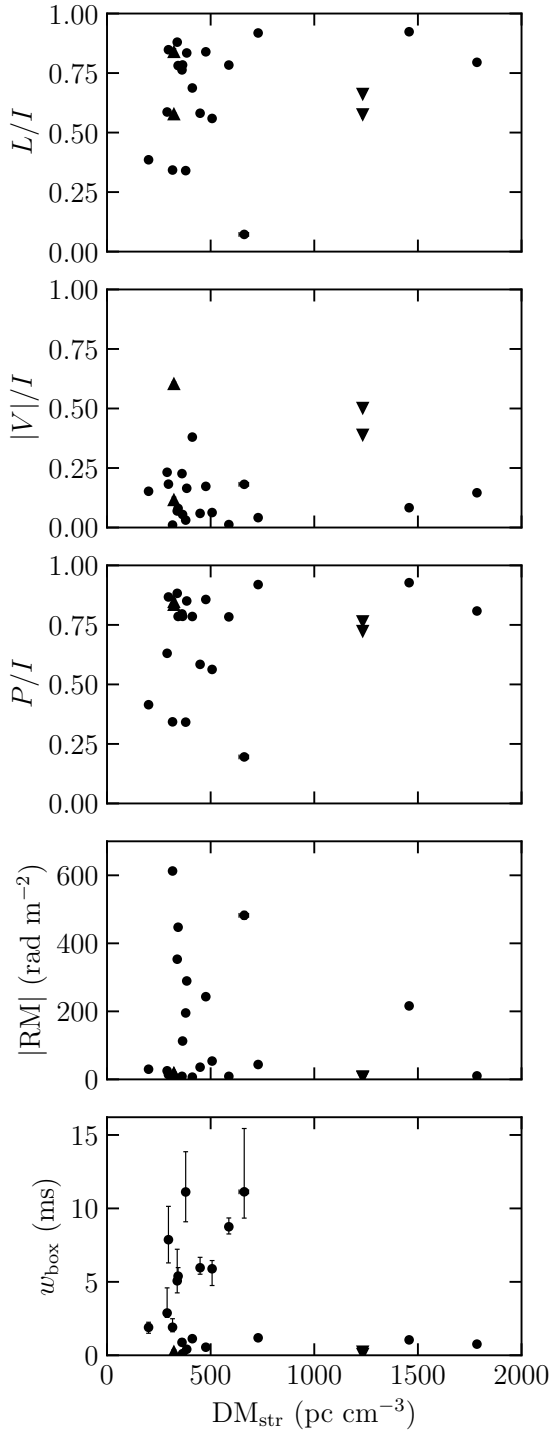

Figure 5.3: Polarisation fractions, |RM|, and boxcar widths vs structure-maximising DM for all the bursts in our sample. The separate components of FRBs 20190611B and 20210912A are plotted as upwards-pointing and downwards-pointing triangles respectively.

5.4.3 High-DM FRBs relatively unaffected by turbulent intervening media

FRBs 20210407E, 20210912A, and 20220610A have exceptionally high DMs relative to the rest of the sample, the great majority of which is likely attributable to the intergalactic medium (Macquart et al., 2020). James et al. (2022) reports that the host galaxy of FRB 20210407E was not detectable due to Galactic extinction, Marnoch et al. (2023) limits the redshift of FRB 20210912A to be > 0.7 based on the non-detection of the FRB host in optical follow-up, while Ryder et al. (2023) measured FRB 20220610A's host galaxy to be at a redshift of 1.016 ± 0.002, the furthest confirmed FRB host distance to date. Assuming Milky Way ISM DM values from Cordes & Lazio (2003), a halo DM of $50\,\mathrm{pc\,cm^{-3}}$ (Prochaska & Zheng, 2019), and redshift-independent host galaxy contributions of $100\,\mathrm{pc\,cm^{-3}}$, the DM contributions from the IGM are expected to be 1480.8, 1052.8, and $1277.1\,\mathrm{pc\,cm^{-3}}$ respectively, which give Macquart-relation redshifts 1.58, 1.32, and 1.55 respectively(Macquart et al., 2020), assuming $H_0 = 70\,\mathrm{km\,s^{-1}\,Mpc^{-1}}$.

These FRBs are hence likely at the largest distances of the bursts in our sample, and therefore also the most luminous. Figure 5.3 plots polarisation fractions, |RM|, and boxcar widths vs structure-maximising DM for all the bursts in our sample; the three mentioned bursts stand out clearly from the rest of the sample.

These FRBs are narrow ($w_{\mathrm{box}} \lesssim 1\,\mathrm{ms}$ in all components; 20220610A has $\tau_{1\mathrm{GHz}} = 1.34 \pm 0.03\,\mathrm{ms}$), implying they have had very little scattering imposed by any turbulent medium along the path of travel.

FRBs 20210407E and 20220610A have high linear polarisation fractions, and the two components of 20210912A are only moderately circularly polarised to about an equal level to their linear polarisation. Following the scenario proposed by Sherman et al. (2024), we assume that all FRBs are highly linearly polarised at emission, and they undergo either conversion into circular polarisation or depolarisation throughout propagation from the source to Earth. Since we see no mechanism whereby distant FRBs would undergo less depolarisation during

propagation, and two of the three have low circular polarisation, we conclude that the dominant effect is scattering within the FRB host galaxy, which suppresses the scattering width by a factor of $(1+z)^3$, and suppresses depolarisation by $(1+z)^4$.

Finally, while FRBs 20210407E and 20210912A have small RMs, and 20220610A's is only moderate in magnitude, RM at the source is suppressed by $(1+z)^2$, which would make these FRBs (albeit with uncertain z) largely consistent with the rest of the distribution.

The extreme distance of these bursts makes it likely they represent the upper end of the FRB luminosity function (Ryder et al., 2023). Thus, selection effects (see e.g. Qiu et al., 2023) against wide bursts could potentially prevent these from being detected. However, these bursts each had moderate S/N at detection (19.1, 31.2, and 23.7 respectively, relative to the sample mean of 19.6 and the detection threshold of 10), suggesting that they would have still been detectable if they had been scattered within their host galaxies to a non-insignificant degree. Thus we conclude that such selection effects do not play an important role in our analysis.

The observed trend could also be suggestive of an evolving FRB population, in particular an evolving distribution of host environment properties, with bursts in the distant/earlier Universe being produced in more placid environments, but we make no strong conclusions or predictions, given the small number of bursts involved.

5.4.4 Correlation between small RM and high circular polarisation

Our sample is suggestive of a mutual exclusivity between larger-magnitude RMs and moderate-to-high circular polarisation fractions, plotted in Figure 5.4. All of the four components (between three FRBs) we observe with $|V|/I > 0.3$ have $|\mathrm{RM}| < 18\,\mathrm{rad\,m^{-2}}$ — phrased another way, none of the nine FRBs we observe with $|\mathrm{RM}| > 100\,\mathrm{rad\,m^{-2}}$ have $|V|/I > 0.2$. The sample reported by Sherman

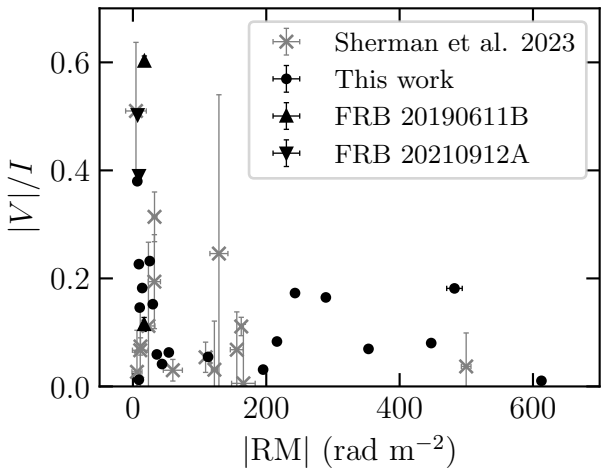

Figure 5.4: Absolute polarisation fraction vs absolute RM value in our sample and that of Sherman et al. (2024). One point from the latter, with $|\mathrm{RM}| = 4670.4 \pm 10.8\,\mathrm{rad\,m^{-2}}$and $|V|/I = 0.116 \pm 0.062$, has been cropped out for visual clarity.

et al. (2024), also plotted in Figure 5.4, is consistent with this observation, with the shape of their $|V|/I$-|RM| distribution taking approximately the same shape as ours, and adding a point to the low-|RM|, moderate-$|V|/I$ region.

We quantify the chances of this by assuming V/I and RM are uncorrelated, and calculating the probability that randomly assigning V/I to RM results in the three FRBs with highest V/I having $|\mathrm{RM}| < 18\,\mathrm{rad\,m^{-2}}$. Since 14 FRBs have $|\mathrm{RM}| > 18\,\mathrm{rad\,m^{-2}}$, this probability becomes $(8/22)(7/21)(6/20) \approx 0.0364$, which becomes 0.073 ($1.8\sigma$) when accounting for a two-sided test. Including DSA data, four FRBs have $V/I > 0.35$ but $|\mathrm{RM}| < 18\,\mathrm{rad\,m^{-2}}$, with a corresponding two-sided probability of 0.0088 (2.6σ). This number does not account for trial factors (we have not controlled for the number of possible correlations we have tested), nor the different time resolutions of DSA's and ASKAP's FRB samples, where a lower time resolution could result in apparent depolarisation.

Our result is only marginally significant, and requires a physical mechanism which increases RM, preserves linear polarisation, and reduces the degree of circular polarisation (or vice versa). Several repeating FRBs show anti-correlations between

the total degree of polarisaion and RM due to RM scatter (Feng et al., 2022), however many moderate-RM FRBs in this sample (the only high-RM FRB is DSA's FRB 20221101A, with an RM of 4670; Sherman et al., 2024) have high polarisation fractions (P/I > 0.8). A possibility is that these highly circular FRBs may have their polarization properties set in a purely e^+/e^- plasma, which induces no RM (Park & Blackman, 2010), but can produce circular polarization from linear (Lyutikov, 2022). For such systems to also have negligible RM contributed by surrounding material more distant from the FRB progenitor suggests that these systems have cleared their local environments, either through their own emissions, or through escaping their birthplace (e.g. through a kick ejecting them from their galaxy's ISM).

5.4.5 Microshots in FRB 20190711A

We note remarkably short-scale structures in FRB 20190711A (see the bottom two panels of the third page of Figure 5.1), the shortest and brightest of which is less than 50 µs in duration. This is paired with it being an overall broader FRB, with $w_{\rm box} = 8.8^{+0.6}_{-0.5}$ ms, among the largest in our sample.

Its dynamic spectrum is qualitatively similar to several bursts of FRB 20220912A as observed with the Nançay Radio Telescope (Hewitt et al., 2023), being composed of short-scale "microshots" and broader-scale emission exhibiting a frequency downdrift over the total duration of the burst. Hewitt et al. (2023) observe residual (post-dedispersion) frequency drifts of the broader components of FRB 20220912A's bursts of a few hundred MHz ms^{-1}. While we cannot confidently assert with the S/N of our data that we observe similar frequency drifting within a single component of FRB 20190711A, the broad emission before the first microshot is qualitatively consistent with this possibility.

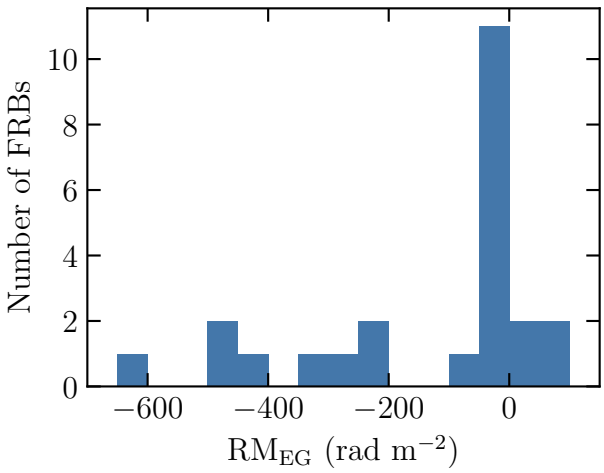

Figure 5.5: Histogram of the $\mathrm{RM_{EG}}$ values in our sample.

5.4.6 Excess of negative extragalactic rotation measures

Figure 5.5 shows the distribution of $\mathrm{RM_{EG}}$ measurements in our sample. We note an excess of negative values; 19 of the 24 $\mathrm{RM_{EG}}$ measurements are unambiguously negative. In the basic scenario where net positive and negative extragalactic RM contributions are equally likely, i.e the magnetic fields are not more likely to be oriented one way or the other along the path of propagation, the probability of observing 19 or more negative or positive values out of 24 measurements is 0.33% according to the binomial distribution, increasing to 0.66% allowing for a two-sided test.

Although we have already accounted for the expected Milky Way RM contribution by subtracting the $\mathrm{RM_{MW}}$ values corresponding to the FRB sightlines according to Hutschenreuter et al. (2022), we note that 16 of our 24 $\mathrm{RM_{EG}}$ measurements are between $-100\,\mathrm{rad\,m^{-2}}$ and $100\,\mathrm{rad\,m^{-2}}$, and 11 of these are between $-50\,\mathrm{rad\,m^{-2}}$ and $0\,\mathrm{rad\,m^{-2}}$. By conservatively estimating that $\mathrm{RM_{MW}}$ for our FRB sightlines, all of which are pointing out of the Galactic plane except FRB 20230718A, could feasibly vary so as to flip the signs of any of the measurements lying within the $\pm 100\,\mathrm{rad\,m^{-2}}$ range and therefore excluding them, we are left with 8 $\mathrm{RM_{EG}}$ measurements, all of which are negative. The probability of all

8 being signed one way or the other, again assuming net positive and negative extragalactic RM contributions are equally likely and following the binomial distribution, is 0.78 %.

This excess is potentially due to a large-scale asymmetry in the Galactic contribution to RM not yet accounted for in Milky Way RM models (Xu & Han, 2024). However, Sherman et al. (2024) present a comparable sample of FRB RM measurements, which does not appear to have an excess of negative or positive values, with 8 of the 20 reported values being negative (they do not subtract any Milky Way contribution from their reported values, so we assume that doing so would not dramatically alter the distribution of positive/negative RMs). Given this, we refrain from making any concrete conclusions about the origin of the negative RM excess.

5.5 Conclusions

We have presented high-time resolution polarimetric measurements of 21 FRBs, made possible by ASKAP's real-time burst detection and voltage capture capabilities. These bursts exhibit a wide range of burst morphologies and demonstrate complex short-duration structures likely present in many FRBs in the general population.

The analysis presented here is largely preliminary. The combination of high time resolution (in principle as fine as ~ 3 ns), high S/N due to coherent beamforming & summation between antennas, coherent dedispersion, and full polarimetry makes ASKAP FRB measurements promising for continued, detailed examination of burst properties.

Chapter 6

Investigating the Coherence of Fast Radio Burst Emission

Very little is concretely known about the emission mechanism or mechanisms producing FRBs. What can be concluded from FRB studies to date is that the emission process must be a coherent one, which is to say that the radiating charges producing the emission are radiating in phase with each other, rather than independently (Melrose, 2017). The primary indication of this is their brightness temperatures, the temperature that would be required to produce black-body radiation bright enough to produce burst fluences consistent with the distances to their source. The typical value of $T_K \approx 10^{35}\,\mathrm{K}$ far exceeds any thermal temperature known to be reached by physical processes, as well as the $10^{12}\,\mathrm{K}$ limit on the brightness temperature of synchrotron radiation set by inverse Compton scattering (Kellermann & Pauliny-Toth, 1969).

By starting from an assumption that the FRB emission process is coherent, we can expect that, in principle, the statistics of the radiation will reflect the emission process. This chapter details investigations into measuring the statistics and coherence of FRB emission using ASKAP data processed with CELEBI. It is intended as a collection of notes that may be used as a reference for further work in this area, and should be considered incomplete. The results here are not

a complete set of those produced during the investigation, but instead make up a summary of the investigations and methods.

The main aim of this chapter is to investigate the application of the second-order intensity correlation function to beamformed high-time resolution intensity time series of fast radio bursts obtained with ASKAP and processed by CELEBI. Because CELEBI's method for polyphase filterbank inversion gives close to perfect and artifact-free reconstructions of the original signal (Morrison et al., 2020), we should be able to confidently analyse the statistics of the data at the bandwidth-limited time resolution of $\delta t = (336\,\mathrm{MHz})^{-1} \approx 3\,\mathrm{ns}$.

Investigations into the use of the modified coherence function (Jenet et al., 2001; Smits et al., 2003) and the measurement of source noise would also be possible in principle, but are not pursued here. For an overview of models for coherent radiation mechanisms see Melrose (2017). Loudon (1980) and Dravins (2008) go over the measurement and interpretation of the non-classical properties of electromagnetic radiation. I also suggest taking note of models for radio emission from pulsars, specifically the amplitude modulated noise model (Rickett, 1975) and shot noise model (Cordes, 1976). These are potentially applicable to FRBs and include direct predictions on the statistics of the modeled radiation that could be used as tests of the models.

6.1 The second-order intensity correlation function

The specific mechanisms of astrophysical phenomena produce measurable imprints in their signals. The most commonly observed of these are intensity, spectra, spatial extent and shape, as well as the variation of each of these over time. These quantities are measurable by simply capturing electromagnetic radiation over a certain time window. This is akin to catching water in a bucket, and after an hour measuring how much water has been collected, and perhaps some other collective

properties of the water such as its temperature.

However, there is only so much information about a signal's emission mechanism we can glean from these basic observables. Identical intensities, spectra, and spatial extents may be producible from many entirely different physical processes. Fortunately, there is more to electromagnetic radiation than how much of it there is and what wavelengths it contains; we can also consider the second- (or higher) order coherence of the radiation, measurable in the correlations in arrival times of two (or more) photons (Dravins, 2008). To return to the earlier analogy, we could measure the correlation in the arrival time of each water drop with the next over the hour we had placed the bucket outside. If the drops came irregularly and randomly, we might think that to be consistent with the stochastic nature of natural rainfall. But if the drops came at a constant rate with little to no deviation, we might consider if a different process was producing the water, such as a tap dripping at a constant rate. If the only information we had was the volume and temperature of the water in the bucket, these two scenarios could be indistinguishable.

At radio frequencies, electromagnetic radiation is typically considered in the wave regime, rather than as a stream of photons. Indeed, it would require extraordinary time resolution and signal-to-noise to observe the individual arrivals of the many low-energy photons making up low-frequency radiation. However, inferences can be made in principle of the second-order coherence of the radiation from its statistics measured at sufficiently fine time resolution, even if that time resolution is not enough to identify individual photon arrivals. This can be done with the second-order correlation function of the radiation's time-dependent intensity $I(t)$:

$$g^{(2)}(\tau) = \frac{\langle I(t)I(t+\tau)\rangle}{\langle I(t)\rangle^2}, \tag{6.1}$$

where τ is the correlation time delay and the angled brackets indicate averaging over a time period larger than the time resolution of $I(t)$ (Dravins, 2008).

$g^{(2)}(\tau)$ is the quantity measured by an intensity interferometer, which Han-

bury Brown & Twiss (1956a) used in a laboratory environment to demonstrate that a measurement of the second-order coherence of radiation is possible. They would go on to apply this to measure the angular diameter of Sirius, demonstrating the applicability of the concept to astronomical sources (Hanbury Brown & Twiss, 1956b).

$g^{(2)}(\tau)$ takes on different values for different collective properties of photons. A steady stream where each photon is evenly separated from the next, as is produced by an idealised laser, gives $g^{(2)}(\tau) = g^{(2)}(0) = 1$. Chaotic radiation, such as blackbody radiation, has a "bunched" photon stream, meaning photons tend to arrive close in time to each other, and gives $g^{(2)}(0) = 2$. We can typically consider radiation to fall somewhere between the "coherent" ($g^{(2)}(0) = 1$) and "incoherent" ($g^{(2)}(0) = 2$) regimes, although there are physical processes that can give rise to values of $g^{(2)}(0)$ outside of this range (Dravins, 2008).

What we have in $g^{(2)}(0)$ is a measure of the distribution of photons within radiation without requiring sufficient time resolution to identify the arrivals of single photons. This makes such a measurement potentially viable at radio wavelengths. $g^{(2)}(0)$ could therefore be used to measure the degree of coherence of FRB emission.

6.1.1 Expected impact of dispersion

The frequency-dependent arrival time due to dispersion manifests in single-channel time series data as smearing of signal over many adjacent time bins, unless dedispersion has been applied with a precision sufficient to ensure the arrival time of emission at the top and bottom of the observing band is separated by no more than the time resolution of the data. When this time resolution is on the order of microseconds, this typically means identifying a DM to $\sim 10^{-4}\,\mathrm{pc\,cm^{-3}}$ precision at most.

However, when our aim is to use the statistics at the bandwidth-limited time resolution of $\sim 3\,\mathrm{ns}$ we need to go even further. To estimate the required precision,

we can calculate the DM that would separate the emission arrival times by exactly one bin of width δt. Approximating the ASKAP centre frequency as 1 GHz and using the bandwidth of 336 MHz, the frequencies of the bottom and top of the band are $\nu_1 = 0.832\,\mathrm{GHz}$ and $\nu_2 = 1.168\,\mathrm{GHz}$ respectively. Setting the dispersion constant[1] $k_{\mathrm{DM}} = 2.41 \times 10^{-4}\,\mathrm{pc\,cm^{-3}\,GHz^{-2}\,\mu s^{-2}}$, we get:

$$\delta\mathrm{DM} = \frac{\delta t k_{\mathrm{DM}}}{\nu_1^{-2} - \nu_2^{-2}} \tag{6.2}$$

$$\approx 10^{-6}\,\mathrm{pc\,cm^{-3}}. \tag{6.3}$$

It is worth making a distinction here between *structure* and *coherence* within a signal. DM measurement methods based on optimising for signal-to-noise or structure in an FRB will be fundamentally limited by the minimal timescale of intrinsic structure within the burst. As such, unless a burst has intrinsic structure on a 3 ns timescale, it would be both impossible and unnecessary to measure its DM to a precision of $10^{-6}\,\mathrm{pc\,cm^{-3}}$. However, even if the structure of a burst has been resolved by dedispersion, it could still be the case that the electric field measurement within that structure is smeared across adjacent 3 ns-duration time bins, apparently decohering the signal. In order to measure the coherence, it would therefore still be necessary to get the DM correct to within $10^{-6}\,\mathrm{pc\,cm^{-3}}$, regardless of the timescales of any structures intrinsic to the burst.

6.1.2 Expected impact of scattering

Much like dispersion, scattering will have the effect of smearing signal across time bins. Unlike dispersion, it isn't possible to reverse this process. Therefore the more scattering present in an FRB signal, the more inherently smeared its data will be, and the lower the prospects for coherent statistics to have been preserved in the data. Because of this, when investigating coherence, it is ideal to use an

[1] This value of k_{DM} is not the most precise or accurate value known. However, it continues to be used due to the requirements of pulsar timing for consistent methods of DM measurement over many years (Hobbs et al., 2006).

FRB that has a minimal degree of scattering present.

While the scattering timescales for FRBs are significantly larger than the time resolution of our data and the timescale associated with the desired DM precision ($10^{-6}\,\mathrm{pc\,cm^{-3}}$), it should still be possible in principle to carry out a measurement of coherence within FRBs with large enough S/N and small enough scattering. At present, it is unclear precisely what impact scattering will have on the measurement of coherence, and therefore it is also unclear how much scattering is required to destroy the signal of coherence in an FRB. Assuming there is coherent emission intrinsic to FRBs, and considering ASKAP's ability to produce *coherently summed* data at the 3 ns level with S/N ratios in the hundreds, it is reasonable to expect that the signal of a coherent emission mechanism could shine through.

6.2 Applying the second-order intensity correlation function to FRB 20181112A

The basic principle of this investigation is to make a prediction for the value of $g^{(2)}(0)$ for *incoherent*, partially polarised radiation (IPPR; $g^{(2)}_{\mathrm{IPPR}}(0)$), and compare this to the actual value of $g^{(2)}(0)$ measured directly from FRB data ($g^{(2)}_{\mathrm{FRB}}(0)$). Throughout, I will be using the maximum time resolution of $\delta t = (336\,\mathrm{MHz})^{-1} \approx 3\,\mathrm{ns}$ for our data, and calculating the expectations over bins of some longer time resolution t_{avg} (which is an integer multiple of δt) under the assumption of an emission process intrinsically stationary over a timescale of t_{avg}. These expectations (indicated by angled brackets) will be direct averages unless otherwise specified. To be explicit, the expectation of a quantity $Z(t)$ measured at a time resolution of δt in the ith bin of duration t_{avg} is

$$\langle Z \rangle_i = \frac{\delta t}{t_{\mathrm{avg}}} \sum_{t=it_{\mathrm{avg}}}^{(i+1)t_{\mathrm{avg}}} Z(t). \tag{6.4}$$

The reference prediction of $g^{(2)}(0)$ for IPPR is

$$g^{(2)}_{\mathrm{IPPR}}(0) = 1.5 + 0.5p^2, \tag{6.5}$$

(Sutinjo, private communication; see Appendix B) where p is the total polarisation fraction

$$p = \frac{\sqrt{Q^2 + U^2 + V^2}}{I}. \tag{6.6}$$

We can calculate $g^{(2)}_{\mathrm{FRB}}(0)$ directly from an FRB's high-time resolution Stokes I time series by

$$g^{(2)}_{\mathrm{FRB}}(0) = \frac{\langle I^2 \rangle}{\langle I \rangle^2}, \tag{6.7}$$

We expect that the $g^{(2)}_{\mathrm{FRB}}(0)$ measured from FRB data will be less than $g^{(2)}_{\mathrm{IPPR}}(0)$, as a smaller $g^{(2)}(0)$ corresponds to a higher degree of coherence.

A straightforward starting point is to take data for an FRB that has been dedispersed to its structure-maximising DM, as determined by the method of Sutinjo et al. (2023). The guiding criteria used for choosing an FRB to work with are:

- High signal-to-noise.
- Minimal apparent scattering, due to the potential for scattering to smear out the statistics of an FRB and "decohere" it.
- Non-negligible polarisation, since our prediction is based on an assumption of partially polarised radiation.

For this investigation, I use FRB 20181112A, as it comfortably meets all of these criteria.

When choosing t_{avg} we want a value large enough to give good signal-to-noise in each bin, but not so large that the burst profile varies rapidly over the bin duration. Since the numerator of $g^{(2)}(0)$ is proportional to the profile's variance (see Appendix B, eq B.8), a t_{avg} that gives a rapidly varying profile within bins will inflate the measured $g^{(2)}(0)$ and render it meaningless.

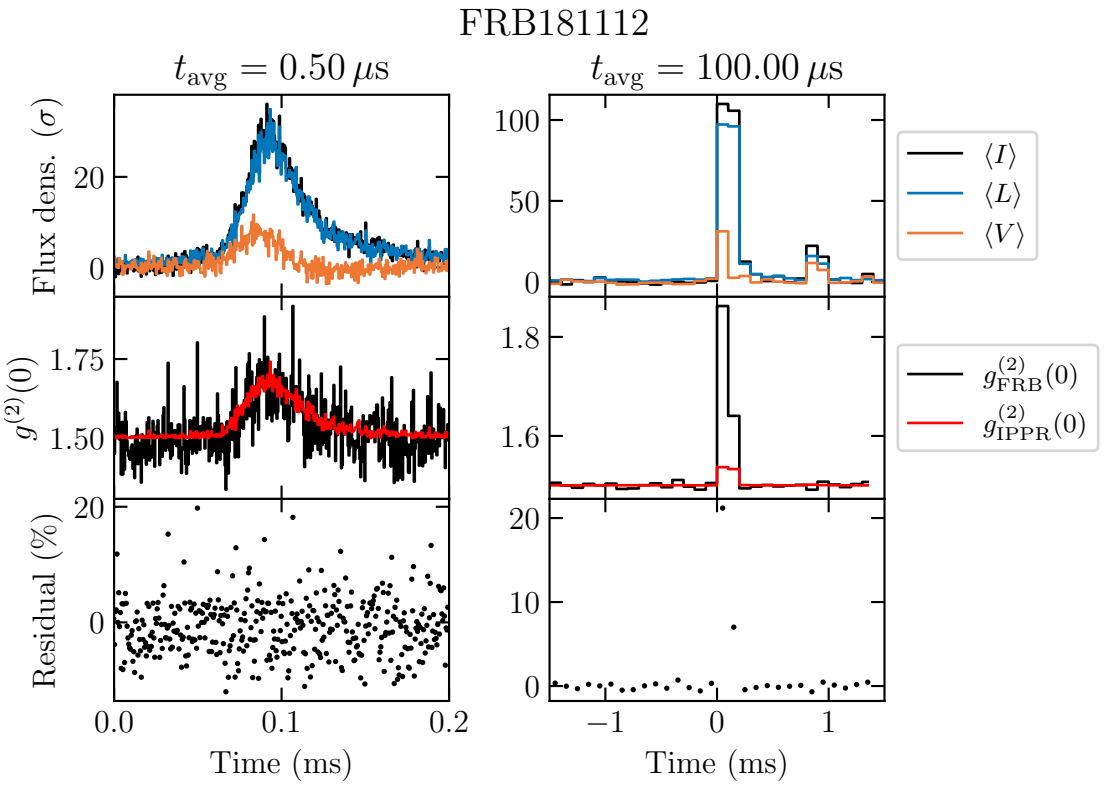

Figure 6.1: Simple comparison between $g^{(2)}_{\rm FRB}(0)$ and $g^{(2)}_{\rm IPPR}(0)$ for FRB 20181112A, with $t_{\rm avg} = 0.5\,\mu$s (left) and $t_{\rm avg} = 100\,\mu$s (right). Top row: $\langle I \rangle$ of FRB 20181112A, along with $\langle L \rangle$ and $\langle V \rangle$ to give an indication of the polarisation present in the burst. Second row: $g^{(2)}_{\rm FRB}(0)$ (black) and $g^{(2)}_{\rm IPPR}(0)$ (red). Bottom row: residuals $(g^{(2)}_{\rm FRB}(0) - g^{(2)}_{\rm IPPR}(0))$ as percentages of $g^{(2)}_{\rm IPPR}(0)$.

A simple algorithm to make the comparison between $g^{(2)}_{\rm FRB}(0)$ and $g^{(2)}_{\rm IPPR}(0)$ is as follows:

for $i = 0, \ldots, \dfrac{t_{\rm avg}}{\delta t} - 1$ **do**
  $g^{(2)}_{\rm FRB}(0)_i \leftarrow \dfrac{\langle I^2 \rangle_i}{\langle I \rangle_i^2}$
  $p_i \leftarrow \dfrac{\sqrt{\langle Q \rangle_i^2 + \langle U \rangle_i^2 + \langle V \rangle_i^2}}{\langle I \rangle_i}$
  $g^{(2)}_{\rm IPPR}(0)_i \leftarrow 1.5 + 0.5 p_i^2$
end for

The results of this algorithm for FRB 20181112A with $t_{\rm avg} = 0.5\,\mu$s and $t_{\rm avg} = 100\,\mu$s are shown in Figure 6.1.

The second column of Figure 6.1 demonstrates the inflation of $g^{(2)}(0)$ when t_{avg} is chosen to be too large, here at 100 µs. With this t_{avg}, the primary burst's profile is almost entirely contained in only two bins. Noting that the profile in the first column is plotted over a duration of 200 µs, we can see that the profile within each of the 100 µs bins of the second column will be entirely non-stationary. With $t_{\text{avg}} = 0.5$ µs, we see no such inflation, as the profile is slowly-varying in each of the bins.

The left column of Figure 6.1 shows no notable deviation between $g^{(2)}_{\text{FRB}}(0)$ and $g^{(2)}_{\text{IPPR}}(0)$ for $t_{\text{avg}} = 0.5$ µs. In particular, we do not see any outliers or excess of negative residuals, corresponding to $g^{(2)}_{\text{FRB}}(0) < g^{(2)}_{\text{IPPR}}(0)$, which would imply a higher measured degree of coherence than the incoherent prediction. There is a slight excess of positive residuals (i.e. $g^{(2)}_{\text{FRB}}(0) > g^{(2)}_{\text{IPPR}}(0)$, which implies a lower degree of coherence than the prediction), but this seems unrelated to the FRB itself, as the excess is present even when the FRB signal is weak or off.

For the rest of this investigation, I use 0.5 µs and 10 µs as values of t_{avg}, so the effect of changing t_{avg} can be considered.

6.2.1 Measuring $g^{(2)}(0)$ over a range of DMs

As described in §6.1.1, dispersion will cause a smearing of signal across adjacent ~ 3 ns bins unless the signal has been dedispersed to the correct DM within $\sim 10^{-6}$ pc cm^{-3}. Analysing data dedispersed to this DM will give the best chance at observing coherence within an FRB, as the corruption of the statistics due to dispersion will be minimised.

Optimising for burst signal-to-noise or structure is not able to identify a DM to this precision, so here I measure $g^{(2)}_{\text{FRB}}(0)$ and compare it to $g^{(2)}_{\text{IPPR}}(0)$ over a range of DMs using coherent dedispersion.

The following algorithm calculates $g^{(2)}_{\text{FRB}}(0)$ and $g^{(2)}_{\text{IPPR}}(0)$ over both time (indexed by i) and ΔDM (indexed by j, defined such that $\Delta\text{DM} = 0$ at the structure-optimising DM). Dedispersion is done coherently by multiplying the X and Y fine

spectra by dedispersion phases:

$$\phi(f;\mathrm{DM}) = \exp\left(2i\pi\frac{\mathrm{DM}}{k_{\mathrm{DM}}}\left(\frac{(f-f_{\mathrm{ref}})^2}{f_{\mathrm{ref}}^2 f}\right)\right), \tag{6.8}$$

(Hankins, 1971) where f_{ref} is some reference frequency. In this chapter, I take f_{ref} to be the central frequency of the data bandwidth.

The algorithm makes use of the distributive property of coherent dedispersion (that is, dedispersing by some DM twice is equivalent to dedispersing by 2DM once) to minimise the calculation of $\phi(f;\mathrm{DM})$, which can be computationally expensive. The $X(t)$ and $Y(t)$ data are initialised by dedispersing them to the first ΔDM, and are then dedispersed by the same small step for each subsequent ΔDM.

1: Define a range of evenly-spaced ΔDM values, from $\Delta\mathrm{DM}_{\mathrm{min}}$ to $\Delta\mathrm{DM}_{\mathrm{max}}$, separated by δDM, for a total of n_{DM} values.
2: Calculate $\phi(f;\Delta\mathrm{DM}_{\mathrm{min}})$ and $\phi(f;\delta\mathrm{DM})$ by eq 6.8
3: ▷ *Initialise X and Y by dedispersing to $\Delta\mathrm{DM}_{\mathrm{min}}$* ◁
4: $X(t)_{j=0} \leftarrow \mathcal{F}^{-1}\Big(\mathcal{F}\big(X(t)\big)\phi(f,\Delta\mathrm{DM}_{\mathrm{min}})\Big)$
5: $Y(t)_{j=0} \leftarrow \mathcal{F}^{-1}\Big(\mathcal{F}\big(Y(t)\big)\phi(f,\Delta\mathrm{DM}_{\mathrm{min}})\Big)$
6: **for** $j = 0,\ldots,n_{\mathrm{DM}}-1$ **do**
7: $\quad I(t)_j \leftarrow |X(t)_j|^2 + |Y(t)_j|^2$
8: $\quad Q(t)_j \leftarrow |X(t)_j|^2 - |Y(t)_j|^2$
9: $\quad U(t)_j \leftarrow 2\,\mathrm{Re}\,(X(t)_j Y^*(t)_j)$
10: $\quad V(t)_j \leftarrow 2\,\mathrm{Im}\,(X(t)_j Y^*(t)_j)$
11: $\quad$ **for** $i = 0,\ldots,\dfrac{t_{\mathrm{avg}}}{\delta t}-1$ **do**
12: $\quad\quad g^{(2)}_{\mathrm{FRB}}(0)_{i,j} \leftarrow \dfrac{\langle I_j^2\rangle_i}{\langle I_j\rangle_i^2}$
13: $\quad\quad p_{i,j} \leftarrow \dfrac{\sqrt{\langle Q_j\rangle_i^2 + \langle U_j\rangle_i^2 + \langle V_j\rangle_i^2}}{\langle I_j\rangle_i}$
14: $\quad\quad g^{(2)}_{\mathrm{IPPR}}(0)_{i,j} \leftarrow 1.5 + 0.5p_{i,j}^2$
15: $\quad$ **end for**

16: ▷ *Increment dedispersion* ◁

17: $X(t)_{j+1} \leftarrow \mathcal{F}^{-1}\Big(\mathcal{F}\big(X(t)_j\big)\phi(f;\delta\mathrm{DM})\Big)$

18: $Y(t)_{j+1} \leftarrow \mathcal{F}^{-1}\Big(\mathcal{F}\big(Y(t)_j\big)\phi(f;\delta\mathrm{DM})\Big)$

19: **end for**

For this investigation with FRB 20181112A, I set $\Delta\mathrm{DM}_{\mathrm{min}} = -0.006\,\mathrm{pc\,cm^{-3}}$ and $\Delta\mathrm{DM}_{\mathrm{max}} = 0.009\,\mathrm{pc\,cm^{-3}}$ to match the uncertainty bounds on the structure-maximising DM as found by Sutinjo et. al (2023).

Figure 6.2 demonstrates a comparison between $g^{(2)}_{\mathrm{FRB}}(0)$ and $g^{(2)}_{\mathrm{IPPR}}(0)$ for FRB 20181112A with $\delta\mathrm{DM} = 2 \times 10^{-4}\,\mathrm{pc\,cm^{-3}}$. This δDM is two orders of magnitude greater than the expected DM precision required to eliminate dispersive smearing over 3 ns time samples of $10^{-6}\,\mathrm{pc\,cm^{-3}}$, as such a small δDM would produce detail far too fine to examine in the plots of Figure 6.2.

Figure 6.3 shows histograms of the residuals of a comparison between $g^{(2)}_{\mathrm{FRB}}(0)$ and $g^{(2)}_{\mathrm{IPPR}}(0)$ for FRB 20181112A over the same DM range and t_{avg} values, but for $\delta\mathrm{DM} = 10^{-6}$, to meet the precision requirement for eliminating dispersive smearing, and best fits of skew-normal distributions. Note that this doesn't tell us *which* DM eliminates smearing, but we should expect that *at least one* of the DMs in this range does. The idea is that this DM will produce an intensity profile with statistics uncorrupted by dispersion, thus giving the best chance at measuring coherence.

As with the residuals in Figure 6.1, we can see in Figure 6.3 an excess of positive residuals, which is particularly pronounced for $t_{\mathrm{avg}} = 0.5\,\mu\mathrm{s}$. The histograms show more clearly that this excess is not due to outliers, but rather that the distribution of residuals is skewed towards positive values. The bulk of the distributions are reasonably well-described by skew-normal distributions, but it is unclear why this should be the case.

It is clear from Figure 6.3 that there are no negative outlier residuals, the presence of which would have indicated a possible direct measurement of FRB coherence. Interestingly, the mean of both samples of residuals is slightly negative

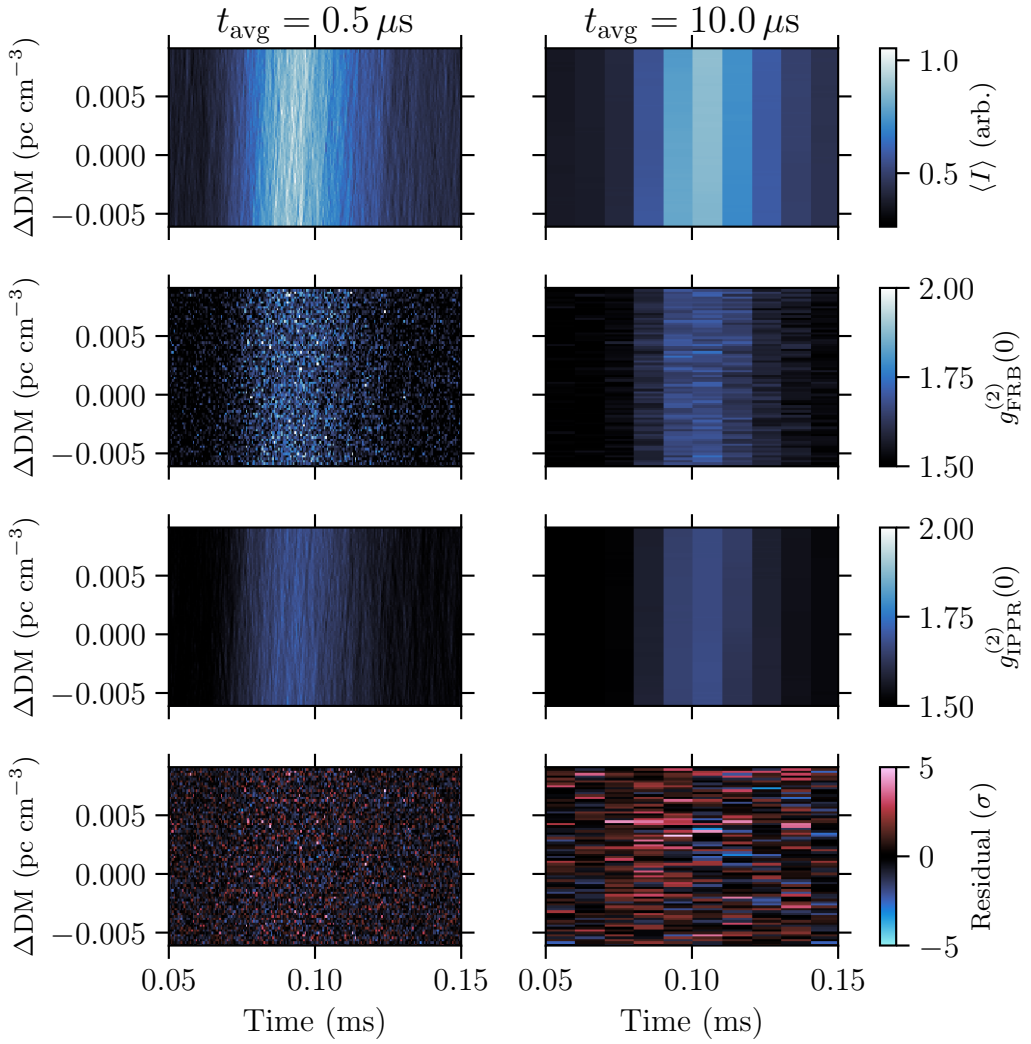

Figure 6.2: Comparison of $g^{(2)}_{\mathrm{FRB}}(0)$ and $g^{(2)}_{\mathrm{IPPR}}(0)$ for FRB 20181112A with $\delta\mathrm{DM} = 2 \times 10^{-4}\,\mathrm{pc\,cm^{-3}}$ with $t_{\mathrm{avg}} = 0.5\,\mu\mathrm{s}$ (left) and $t_{\mathrm{avg}} = 10\,\mu\mathrm{s}$ (right). Top row: $\langle I \rangle$. Second row: $g^{(2)}_{\mathrm{FRB}}(0)$. Third row: $g^{(2)}_{\mathrm{IPPR}}(0)$. Fourth row: residuals ($g^{(2)}_{\mathrm{FRB}}(0) - g^{(2)}_{\mathrm{IPPR}}(0)$) in units of standard deviations.

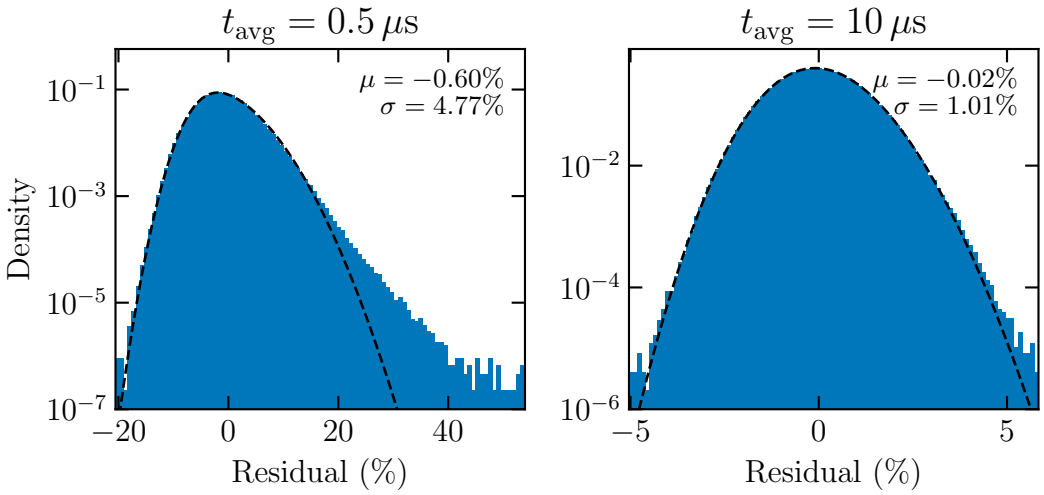

Figure 6.3: Histograms of the residuals of comparisons between $g^{(2)}_{\mathrm{FRB}}(0)$ and $g^{(2)}_{\mathrm{IPPR}}(0)$ with $\delta\mathrm{DM} = 10^{-6}\,\mathrm{pc\,cm^{-3}}$, for $t_{\mathrm{avg}} = 0.5\,\mu\mathrm{s}$ (left) and $t_{\mathrm{avg}} = 10\mu\mathrm{s}$ (right). Inset text in each plot is the mean μ and standard deviation σ of each sample of residuals. Dashed lines are best fits of the probability density functions of skew-normal distributions.

(-0.60% for $t_{\mathrm{avg}} = 0.5\,\mu\mathrm{s}$, -0.02% for $t_{\mathrm{avg}} = 10\,\mu\mathrm{s}$), hinting that over all the DMs and time bins the average degree of coherence is slightly higher than the IPPR prediction. However, since the standard deviation of each sample (4.77% and 1.01% respectively) is much larger than the magnitude of the respective means, it would be difficult to draw any concrete conclusions from this without a better understanding of the distributions of these residuals.

6.2.2 Smoothing by regularisation instead of direct averaging

Until now, I have been using a direct average of the 3 ns resolution burst profile for our expectations. In effect, this has been treating the expectations as approximations of the true burst profile measured on some timescale t_{avg}, in the sense that the averaging is suppressing the noise of our data to bring us closer to the underlying true profile.

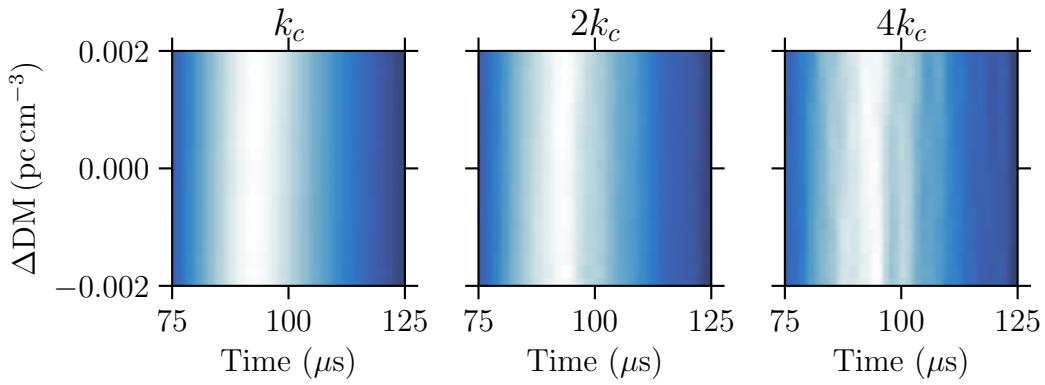

Figure 6.4: $\langle \tilde{I} \rangle$ profiles over time and ΔDM for changing multiplicative factors applied to k_c (left to right: 1, 2, 4).

Now I consider smoothing by regularisation as an alternative method of approximating the true burst profile. I use the smoothing method developed by Sutinjo et al. (2023), where it was applied to determine the dedispersion DM that optimises structure in the burst profile and an associated uncertainty. To summarise, we smooth $I(t)$ by applying a low-pass filter with a spectral cutoff k_c. This gives us a smoothed "model" profile $\tilde{I}(t)$.

Sutinjo et al. (2023) were particularly concerned with optimising an FRB's DM for structure in the burst profile, and choose k_c by minimising the error in the structure-optimised DM. However, for the method here where I am less concerned with robustly optimising the burst DM as I am with trying to obtain an approximation of the burst profile, there is some flexibility.

Throughout this section, I will also investigate the effect of increasing k_c by multiplying it by a factor of 2 and 4. Increasing k_c will increase the fidelity of the resulting smoothed profiles, as is demonstrated in Figure 6.4. This fidelity will include a combination of real burst signal and noise, with the idea being to attempt to fine-tune the trade-off between smoothing out noise and smoothing out the real signal.

In the implementation applied here, I first time-scrunch $I(t)$ to 1 µs before finding $\tilde{I}(t)$, and then linearly interpolate $\tilde{I}(t)$ back to the initial ~ 3 ns time

resolution. This is to reduce the computational demand of the algorithm, and is safe to do without significant loss of information as, for FRB 20181112A, the timescale of the smoothing is substantially greater than 1 µs. I then calculate $g^{(2)}_{\mathrm{FRB}}(0)$ by:

$$g^{(2)}_{\mathrm{FRB}}(0) = \frac{\langle I^2 \rangle}{\langle \tilde{I} \rangle^2}, \tag{6.9}$$

It is important to note that this process is only applied to $I(t)$ (in the denominator of $g^{(2)}(0)$), *not* $I(t)^2$ (in the numerator of $g^{(2)}(0)$). This means that the high-time resolution statistics of the burst profile are not removed from the analysis. Also, I still calculate p with the original $I(t)$, so $g^{(2)}_{\mathrm{IPPR}}(0)$ will not be different. The algorithm for this method is identical to that used in the previous section, aside from replacing the calculation of $g^{(2)}_{\mathrm{FRB}}(0)$ by eq 6.9.

Figure 6.5 shows the $g^{(2)}_{\mathrm{FRB}}(0) - g^{(2)}_{\mathrm{IPPR}}(0)$ residuals over time and ΔDM across t_{avg} and spectral cutoffs. Figure 6.6 shows the overall distributions of these residuals, as well as the distribution of residuals from the direct averaging method for comparison.

For $t_{\mathrm{avg}} = 0.5\,\mu\mathrm{s}$, there is very little difference in the results for different spectral cutoffs. In all cases, the residuals are distributed much more broadly than for the direct method, and there are no extreme negative outliers. For $t_{\mathrm{avg}} = 10\,\mu\mathrm{s}$, the distributions are much closer to the direct method, and get noticeably closer as the spectral cutoff is increased. The top-right panel of Figure 6.5 (with $t_{\mathrm{avg}} = 10\,\mu\mathrm{s}$ and spectral cutoff k_c) suggests some possible structure in the residuals correlated with the underlying burst profile, with the rise and fall times of the burst correlated with excess negative residuals, and the flat constant top of the burst correlated with excess positive residuals. The reasons for this are unclear, and given that a spectral cutoff of k_c also gives the broadest (i.e. least precise) distribution of residuals, there seems to be reason to see k_c as too low a spectral cutoff in this method.

Overall, the regularisation method seems to have the effect of making the comparison between $g^{(2)}_{\mathrm{FRB}}(0)$ and $g^{(2)}_{\mathrm{IPPR}}(0)$ less precise, especially for small t_{avg}. It

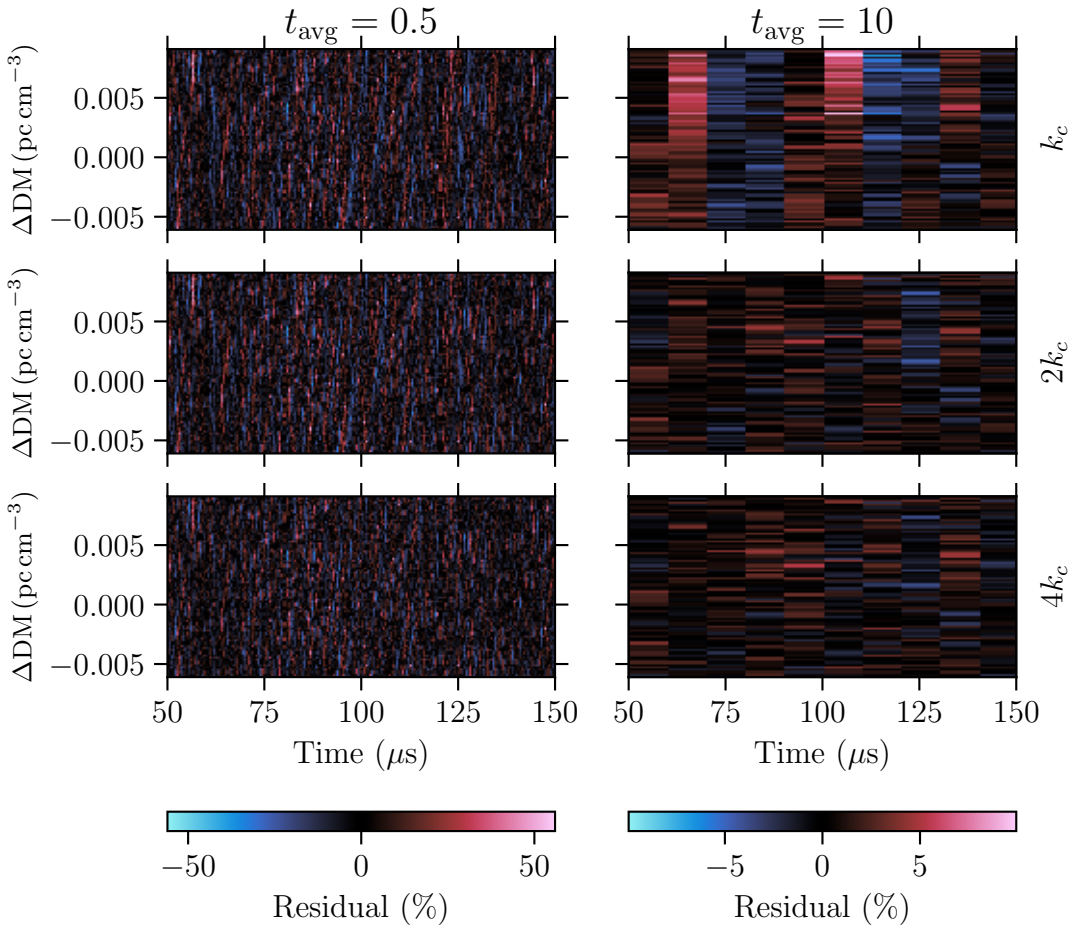

Figure 6.5: $g^{(2)}_{\mathrm{FRB}}(0) - g^{(2)}_{\mathrm{IPPR}}(0)$ residuals over time and ΔDM, where $g^{(2)}_{\mathrm{FRB}}(0)$ has been calculated with the regularisation method with $\delta\mathrm{DM} = 2 \times 10^{-4}$, $t_{\mathrm{avg}} = 0.5\,\mu\mathrm{s}$ (left) and $t_{\mathrm{avg}} = 10\,\mu\mathrm{s}$ (right), and spectral cutoffs k_c, $2k_c$, and $4k_c$ (from top to bottom).

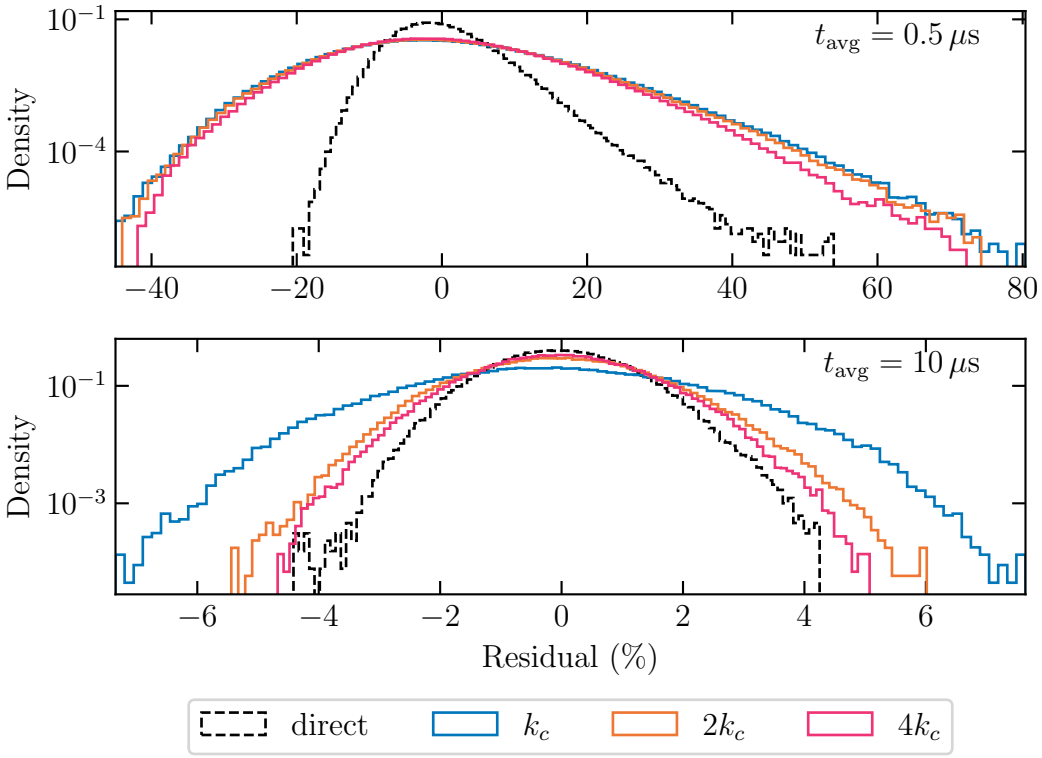

Figure 6.6: Distributions of $g^{(2)}_{\mathrm{FRB}}(0) - g^{(2)}_{\mathrm{IPPR}}(0)$ residuals where $g^{(2)}_{\mathrm{FRB}}(0)$ has been calculated with the regularisation method with $\delta\mathrm{DM} = 10^{-6}$, $t_{\mathrm{avg}} = 0.5\,\mu\mathrm{s}$ (top) and $t_{\mathrm{avg}} = 10\,\mu\mathrm{s}$ (bottom), and for spectral cutoffs k_c, $2k_c$, and $4k_c$. The distributions of residuals from the direct averaging method are also shown for comparison.

could have some application for larger $t_{\rm avg}$, so long as the spectral cutoff is high enough. More investigation is required to say conclusively if the regularisation method is useful in searching for coherence, or if simple direct averaging is best.

6.3 Measuring $g^{(2)}(0)$ in synthetic bursts with varying polarisation fraction

In this section, I apply $g^{(2)}(0)$ to pure-noise synthetic bursts — i.e. purely incoherent signals — to verify that the resulting $g^{(2)}_{\rm synth}(0)$ values are consistent with the IPPR prediction. I generate the complex X and Y time series of the synthetic bursts by summing a pure white noise component with a "signal" component, which is white noise modulated by a Gaussian time profile of similar timescale to FRB 20181112A:

$$X_{\rm synth}(t) = X_{\rm re,ns}(t) + iX_{\rm im,ns}(t) + s\left(X_{\rm re,sig}(t) + iX_{\rm im,sig}(t)\right), \tag{6.10}$$

$$Y_{\rm synth}(t) = Y_{\rm re,ns}(t) + iY_{\rm im,ns}(t) + sp\left(Y_{\rm re,sig}(t) + iY_{\rm im,sig}(t)\right), \tag{6.11}$$

where:

- Subscript "ns" denotes the noise component.
- Subscript "sig" denotes the signal component.
- Subscripts "re" and "im" denote real and imaginary components respectively.
- $X_{\rm re,ns}(t)$, $X_{\rm im,ns}(t)$, $Y_{\rm re,ns}(t)$, $Y_{\rm im,ns}(t)$ are all i.i.d. $\sim \mathcal{N}(0,1)$.
- $X_{\rm re,sig}(t)$, $X_{\rm im,sig}(t)$, $Y_{\rm re,sig}(t)$, $Y_{\rm im,sig}(t)$ are all i.i.d. $\sim \mathcal{N}(0,1)$, and then modulated by a Gaussian time profile with width comparable to FRB 20181112A.
- p is the desired polarisation fraction of the combined signal.

- s is a scaling factor, set so that the resulting $I(t)$ profile has a large signal-to-noise consistent across values of p.

I generate five instances each of $X_{\text{synth}}(t)$ and $Y_{\text{synth}}(t)$ for each of $p = 0$, 0.5, 1, and feed this data into the algorithm in §6.2.1, keeping DM_{min} and DM_{max} at the values used when analysing FRB 20181112A so comparisons can be made between the real and synthetic bursts. Figure 6.7 shows an example of $\langle I \rangle$ for one of these synthetic bursts.

Figure 6.8 shows the $g^{(2)}_{\text{synth}}(0) - g^{(2)}_{\text{IPPR}}(0)$ residuals over time and ΔDM across t_{avg} and p values, averaged across the five different instances of noise. Figure 6.9 shows the distributions across all five noise instances over each of $p = 0$, 0.5, 1 with $\delta\text{DM} = 10^{-5}\,\text{pc}\,\text{cm}^{-3}$.

It is clear from Figures 6.8 and 6.9 that there is a large excess of positive residuals when $t_{\text{avg}} = 10\,\mu\text{s}$, correlated with time bins containing the rise and fall of the synthetic bursts (as seen when comparing to Figure 6.7). This is consistent with the "inflation" of $g^{(2)}(0)$ demonstrated in Figure 6.1, indicating that $t_{\text{avg}} = 10\,\mu\text{s}$ is still long enough to produce inflated residuals. However, this effect will only apply to the time bins where the underlying burst is changing rapidly, and the two central time bins where the signal is on average constant don't manifest any of this inflation. This does indicate that $t_{\text{avg}} = 10\,\mu\text{s}$ could be too long a time binning to expect to be useful.

The top panel of Figure 6.9 shows that the distribution of residuals in the synthetic data for $t_{\text{avg}} = 0.5\,\mu\text{s}$ and $p = 0.5$ is almost identical to the distributions of the residuals in the real FRB 20181112A data. This is reassuring, as it confirms that the synthetic noise simulation is able to produce results consistent with reality and confirms that $g^{(2)}_{\text{IPPR}}(0)$ is a valid prediction for incoherent, partially polarised radiation. It also reinforces that the measurements of $g^{(2)}(0)$ for FRB 20181112A are consistent with an incoherent signal.

The shape of the $t_{\text{avg}} = 0.5\,\mu\text{s}$ residual distributions changes with p, becoming more spread out as p goes from 0 to 1. Despite only being a slight effect, it does

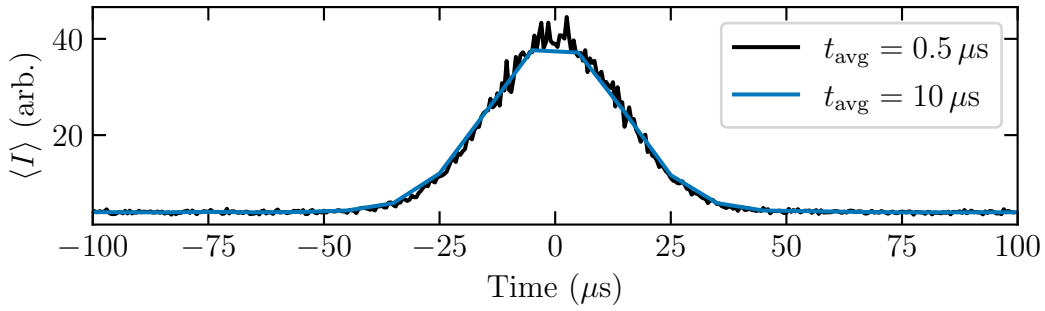

Figure 6.7: $\langle I \rangle$ of a synthetic burst for $t_{avg} = 0.5\,\mu s$ and $t_{avg} = 10\,\mu s$.

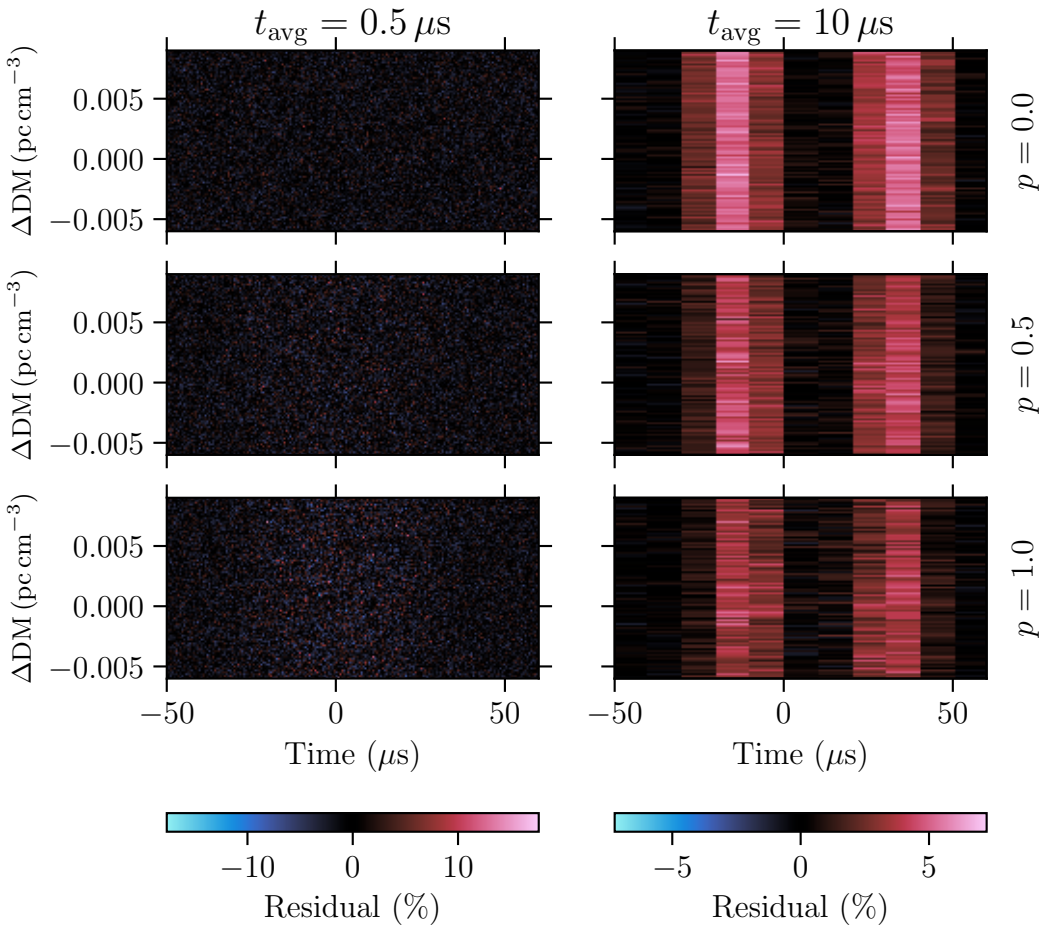

Figure 6.8: $g^{(2)}_{synth}(0) - g^{(2)}_{IPPR}(0)$ residuals over time and ΔDM, calculated from pure-noise data with varying polarisation fraction, with $\delta\text{DM} = 2 \times 10^{-4}, \text{pc cm}^{-3}$, $t_{avg} = 0.5\,\mu s$ (left) and $t_{avg} = 10\,\mu s$ (right), and $p = 0$, 0.5, 1 (top to bottom). These residuals have been averaged over five instances of pure-noise data.

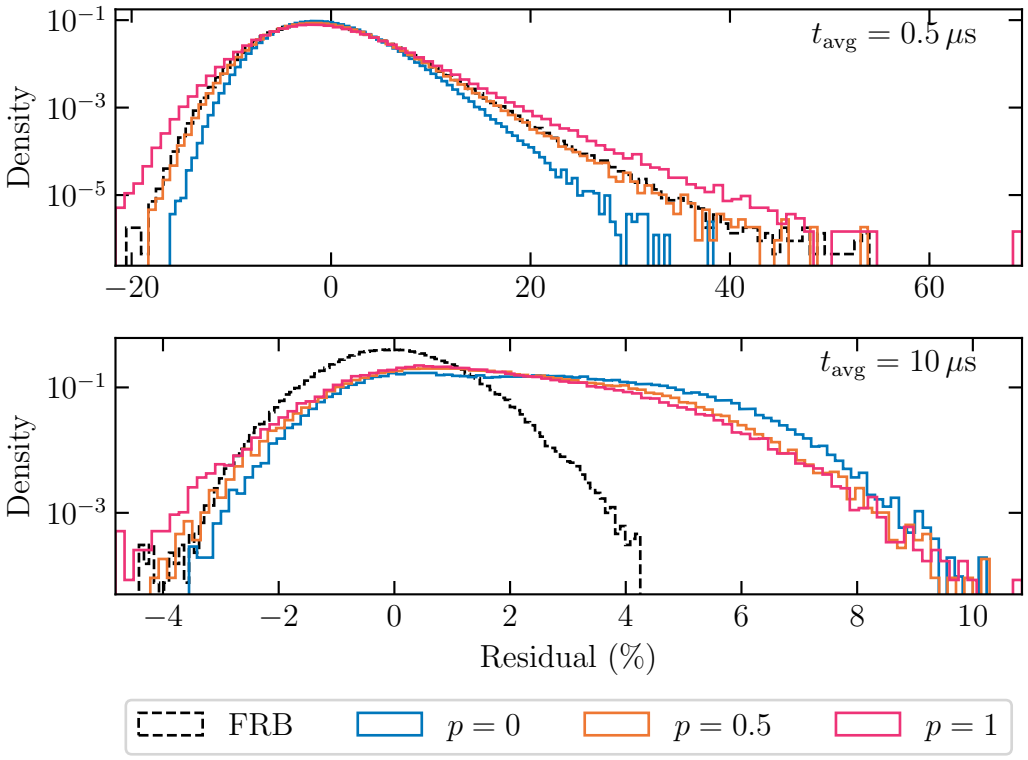

Figure 6.9: Distributions of $g^{(2)}_{\mathrm{synth}}(0) - g^{(2)}_{\mathrm{IPPR}}(0)$ residuals with $\delta\mathrm{DM} = 10^{-5}\,\mathrm{pc\,cm^{-3}}$, $t_{\mathrm{avg}} = 0.5\,\mu\mathrm{s}$ (top) and $t_{\mathrm{avg}} = 10\,\mu\mathrm{s}$ (bottom). The noise distributions include data from five different instances of noise. The distributions of residuals from FRB 20181112A with the direct averaging method are also shown for comparison.

confirm that the residual distributions are dependant on polarisation fraction, a fact that will no doubt be necessary to consider when trying to make sense of these distributions.

6.3.1 On measuring $g^{(2)}(0)$ in coherent synthetic bursts

It would be highly desirable to apply these methods of coherence measurement to a coherent synthetic burst. This would allow for verification that coherence could be detected in an ideal case, and give insight into what would be expected in e.g. the residual distributions.

This, however, would be a major task. To be able to do this, one would need a plausible, well-defined model of the coherent radiation in an FRB to use to synthesise a burst. But no sufficiently predictive and plausible model currently exists in the literature, and the development of one is, unfortunately, too large a task to be able to be included within this thesis.

The simplest models of coherent radiation are: monochromatic, laser-like radiation constant in intensity; and a delta function "shot" of radiation, with all of a burst's energy contained in one time sample. Clearly, neither of these models are plausibly applicable to modelling FRB emission. Any developed model would likely be somewhere in between these two extremes. A plausible starting point is the "shot noise" model (Rickett, 1975; Cordes, 1976), as has been applied to the Crab pulsar (Hankins et al., 2003).

6.4 Summary and areas for future investigation

Several methods have been described for searching for coherence in FRB signals using the second-order intensity correlation function $g^{(2)}(0)$, by comparing to a predicted value $g^{(2)}_{\mathrm{IPPR}}(0)$ for incoherent, partially-polarised radiation. These methods include considerations for mitigating the effects of dispersion on the statistics of FRB signals, and a possible alternative to direct averaging for modeling the

"true" burst profile. No coherence was detected in the test case FRB 20181112A, but the methods have been demonstrated as a proof of concept. The methods were also applied to pure-noise data, and the validity of the IPPR prediction was verified.

Several areas of this investigation are incomplete. The distributions of the residuals between the directly-calculated $g^{(2)}(0)$ and $g^{(2)}_{\mathrm{IPPR}}(0)$ do not appear straightforward to understand, with a characteristic skew towards values implying $g^{(2)}_{\mathrm{FRB}}(0) > g^{(2)}_{\mathrm{IPPR}}(0)$, but a mean value implying $g^{(2)}_{\mathrm{FRB}}(0) \lesssim g^{(2)}_{\mathrm{IPPR}}(0)$.

Development of a predictive theoretical model for coherent radiation in FRBs would be extremely valuable and likely necessary to understand exactly what results should be expected (§6.3.1).

A more careful method for selecting t_{avg} should be pursued. The values of 0.5 µs and 10 µs used throughout this chapter were chosen to summarise the broad effects of changing t_{avg}. There will be a trade-off between signal-to-noise and quality of statistics with varying t_{avg}, and it's completely unclear what value *should* be ideal. A more quantitative, or perhaps even analytical, analysis of this would be helpful, especially in the event that the methods here are generalised to more FRBs.

The method using regularisation instead of direct averaging seems to broadly make the analysis less precise, but given this effect is heavily dependent on t_{avg}, it should still be considered in future investigation.

Future investigations should also take heed of the warning presented by Smits et al. (2003) that scintillation can imprint an apparent measurement of coherence where there may actually be none. The FRB used in this analysis has no measurable scintillation (Sammons et al., 2023), but if this analysis is attempted on bursts with scintillation present, it should be noted that there will possibly be a reduction in sensitivity to coherent structure on the timescales associated with the degree of scintillation.

Finally, the simplest expansion of the analysis presented here would be to apply

it to more FRBs. It is possible that FRB 20181112A's signal was, for some reason or another, decohered. Other FRBs with remarkably little scattering have been observed, and would be ideal candidates for future application of these methods.

Chapter 7

Conclusion

Fast radio bursts, as a field of study, continues to develop rapidly. This has largely been driven by advances in instrumentation and data processing techniques allowing higher detection rates, interferometric imaging of bursts beyond repeaters, and more feasible polarimetric measurements in a range of instruments around the world.

FRB science with ASKAP in particular is on the cusp of a new phase. The imminent CRACO upgrade will give ASKAP a leap forward in the form of a higher burst detection rate. Burst localisations, host galaxy identifications, and high time resolution investigation will accelerate, with the current major bottleneck (rate of detection) being significantly widened.

But it was not always the case that the burst detection rate was the primary bottleneck. At the time work on this thesis started in March 2020, CRAFT was not yet able to process the antenna voltages to produce high-precision burst positions and polarimetric profiles quickly or consistently. This was mostly because the methods to do this were still being developed, understood, and refined. The ability of CRAFT to obtain the final data products had been demonstrated (Bannister et al., 2019b; Cho et al., 2020; Day et al., 2020), but there was not yet a robust pipeline implementing the processing chain.

It's in this context that the CRAFT Effortless Localisation and Enhanced

Burst Inspection pipeline (CELEBI; Chapter 4) stands as the first major outcome of this thesis. As discussed in Chapter 3, CELEBI automates CRAFT voltage processing allowing for much quicker turnaround — from days of intense hands-on operations to only hours with minimal human intervention — among other significant benefits.

At the time of writing, CRACO is in the early stages of its commissioning, and has already detected its first few FRBs in real-time. Going forward CELEBI will certainly, and indeed already does (see the ten publications for which it played a key role, §3.1), play an essential, central role in ASKAP FRB studies.

While the core functionality of CELEBI is complete, active development continues to expand the pipeline's capabilities and ensure that the best data products possible are being produced from the voltages. For example, work is underway by the CRAFT team to apply robust weighting functions to the visibilities from which an FRB is imaged, based on its integrated time profile as determined via beamforming. This would optimise the signal-to-noise ratio of bursts at the imaging stage, and promises a significant improvement to localisation precision.

Aside from improvements to processing, the CRAFT FRB sample promises to be a treasure trove of interesting burst properties and clues towards the nature of FRB emission physics. First steps in digging into this are outlined in Chapters 5 and 6. The investigations and observations presented in these chapters, along with those of Cho et al. (2020) and Day et al. (2020), are among only the first unlocked by the measurement of FRBs at very high time resolution.

The avenues for further exploration and experimentation are too numerous to list all of them here. To highlight just a few I consider particularly interesting:

- **Polarisation behaviours.** The present sample exhibits many strange and diverse behaviours of polarisation angles and fractions. The ability to access these profiles at such high time resolutions and with such high signal-to-noise is one of ASKAP's more unique abilities. These will certainly

be central pieces of the puzzle when it comes to attempting to understand burst emission mechanisms and immediate host environments. Are all FRBs inherently polarised? Is the polarisation initially linear and sometimes is converted to circular? What sorts of environments can produce such diverse behaviours?

- **A rotating progenitor?** A number of FRBs in the ASKAP sample are observed to have multiple clearly separated, distinct, often narrow components or "sub-bursts". FRB 20230708A in particular has many of these spread out over tens of milliseconds. In the ASKAP sample, it's clear that at least some of these are only detectable due to the coherent data processing methods and subsequently high signal-to-noise. Are these due to a rotating beam of emission sweeping over the Earth as seen from the source, as modeled for pulsars? If so, what implications does this have for explanations of apparently non-repeating FRBs? Can we expect these sub-bursts to be present in all FRBs given good enough sensitivity, or does it indicate a distinct category of burst?

- **Can we measure burst coherence?** The investigation presented in Chapter 6 is, to my knowledge, the only one done so far into the nature of FRB emission at nanosecond timescales. Indeed, analysis of the coherence of astronomical radio signals in general is not something that has been widely pursued. There is much more effort, time, and rigour that could be applied to this area of research, far more than could be achieved within the scope of this thesis. But this also seems like an area with major potential for unravelling the nature of FRB emission directly — if the expectations for the quantities measured in Chapter 6 can be better understood, the impact of propagation better mediated, and, most importantly, the methods applied to many more bursts.

The aims of this work have been to facilitate and contribute to the capabilities

of ASKAP and the CRAFT Collaboration so that they can continue to play leading roles in the field of FRB science, and to demonstrate the potential of ASKAP's high time resolution measurements to further our understanding of the nature of these peculiar bursts. Some of the next steps have been sketched out above, and it is clear that FRB research is still a young and dynamic field and there is much left to continue on with.

Appendices

Appendix A

Supplementary Tables

Table A.1: FRBs for which a host galaxy has been identified.

FRB	Reference	FRB	Reference
20121102A	Chatterjee et al. (2017)	20200430A	Heintz et al. (2020)
20171020A	Mahony et al. (2018) Lee-Waddell et al. (2023)	20200906A	Bhandari et al. (2022)
20180301A	Bhandari et al. (2022)	20201124A	Fong et al. (2021)
20180814A	Michilli et al. (2023)	20210117A	Bhandari et al. (2023)
20180916B	Marcote et al. (2020)	20210320C	James et al. (2022)
20180924B	Bannister et al. (2019b)	20210410D	Caleb et al. (2023a)
20181030A	Bhardwaj et al. (2021b)	20210603A	Cassanelli et al. (2023)
20181112A	Prochaska et al. (2019)	20210807D	James et al. (2022)
20190102C	Macquart et al. (2020)	20211127I	James et al. (2022)
20190110C	Ibik et al. (2023)	20211203C	Gordon et al. (2023)
20190303A	Michilli et al. (2023)	20211212A	James et al. (2022)
20190425A	Moroianu et al. (2023)	20220105A	Gordon et al. (2023)
20190520B	Niu et al. (2022)	20220207C	Law et al. (2023)
20190523A	Ravi et al. (2019)	20220307B	Law et al. (2023)
20190608B	Macquart et al. (2020)	20220310F	Law et al. (2023)
20190611B	Macquart et al. (2020)	20220319D	Ravi et al. (2023a)
20190614D	Law et al. (2020)	20220418A	Law et al. (2023)
20190711A	Macquart et al. (2020)	20220506D	Law et al. (2023)
20190714A	Heintz et al. (2020)	20220509G	Sharma et al. (2023)
20191001A	Bhandari et al. (2020a)	20220610A	Ryder et al. (2023)
20191106C	Ibik et al. (2023)	20220825A	Law et al. (2023)
20191228A	Bhandari et al. (2022)	20220912A	Ravi et al. (2023b)
20200120E	Kirsten et al. (2022)	20220914A	Sharma et al. (2023)
20200223B	Ibik et al. (2023)	20220920A	Law et al. (2023)
20200428	Bochenek et al. (2020) CHIME/FRB Collaboration et al. (2020b)	20221012A	Law et al. (2023)
		20230718A	Glowacki et al. (2024)

Appendix B

A prediction of $g^{(2)}(0)$ for incoherent, partially-polarised radiation

This derivation was produced by Adrian Sutinjo. It has not been published, and is reproduced here with his permission to create a permanent record.

We wish to make a prediction for the second-order intensity correlation function $g^{(2)}(0)$ for incoherent, partially-polarised radiation, where

$$g^{(2)}(\tau) \equiv \frac{\langle I(t)I(t+\tau)\rangle}{\langle I(t)\rangle^2} \tag{B.1}$$

The incident electric field is a vector $\bar{E} = \hat{v}E_v + \hat{h}E_h$ (where the $\hat{\cdot}$ quantities indicate orthogonal polarization bases: $\hat{v}$ is orthogonal to $\hat{h}$). A polarimeter consists of dual-polarized antennas. For argument's sake let there be orthogonal $\hat{v}$ and $\hat{h}$-polarized antennas. The antenna voltages are

$$S_v(t) = X_v(t) + jY_v(t), \tag{B.2}$$

$$S_h(t) = X_h(t) + jY_h(t). \tag{B.3}$$

The intensity is

$$I(t) = |S_v(t)|^2 + |S_h(t)|^2. \tag{B.4}$$

We then have the mean and variance of $I(t)$:

$$\langle I(t) \rangle = \left\langle |S_v(t)|^2 \right\rangle + \left\langle |S_h(t)|^2 \right\rangle, \tag{B.5}$$

$$\mathrm{var}\left(I(t)\right) = \mathrm{var}\left(|S_v(t)|^2\right) + \mathrm{var}\left(|S_h(t)|^2\right). \tag{B.6}$$

Following from the definition of variance as $\mathrm{var}\left(Z\right) = \langle (Z - \langle Z \rangle)^2 \rangle = \langle Z^2 \rangle - \langle Z \rangle^2$, we can express $g^{(2)}(0)$ as:

$$g^{(2)}(0) = \frac{\langle I(t)^2 \rangle}{\langle I(t) \rangle^2} \tag{B.7}$$

$$= \frac{\mathrm{var}\left(I(t)\right)}{\langle I(t) \rangle^2} + 1 \tag{B.8}$$

We also have

$$\mathrm{var}\left(|S_v(t)|^2\right) = \left\langle |S_v(t)|^2 |S_v(t)|^2 \right\rangle - \left\langle |S_v(t)|^2 \right\rangle^2 \tag{B.9}$$

$$= 2\left\langle |S_v(t)|^2 \right\rangle^2 - \left\langle |S_v(t)|^2 \right\rangle^2 \tag{B.10}$$

$$= \left\langle |S_v(t)|^2 \right\rangle^2, \tag{B.11}$$

$$\implies \mathrm{var}\left(|S_h(t)|^2\right) = \left\langle |S_h(t)|^2 \right\rangle^2. \tag{B.12}$$

Combining eqs B.11 and B.12 with eq B.8:

$$g^{(2)}(0) = \frac{\left\langle |S_v(t)|^2 \right\rangle^2 + \left\langle |S_h(t)|^2 \right\rangle^2}{\left(\left\langle |S_v(t)|^2 \right\rangle + \left\langle |S_h(t)|^2 \right\rangle\right)^2} + 1 \tag{B.13}$$

$$= \frac{\left\langle |S_v(t)|^2 \right\rangle^2 + \left\langle |S_h(t)|^2 \right\rangle^2}{\left\langle |S_v(t)|^2 \right\rangle^2 + \left\langle |S_h(t)|^2 \right\rangle^2 + 2\left\langle |S_v(t)|^2 \right\rangle \left\langle |S_h(t)|^2 \right\rangle} + 1. \tag{B.14}$$

To find the bounds of possible values for $g^{(2)}(0)$ for partially-polarised radiation, we will consider in turn the fully unpolarised and fully polarised cases.

For fully unpolarised radiation, $\langle|S_h(t)|^2\rangle = \langle|S_v(t)|^2\rangle$, hence

$$g^{(2)}(0) = \frac{\langle|S_v(t)|^2\rangle^2 + \langle|S_v(t)|^2\rangle^2}{\langle|S_v(t)|^2\rangle^2 + \langle|S_v(t)|^2\rangle^2 + \langle|S_v(t)|^2\rangle^2 + \langle|S_v(t)|^2\rangle^2} + 1 \tag{B.15}$$

$$= \frac{2}{4} + 1 = 1.5. \tag{B.16}$$

For fully polarised radiation, $2\langle|S_v(t)|^2\rangle\langle|S_h(t)|^2\rangle = 0$, as all of the radiation's energy is contained in only one of the polarisation bases, and therefore one of $\langle|S_v(t)|^2\rangle$ or $\langle|S_h(t)|^2\rangle$ must be 0. Then

$$g^{(2)}(0) = \frac{\langle|S_v(t)|^2\rangle^2 + \langle|S_h(t)|^2\rangle^2}{\langle|S_v(t)|^2\rangle^2 + \langle|S_h(t)|^2\rangle^2} + 1 \tag{B.17}$$

$$= 2. \tag{B.18}$$

We now compute $g^{(2)}(0)$ for partially polarised radiation. Let the polarized wave be fully contained in S_v; hence there is zero polarised wave in S_h. $S_{vp}(t) = X_{vp}(t) + jY_{vp}(t)$ is then the polarised component. The unpolarised components are

$$S_{vu}(t) = X_{vu}(t) + jY_{vu}(t), \tag{B.19}$$

$$S_{hu}(t) = X_{hu}(t) + jY_{hu}(t), \tag{B.20}$$

where our assumption of incoherence sets $X_{vu}(t), Y_{vu}(t), X_{hu}(t), Y_{hu}(t)$ as zero-mean Gaussian i.i.d. random variables. Hence

$$\left\langle|S_h(t)|^2\right\rangle = \left\langle|S_{hu}(t)|^2\right\rangle. \tag{B.21}$$

$$\left\langle |S_v(t)|^2 \right\rangle = \left\langle |S_{vu}(t) + S_{vp}(t)|^2 \right\rangle \tag{B.22}$$

$$= \left\langle (X_{vu}(t) + X_{vp}(t))^2 + (Y_{vu}(t) + Y_{vp}(t))^2 \right\rangle \tag{B.23}$$

$$= \left\langle X_{vu}(t)^2 + 2X_{vu}(t)X_{vp}(t) + X_{vp}(t)^2 + Y_{vu}(t)^2 + 2Y_{vu}(t)Y_{vp}(t) + Y_{vp}(t)^2 \right\rangle \tag{B.24}$$

$$= \left\langle |S_{vu}(t)|^2 \right\rangle + \left\langle |S_{vp}(t)|^2 \right\rangle, \tag{B.25}$$

since $\langle X_{vu}(t)X_{vp}(t)\rangle = 0$ and $\langle Y_{vu}(t)Y_{vp}(t)\rangle = 0$ because X_{vu}, X_{vp} and Y_{vu}, Y_{vp} are independent noise and X_{vu}, Y_{vu} are zero mean.

Since $X_{vu}(t), Y_{vu}(t), X_{hu}(t), Y_{hu}(t)$ are zero-mean Gaussian i.i.d., $\langle |S_{hu}(t)|^2\rangle = \langle |S_{vu}(t)|^2\rangle$. Therefore

$$\langle I(t)\rangle = \left\langle |S_{vp}(t)|^2 \right\rangle + \left\langle |S_{vu}(t)|^2 \right\rangle + \left\langle |S_{hu}(t)|^2 \right\rangle \tag{B.26}$$

$$= \left\langle |S_{vp}(t)|^2 \right\rangle + 2\left\langle |S_{hu}(t)|^2 \right\rangle. \tag{B.27}$$

The fraction of polarisation is

$$p \equiv \frac{\text{polarised intensity}}{\text{total intensity}} \tag{B.28}$$

$$= \frac{\langle |S_{vp}(t)|^2\rangle}{\langle I(t)\rangle} \tag{B.29}$$

$$= \frac{\langle |S_{vp}(t)|^2\rangle}{\langle |S_{vp}(t)|^2\rangle + 2\langle |S_{hu}(t)|^2\rangle} \tag{B.30}$$

$$= \frac{1}{1 + 2\frac{\langle |S_{hu}(t)|^2\rangle}{\langle |S_{vp}(t)|^2\rangle}} \tag{B.31}$$

$$\implies \frac{\langle |S_{hu}(t)|^2\rangle}{\langle |S_{vp}(t)|^2\rangle} = 0.5\frac{1-p}{p} = 0.5F, \tag{B.32}$$

where F is the ratio of unpolarised to polarised component.

Having expressions for $I(t)$ and p, we seek to express $\text{var}\,(I(t))$. We now know that

$$\left\langle |S_h(t)|^2 \right\rangle^2 = \left\langle |S_{hu}(t)|^2 \right\rangle^2, \tag{B.33}$$

$$\left\langle |S_v(t)|^2 \right\rangle^2 = \left\langle |S_{vu}(t)|^2 \right\rangle^2 + \left\langle |S_{vp}(t)|^2 \right\rangle^2 + 2 \left\langle |S_{vu}(t)|^2 \right\rangle \left\langle |S_{vp}(t)|^2 \right\rangle \tag{B.34}$$

$$= \left\langle |S_{hu}(t)|^2 \right\rangle^2 + \left\langle |S_{vp}(t)|^2 \right\rangle^2 + 2 \left\langle |S_{hu}(t)|^2 \right\rangle \left\langle |S_{vp}(t)|^2 \right\rangle, \tag{B.35}$$

Hence, from eqs B.6, B.12, and B.11:

$$\text{var}\left(I(t)\right) = \left\langle |S_v(t)|^2 \right\rangle^2 + \left\langle |S_h(t)|^2 \right\rangle^2 \tag{B.36}$$

$$= 2 \left\langle |S_{hu}(t)|^2 \right\rangle^2 + \left\langle |S_{vp}(t)|^2 \right\rangle^2 + 2 \left\langle |S_{vp}(t)|^2 \right\rangle \left\langle |S_{hu}(t)|^2 \right\rangle \tag{B.37}$$

Bringing together eqs B.37 and B.27,

$$\frac{\text{var}\left(I(t)\right)}{\langle I(t)\rangle^2} = \frac{2 \left\langle |S_{hu}(t)|^2 \right\rangle^2 + \left\langle |S_{vp}(t)|^2 \right\rangle^2 + 2 \left\langle |S_{vp}(t)|^2 \right\rangle \left\langle |S_{hu}(t)|^2 \right\rangle}{(\left\langle |S_{vp}(t)|^2 \right\rangle + 2 \left\langle |S_{hu}(t)|^2 \right\rangle)^2} \tag{B.38}$$

$$= \frac{2 \left\langle |S_{hu}(t)|^2 \right\rangle^2 + \left\langle |S_{vp}(t)|^2 \right\rangle^2 + 2 \left\langle |S_{vp}(t)|^2 \right\rangle \left\langle |S_{hu}(t)|^2 \right\rangle}{4 \left\langle |S_{hu}(t)|^2 \right\rangle^2 + \left\langle |S_{vp}(t)|^2 \right\rangle^2 + 4 \left\langle |S_{vp}(t)|^2 \right\rangle \left\langle |S_{hu}(t)|^2 \right\rangle} \tag{B.39}$$

Making substitutions for F from eq B.32

$$= \frac{0.5F^2 + 1 + F}{F^2 + 1 + 2F} \tag{B.40}$$

$$= \frac{0.5F^2 + 1 + F}{(F+1)^2} \tag{B.41}$$

$$= 0.5(1 + p^2) \tag{B.42}$$

Therefore, for incoherent partially polarized source

$$g^{(2)}(0) = \frac{\text{var}\left(I(t)\right)}{\langle I(t)\rangle^2} + 1 = 1.5 + 0.5p^2. \tag{B.43}$$

Appendix C

Co-author attribution

Chapter 4

This chapter is the paper "CELEBI: The CRAFT Effortless Localisation and Enhanced Burst Inspection Pipeline", published in Astronomy & Computing Volume 44. CELEBI was designed, developed, and tested by me, with contributions from co-authors as listed below. The draft manuscript was written primarily by me, except where stated otherwise below, and circulated to all co-authors for review.

Hyerin Cho contributed to early development of methodology and software implementing polyphase filterbank inversion, coherent beamforming, derippling, coherent dedispersion, IFFT, and calculation of Stokes parameters. Cherie Day contributed to early development of methodology and software implementing imaging and localisation of bursts. Adam Deller contributed to development of the methodology employed by CELEBI and components of the source code; executed CELEBI and validated output data products; wrote part of section 3.3.2 & all of section 3.3.3; reviewed the manuscript and provided editorial suggestions. Marcin Glowacki provided project supervision; contributed to development throughout CELEBI; executed CELEBI and validated output data products; reviewed and edited the manuscript. Kelly Gourdji contributed to development throughout CELEBI; executed CELEBI and validated output data products; reviewed and

edited the manuscript. Keith Bannister developed the methodology and software related to ASKAP's voltage capture system, including that related to handling raw voltage data and performing polyphase filterbank inversion. Apurba Bera developed methodology and software implementing automatic flagging of RFI-affected data and wrote section 3.4; reviewed and edited the manuscript. Shivani Bhandari developed methodology and software implementing polarisation calibration. Clancy James provided project supervision; developed methodology and software implementing statistical determination of mean source offsets; reviewed and edited the manuscript. Ryan Shannon contributed to development of the high-level methodology of ASKAP voltage capture and burst localisation.

Chapter 5

This chapter is the paper entitled "The CRAFT high time resolution FRB sample", intended for submission to Proceedings of the Astronomical Society of Australia. The version presented here has been through one round of review within the Commensal Real-time ASKAP Fast Transients Collaboration, and may differ from the submitted and accepted versions. I performed data processing, analysis, and interpretation, with contributions from co-authors as listed below. The draft manuscript was written primarily by me, except where stated otherwise below, and circulated to all co-authors for review.

Marcin Glowacki provided project supervision; processed FRB data; assisted with data analysis; reviewed and edited the manuscript. Adam Deller processed FRB data; contributed to development of methodology of ASKAP voltage capture and processing; reviewed and edited the manuscript. Kelly Gourdji processed FRB data; reviewed and edited the manuscript. Apurba Bera processed FRB data. Tyson Dial processed FRB data; validated polarisation calibration. Clancy James provided project supervision and conception of work; wrote section 4.2, part of sections 4.1, 4.3, and 4.4; reviewed and edited the manuscript. Ryan Shannon oversaw ASKAP operations for CRAFT FRB detections; curated ASKAP voltage data; contributed to the development of the methodology of ASKAP voltage

capture and data processing; assisted with validation of polarimetry. Keith Bannister contributed to development of methodology of ASKAP voltage capture and data processing. Shivani Bhandari operated ASKAP for CRAFT FRB detections. Adrian Sutinjo provided project supervision.

Appendix B

This derivation was produced by Adrian Sutinjo. It has not been published, and is reproduced here with his permission to create a permanent record.

Bibliography

T. Akahori, et al. (2016). 'Fast radio bursts as probes of magnetic fields in the intergalactic medium'. *The Astrophysical Journal* **824**(2):105.

R. Anna-Thomas, et al. (2023). 'Magnetic field reversal in the turbulent environment around a repeating fast radio burst'. *Science* **380**(6645):599–603. Publisher: American Association for the Advancement of Science.

Astropy Collaboration, et al. (2022). 'The Astropy Project: Sustaining and Growing a Community-oriented Open-source Project and the Latest Major Release (v5.0) of the Core Package*'. *The Astrophysical Journal* **935**(2):167. Publisher: The American Astronomical Society.

Astropy Collaboration, et al. (2018). 'The Astropy Project: Building an Open-science Project and Status of the v2.0 Core Package*'. *The Astronomical Journal* **156**(3):123. Publisher: The American Astronomical Society.

M. Bailes (2022). 'The discovery and scientific potential of fast radio bursts'. *Science* **378**(6620):eabj3043. Publisher: American Association for the Advancement of Science.

K. Bannister, et al. (2019a). 'FREDDA: A fast, real-time engine for de-dispersing amplitudes'.

K. W. Bannister, et al. (2019b). 'A single fast radio burst localized to a massive galaxy at cosmological distance'. *Science* **365**(6453):565–570. Publisher: American Association for the Advancement of Science.

K. W. Bannister, et al. (2017). 'The Detection of an Extremely Bright Fast Radio Burst in a Phased Array Feed Survey'. *The Astrophysical Journal* **841**(1):L12.

J. Baptista, et al. (2023). 'Measuring the Variance of the Macquart Relation in z-DM Modeling'. arXiv:2305.07022 [astro-ph].

M. C. Bezuidenhout, et al. (2023). 'Tied-array beam localization of radio transients and pulsars'. *RAS Techniques and Instruments* **2**(1):114–128.

S. Bhandari, et al. (2020a). 'Limits on Precursor and Afterglow Radio Emission from a Fast Radio Burst in a Star-forming Galaxy'. *The Astrophysical Journal Letters* **901**(2):L20. Publisher: The American Astronomical Society.

S. Bhandari, et al. (2023). 'A Nonrepeating Fast Radio Burst in a Dwarf Host Galaxy'. *The Astrophysical Journal* **948**(1):67. Publisher: The American Astronomical Society.

S. Bhandari, et al. (2022). 'Characterizing the Fast Radio Burst Host Galaxy Population and its Connection to Transients in the Local and Extragalactic Universe'. *The Astronomical Journal* **163**(2):69. Publisher: The American Astronomical Society.

S. Bhandari, et al. (2020b). 'The Host Galaxies and Progenitors of Fast Radio Bursts Localized with the Australian Square Kilometre Array Pathfinder'. *The Astrophysical Journal* **895**(2):L37. Publisher: American Astronomical Society.

M. Bhardwaj, et al. (2021a). 'A Nearby Repeating Fast Radio Burst in the Direction of M81'. *The Astrophysical Journal Letters* **910**(2):L18. Publisher: The American Astronomical Society.

M. Bhardwaj, et al. (2021b). 'A Local Universe Host for the Repeating Fast Radio Burst FRB 20181030A'. *The Astrophysical Journal Letters* **919**(2):L24. Publisher: The American Astronomical Society.

C. D. Bochenek, et al. (2020). 'A fast radio burst associated with a Galactic magnetar'. *Nature* **587**(7832):59–62. Number: 7832 Publisher: Nature Publishing Group.

M. Caleb, et al. (2023a). 'A subarcsec localized fast radio burst with a significant host galaxy dispersion measure contribution'. *Monthly Notices of the Royal Astronomical Society* **524**(2):2064–2077.

M. Caleb, et al. (2023b). 'Discovery of an as-yet non-repeating fast radio burst with the hallmarks of a repeater'. arXiv:2302.09754 [astro-ph].

M. Caleb, et al. (2018). 'The SUrvey for Pulsars and Extragalactic Radio Bursts – III. Polarization properties of FRBs 160102 and 151230'. *Monthly Notices of the Royal Astronomical Society* **478**(2):2046–2055.

CASA Team, et al. (2022). 'CASA, the Common Astronomy Software Applications for Radio Astronomy'. *Publications of the Astronomical Society of the Pacific* **134**(1041):114501. Publisher: The Astronomical Society of the Pacific.

T. Cassanelli, et al. (2023). 'A fast radio burst localized at detection to a galactic disk using very long baseline interferometry'. arXiv:2307.09502 [astro-ph].

S. Chatterjee, et al. (2017). 'A direct localization of a fast radio burst and its host'. *Nature* **541**(7635):58–61. Number: 7635 Publisher: Nature Publishing Group.

CHIME/FRB Collaboration, et al. (2023a). 'Updating the first CHIME/FRB catalog of fast radio bursts with baseband data'. arXiv:2311.00111 [astro-ph].

CHIME/FRB Collaboration, et al. (2021). 'The First CHIME/FRB Fast Radio Burst Catalog'. *The Astrophysical Journal Supplement Series* **257**(2):59. Publisher: The American Astronomical Society.

CHIME/FRB Collaboration, et al. (2020a). 'Periodic activity from a fast radio burst source'. *arXiv:2001.10275 [astro-ph]* arXiv: 2001.10275.

CHIME/FRB Collaboration, et al. (2020b). 'A bright millisecond-duration radio burst from a Galactic magnetar'. *Nature* **587**(7832):54–58. Number: 7832 Publisher: Nature Publishing Group.

CHIME/FRB Collaboration, et al. (2022). 'Sub-second periodicity in a fast radio burst'. *Nature* **607**(7918):256–259. Number: 7918 Publisher: Nature Publishing Group.

CHIME/FRB Collaboration, et al. (2023b). 'CHIME/FRB Discovery of 25 Repeating Fast Radio Burst Sources'. *The Astrophysical Journal* **947**(2):83. Publisher: The American Astronomical Society.

J. S. Chittidi, et al. (2020). 'Dissecting the Local Environment of FRB 190608 in the Spiral Arm of its Host Galaxy'. *arXiv:2005.13158 [astro-ph]* arXiv: 2005.13158.

H. Cho, et al. (2020). 'Spectropolarimetric Analysis of FRB 181112 at Microsecond Resolution: Implications for Fast Radio Burst Emission Mechanism'. *The Astrophysical Journal Letters* **891**(2):L38. Publisher: The American Astronomical Society.

L. Connor, et al. (2020). 'A bright, high rotation-measure FRB that skewers the M33 halo'. *Monthly Notices of the Royal Astronomical Society* **499**(4):4716–4724.

R. J. Cooke, et al. (2018). 'One Percent Determination of the Primordial Deuterium Abundance*'. *The Astrophysical Journal* **855**(2):102. Publisher: The American Astronomical Society.

J. M. Cordes (1976). 'Pulsar radiation as polarized shot noise'. *The Astrophysical Journal* **210**:780–791.

J. M. Cordes & T. J. W. Lazio (2003). 'NE2001. II. Using Radio Propagation Data to Construct a Model for the Galactic Distribution of Free Electrons'. *arXiv:astro-ph/0301598* arXiv: astro-ph/0301598.

M. Cruces, et al. (2021). 'Repeating behaviour of FRB 121102: periodicity, waiting times, and energy distribution'. *Monthly Notices of the Royal Astronomical Society* **500**(1):448–463.

C. K. Day, et al. (2021). 'Astrometric accuracy of snapshot fast radio burst localisations with ASKAP'. *Publications of the Astronomical Society of Australia* **38**:e050. Publisher: Cambridge University Press.

C. K. Day, et al. (2020). 'High time resolution and polarization properties of ASKAP-localized fast radio bursts'. *Monthly Notices of the Royal Astronomical Society* **497**(3):3335–3350.

A. T. Deller, et al. (2011). 'DiFX-2: A More Flexible, Efficient, Robust, and Powerful Software Correlator'. *Publications of the Astronomical Society of the Pacific* **123**(901):275. Publisher: IOP Publishing.

P. Di Tommaso, et al. (2017). 'Nextflow enables reproducible computational workflows'. *Nature Biotechnology* **35**(4):316–319.

D. Dravins (2008). 'Photonic Astronomy and Quantum Optics'. In D. Phelan, O. Ryan, & A. Shearer (eds.), *High Time Resolution Astrophysics*, Astrophysics and Space Science Library, pp. 95–132. Springer Netherlands, Dordrecht.

L. N. Driessen, et al. (2023). 'FRB 20210405I: the first Fast Radio Burst sub-arcsecond localised with MeerKAT'. arXiv:2302.09787 [astro-ph].

R. C. Duncan & C. Thompson (1992). 'Formation of Very Strongly Magnetized Neutron Stars: Implications for Gamma-Ray Bursts'. *The Astrophysical Journal* **392**:L9. ADS Bibcode: 1992ApJ...392L...9D.

W. Farah, et al. (2018). 'FRB microstructure revealed by the real-time detection of FRB170827'. *Monthly Notices of the Royal Astronomical Society* **478**(1):1209–1217.

Y. Feng, et al. (2022). 'Frequency-dependent polarization of repeating fast radio bursts—implications for their origin'. *Science* **375**(6586):1266–1270. Publisher: American Association for the Advancement of Science.

K. M. Ferrière (2001). 'The interstellar environment of our galaxy'. *Reviews of Modern Physics* **73**(4):1031–1066. Publisher: American Physical Society.

W.-f. Fong, et al. (2021). 'Chronicling the Host Galaxy Properties of the Remarkable Repeating FRB 20201124A'. *The Astrophysical Journal Letters* **919**(2):L23. Publisher: American Astronomical Society.

V. Gajjar, et al. (2018). 'Highest Frequency Detection of FRB 121102 at 4–8 GHz Using the Breakthrough Listen Digital Backend at the Green Bank Telescope'. *The Astrophysical Journal* **863**(1):2. Publisher: The American Astronomical Society.

A. Ginsburg, et al. (2019). 'astroquery: An Astronomical Web-querying Package in Python'. *The Astronomical Journal* **157**(3):98. Publisher: The American Astronomical Society.

M. Glowacki, et al. (2024). 'H i, FRB, What's Your z: The First FRB Host Galaxy Redshift from Radio Observations'. *The Astrophysical Journal Letters* **962**(1):L13. Publisher: The American Astronomical Society.

A. C. Gordon, et al. (2023). 'The Demographics, Stellar Populations, and Star Formation Histories of Fast Radio Burst Host Galaxies: Implications for the Progenitors'. *The Astrophysical Journal* **954**(1):80. Publisher: The American Astronomical Society.

D. Gordon, et al. (2016). *Difxcalc - Calc11 for the DiFX Correlator*. Conference Name: New Horizons with VGOS Pages: 187-192 ADS Bibcode: 2016ivs..conf..187G.

E. W. Greisen (2003). 'AIPS, the VLA, and the VLBA'. In A. Heck (ed.), *Information Handling in Astronomy - Historical Vistas*, Astrophysics and Space Science Library, pp. 109–125. Springer Netherlands, Dordrecht.

C. L. Hale, et al. (2021). 'The Rapid ASKAP Continuum Survey Paper II: First Stokes I Source Catalogue Data Release'. *Publications of the Astronomical Society of Australia* **38**:e058. Publisher: Cambridge University Press.

R. Hanbury Brown & R. Q. Twiss (1956a). 'Correlation between Photons in two Coherent Beams of Light'. *Nature* **177**(4497):27–29. Number: 4497 Publisher: Nature Publishing Group.

R. Hanbury Brown & R. Q. Twiss (1956b). 'A Test of a New Type of Stellar Interferometer on Sirius'. *Nature* **178**(4541):1046–1048. Number: 4541 Publisher: Nature Publishing Group.

T. H. Hankins (1971). 'Microsecond Intensity Variations in the Radio Emissions from CP 0950'. *The Astrophysical Journal* **169**:487. ADS Bibcode: 1971ApJ...169..487H.

T. H. Hankins & J. A. Eilek (2007). 'Radio Emission Signatures in the Crab Pulsar'. *The Astrophysical Journal* **670**(1):693. Publisher: IOP Publishing.

T. H. Hankins, et al. (2003). 'Nanosecond radio bursts from strong plasma turbulence in the Crab pulsar'. *Nature* **422**(6928):141–143. Number: 6928 Publisher: Nature Publishing Group.

C. R. Harris, et al. (2020). 'Array programming with NumPy'. *Nature* **585**(7825):357–362. Number: 7825 Publisher: Nature Publishing Group.

K. E. Heintz, et al. (2020). 'Host Galaxy Properties and Offset Distributions of Fast Radio Bursts: Implications for Their Progenitors'. *The Astrophysical Journal* **903**(2):152. Publisher: The American Astronomical Society.

D. M. Hewitt, et al. (2023). 'Dense forests of microshots in bursts from FRB 20220912A'. *Monthly Notices of the Royal Astronomical Society* **526**(2):2039–2057.

G. B. Hobbs, et al. (2006). 'tempo2, a new pulsar-timing package – I. An overview'. *Monthly Notices of the Royal Astronomical Society* **369**(2):655–672.

A. W. Hotan, et al. (2021). 'Australian square kilometre array pathfinder: I. system description'. *Publications of the Astronomical Society of Australia* **38**:e009. Publisher: Cambridge University Press.

J. D. Hunter (2007). 'Matplotlib: A 2D Graphics Environment'. *Computing in Science & Engineering* **9**(3):90–95. Conference Name: Computing in Science & Engineering.

S. Hutschenreuter, et al. (2022). 'The Galactic Faraday rotation sky 2020'. *Astronomy & Astrophysics* **657**:A43. Publisher: EDP Sciences.

A. L. Ibik, et al. (2023). 'Proposed host galaxies of repeating fast radio burst sources detected by CHIME/FRB'. arXiv:2304.02638 [astro-ph].

C. W. James, et al. (2022). 'A measurement of Hubble's Constant using Fast Radio Bursts'. *Monthly Notices of the Royal Astronomical Society* **516**(4):4862–4881.

F. A. Jenet, et al. (2001). 'The First Detection of Coherent Emission from Radio Pulsars'. *The Astrophysical Journal* **558**:302–308.

E. F. Keane, et al. (2016). 'The host galaxy of a fast radio burst'. *Nature* **530**(7591):453.

K. I. Kellermann & I. I. K. Pauliny-Toth (1969). 'The Spectra of Opaque Radio Sources'. *The Astrophysical Journal* **155**:L71. ADS Bibcode: 1969ApJ...155L..71K.

F. Kirsten, et al. (2022). 'A repeating fast radio burst source in a globular cluster'. *Nature* **602**(7898):585–589. Number: 7898 Publisher: Nature Publishing Group.

P. Kumar, et al. (2023). 'Propagation of a fast radio burst through a birefringent relativistic plasma'. *Physical Review D* **108**(4):043009. Publisher: American Physical Society.

C. J. Law, et al. (2018). 'realfast: Real-time, Commensal Fast Transient Surveys with the Very Large Array'. *The Astrophysical Journal Supplement Series* **236**(1):8. Publisher: The American Astronomical Society.

C. J. Law, et al. (2020). 'A Distant Fast Radio Burst Associated with Its Host Galaxy by the Very Large Array'. *The Astrophysical Journal* **899**(2):161. Publisher: The American Astronomical Society.

C. J. Law, et al. (2023). 'Deep Synoptic Array Science: First FRB and Host Galaxy Catalog'. arXiv:2307.03344 [astro-ph].

K. Lee-Waddell, et al. (2023). 'The host galaxy of FRB 20171020A revisited'. *Publications of the Astronomical Society of Australia* **40**:e029.

D. Lorimer & M. Kramer (2005). *Handbook of Pulsar Astronomy*. Cambridge University Press, Cambridge.

D. R. Lorimer, et al. (2007). 'A Bright Millisecond Radio Burst of Extragalactic Origin'. *Science* **318**(5851):777–780.

R. Loudon (1980). 'Non-classical effects in the statistical properties of light'. *Reports on Progress in Physics* **43**(7):913.

R. Luo, et al. (2020). 'Diverse polarization angle swings from a repeating fast radio burst source'. *Nature* **586**(7831):693–696. Number: 7831 Publisher: Nature Publishing Group.

M. Lyutikov (2022). 'Faraday Conversion in Pair-symmetric Winds of Magnetars and Fast Radio Bursts'. *The Astrophysical Journal Letters* **933**(1):L6. Publisher: The American Astronomical Society.

M. Lyutikov, et al. (2020). 'FRB Periodicity: Mild Pulsars in Tight O/B-star Binaries'. *The Astrophysical Journal Letters* **893**(2):L39. Publisher: The American Astronomical Society.

J.-P. Macquart, et al. (2010). 'The Commensal Real-Time ASKAP Fast-Transients (CRAFT) Survey'. *Publications of the Astronomical Society of Australia* **27**(3):272–282. Publisher: Cambridge University Press.

J.-P. Macquart, et al. (2020). 'A census of baryons in the Universe from localized fast radio bursts'. *Nature* **581**(7809):391–395. Number: 7809 Publisher: Nature Publishing Group.

E. K. Mahony, et al. (2018). 'A search for the host galaxy of FRB171020' .

A. G. Mannings, et al. (2023). 'Fast Radio Bursts as Probes of Magnetic Fields in Galaxies at z $<$ 0.5'. arXiv:2209.15113 [astro-ph].

B. Marcote, et al. (2020). 'A repeating fast radio burst source localized to a nearby spiral galaxy'. *Nature* **577**(7789):190–194. Number: 7789 Publisher: Nature Publishing Group.

L. Marnoch, et al. (2023). 'The unseen host galaxy and high dispersion measure of a precisely localized fast radio burst suggests a high-redshift origin'. *Monthly Notices of the Royal Astronomical Society* **525**(1):994–1007.

M. McQuinn (2013). 'Locating the "missing" baryons with extragalactic dispersion measure estimates'. *The Astrophysical Journal Letters* **780**(2):L33.

D. B. Melrose (2017). 'Coherent emission mechanisms in astrophysical plasmas'. *Reviews of Modern Plasma Physics* **1**(1):5.

D. Michilli, et al. (2023). 'Subarcminute Localization of 13 Repeating Fast Radio Bursts Detected by CHIME/FRB'. *The Astrophysical Journal* **950**(2):134. Publisher: The American Astronomical Society.

D. Michilli, et al. (2021). 'An Analysis Pipeline for CHIME/FRB Full-array Baseband Data'. *The Astrophysical Journal* **910**(2):147. Publisher: The American Astronomical Society.

D. Michilli, et al. (2018). 'An extreme magneto-ionic environment associated with the fast radio burst source FRB 121102'. *Nature* **553**(7687):182–185. Number: 7687 Publisher: Nature Publishing Group.

A. Moroianu, et al. (2023). 'An assessment of the association between a fast radio burst and binary neutron star merger'. *Nature Astronomy* **7**(5):579–589. Number: 5 Publisher: Nature Publishing Group.

I. S. Morrison, et al. (2020). 'Performance of Oversampled Polyphase Filterbank Inversion via Fourier Transform'. *Journal of Astronomical Instrumentation* **09**(01):2050004. Publisher: World Scientific Publishing Co.

F. Nicastro, et al. (2008). 'Missing Baryons and the Warm-Hot Intergalactic Medium'. *Science* **319**(5859):55–57. Publisher: American Association for the Advancement of Science.

K. Nimmo, et al. (2022). 'Burst timescales and luminosities as links between young pulsars and fast radio bursts'. *Nature Astronomy* **6**(3):393–401. Number: 3 Publisher: Nature Publishing Group.

C.-H. Niu, et al. (2022). 'A repeating fast radio burst associated with a persistent radio source'. *Nature* **606**(7916):873–877. Number: 7916 Publisher: Nature Publishing Group.

A. Pandhi, et al. (2024). 'Polarization properties of the 128 non-repeating fast radio bursts from the first CHIME/FRB baseband catalog'. arXiv:2401.17378 [astro-ph].

K. Park & E. G. Blackman (2010). 'Effect of plasma composition on the interpre-

tation of Faraday rotation'. *Monthly Notices of the Royal Astronomical Society* **403**(4):1993–1998.

I. Pastor-Marazuela, et al. (2021). 'Chromatic periodic activity down to 120 megahertz in a fast radio burst'. *Nature* **596**(7873):505–508. Number: 7873 Publisher: Nature Publishing Group.

E. Petroff, et al. (2019). 'Fast Radio Bursts'. *The Astronomy and Astrophysics Review* **27**(1):4. arXiv:1904.07947 [astro-ph].

Planck Collaboration, et al. (2016). 'Planck 2015 results - XIII. Cosmological parameters'. *Astronomy & Astrophysics* **594**:A13. Publisher: EDP Sciences.

E. Platts, et al. (2019). 'A living theory catalogue for fast radio bursts'. *Physics Reports* **821**:1–27.

Z. Pleunis, et al. (2021a). 'Fast Radio Burst Morphology in the First CHIME/FRB Catalog'. *The Astrophysical Journal* **923**(1):1. Publisher: The American Astronomical Society.

Z. Pleunis, et al. (2021b). 'LOFAR Detection of 110–188 MHz Emission and Frequency-dependent Activity from FRB 20180916B'. *The Astrophysical Journal Letters* **911**(1):L3. Publisher: The American Astronomical Society.

J. X. Prochaska, et al. (2019). 'The low density and magnetization of a massive galaxy halo exposed by a fast radio burst'. *Science* **366**(6462):231–234. Publisher: American Association for the Advancement of Science Section: Report.

J. X. Prochaska, et al. (2023). 'FRBs/FRB: Release to sync with Gordon et al. 2023'.

J. X. Prochaska & Y. Zheng (2019). 'Probing Galactic haloes with fast radio bursts'. *Monthly Notices of the Royal Astronomical Society* **485**:648–665.

C. R. Purcell, et al. (2020). 'RM-Tools: Rotation measure (RM) synthesis and Stokes QU-fitting'.

H. Qiu, et al. (2023). 'Systematic performance of the ASKAP fast radio burst search algorithm'. *Monthly Notices of the Royal Astronomical Society* **523**(4):5109–5119.

H. Qiu, (), et al. (2020). 'A population analysis of pulse broadening in ASKAP fast radio bursts'. *Monthly Notices of the Royal Astronomical Society* **497**(2):1382–1390.

K. M. Rajwade, et al. (2020). 'Possible periodic activity in the repeating FRB 121102'. *Monthly Notices of the Royal Astronomical Society* **495**(4):3551–3558.

V. Ravi, et al. (2023a). 'Deep Synoptic Array science: a 50 Mpc fast radio burst constrains the mass of the Milky Way circumgalactic medium'. arXiv:2301.01000 [astro-ph].

V. Ravi, et al. (2023b). 'Deep Synoptic Array Science: Discovery of the Host Galaxy of FRB 20220912A'. *The Astrophysical Journal Letters* **949**(1):L3. Publisher: The American Astronomical Society.

V. Ravi, et al. (2019). 'A fast radio burst localized to a massive galaxy'. *Nature* **572**(7769):352–354. Number: 7769 Publisher: Nature Publishing Group.

B. J. Rickett (1975). 'Amplitude-modulated noise - an empirical model for the radio radiation received from pulsars'. *The Astrophysical Journal* **197**:185–191.

T. P. Robitaille, et al. (2013). 'Astropy: A community Python package for astronomy'. *Astronomy & Astrophysics* **558**:A33. Publisher: EDP Sciences.

S. D. Ryder, et al. (2022). 'Probing the distant universe with a very luminous fast radio burst at redshift 1'. arXiv:2210.04680 [astro-ph].

S. D. Ryder, et al. (2023). 'Probing the distant universe with a very luminous fast radio burst at redshift 1'. arXiv:2210.04680 [astro-ph].

M. W. Sammons, et al. (2023). 'Two-Screen Scattering in CRAFT FRBs'. arXiv:2305.11477 [astro-ph].

D. R. Scott, et al. (2023). 'CELEBI: The CRAFT Effortless Localisation and Enhanced Burst Inspection pipeline'. *Astronomy and Computing* **44**:100724.

R. M. Shannon, et al. (2018). 'The dispersion–brightness relation for fast radio bursts from a wide-field survey'. *Nature* **562**(7727):386.

K. Sharma, et al. (2023). 'Deep Synoptic Array Science: A Massive Elliptical Host Among Two Galaxy-cluster Fast Radio Bursts'. *The Astrophysical Journal* **950**(2):175. Publisher: The American Astronomical Society.

M. B. Sherman, et al. (2024). 'Deep Synoptic Array Science: Polarimetry of 25 New Fast Radio Bursts Provides Insights into Their Origins'. *The Astrophysical Journal* **964**(2):131. Publisher: The American Astronomical Society.

S. Simha, et al. (2023). 'Searching for the Sources of Excess Extragalactic Dispersion of FRBs'. *The Astrophysical Journal* **954**(1):71. Publisher: The American Astronomical Society.

J. M. Smits, et al. (2003). 'On the search for coherent radiation from radio pulsars'. *Astronomy and Astrophysics* **405**:795–801.

L. G. Spitler, et al. (2016). 'A repeating fast radio burst'. *Nature* **531**(7593):202.

A. T. Sutinjo, et al. (2023). 'Calculation and Uncertainty of Fast Radio Burst Structure Based on Smoothed Data'. *The Astrophysical Journal* **954**(1):37. Publisher: The American Astronomical Society.

D. Thornton, et al. (2013). 'A Population of Fast Radio Bursts at Cosmological Distances'. *Science* **341**(6141):53–56.

T. Totani (2013). 'Cosmological Fast Radio Bursts from Binary Neutron Star Mergers'. *Publications of the Astronomical Society of Japan* **65**(5):L12.

J. Tuthill, et al. (2015). 'Compensating for Resampling Effects in Polyphase Channelizers: A Radio Astronomy Application' Publisher: IEEE.

P. Virtanen, et al. (2020). 'SciPy 1.0: fundamental algorithms for scientific computing in Python'. *Nature Methods* **17**(3):261–272. Number: 3 Publisher: Nature Publishing Group.

D. Xiao & Z.-G. Dai (2022). 'New insights into the criterion of fast radio burst in the light of FRB 20121102A'. *Astronomy & Astrophysics* **657**:L7. Publisher: EDP Sciences.

H. Xu, et al. (2022). 'A fast radio burst source at a complex magnetized site in a barred galaxy'. *Nature* **609**(7928):685–688. Number: 7928 Publisher: Nature Publishing Group.

J. Xu & J. L. Han (2024). 'The Huge Magnetic Toroids in the Milky Way Halo'. *The Astrophysical Journal* **966**(2):240. arXiv:2404.02038 [astro-ph].

J. M. Yao, et al. (2017). 'A new electron-density model for estimation of pulsar and FRB distances'. *The Astrophysical Journal* **835**(1):29.

B. Zackay & E. O. Ofek (2017). 'An accurate and efficient algorithm for detection of fast radio bursts with an unknown dispersion measure, for single-dish telescopes and interferometers'. *The Astrophysical Journal* **835**(1):11.

B. Zhang (2020). 'Fast Radio Bursts from Interacting Binary Neutron Star Systems'. *The Astrophysical Journal Letters* **890**(2):L24. Publisher: The American Astronomical Society.

B. Zhang (2022). 'The Physics of Fast Radio Bursts'. arXiv:2212.03972 [astro-ph].

W. Zhu, et al. (2020). 'A Fast Radio Burst Discovered in FAST Drift Scan Survey'. *The Astrophysical Journal Letters* **895**(1):L6. Publisher: The American Astronomical Society.